A Computational Model of Arterial Structures: A Relationship to Alzheimer's Disease

---

A thesis submitted in partial fulfilment of the

requirements for the Degree

of Master of Biomedical Engineering

in the University of Canterbury

by Svava Kristinsdottir

University of Canterbury

2009

Table of Contents

1 ACKNOWLEDGMENTS 9

2 ABSTRACT 10

3 GLOSSARY 12

4 INTRODUCTION 5

5 BASIC ANATOMY OF THE BRAIN 7

5.1 The Brainstem 7
5.1.1 The Medulla oblongata 8
5.1.2 The Pons 9
5.1.3 The Mesencephalon 9
5.1.4 Reticular formation 10

5.2 The cerebellum 11

5.3 The Diencephalon 12
5.3.1 Thalamus 13
5.3.2 The Subthalamus 14
5.3.3 The Epithalamus 14
5.3.4 The Hypothalamus 15

5.4 Cerebrum 16
5.4.1 Basal Nuclei 18
5.4.2 Limbic system 18

5.5 Arteries of the brain and neck 19

5.6 Arterioles and capillaries 21

6 BASIC HISTOLOGY OF THE BRAIN 24

6.1 Neurons 24

6.2 Glia 26
6.2.1 Astrocytes 26
6.2.2 Oligodendrocytes 28
6.2.3 Ependymal cells 29

6.3 Microglia 29

7 BASIC PHYSIOLOGY OF THE BRAIN 31

7.1 Cell communication **31**
7.1.1 Chemical signaling 32
7.1.2 Neuronal signals 33

7.2 Cells and action potentials **35**
7.2.1 The plasma membrane $Na + - K +$ pump 35
7.2.2 Cell $Ca + +$ pumps 36
7.2.3 The generation of action potential 37

7.3 Myelination **39**

7.4 Transport of substances through the cell membrane **40**

7.5 Diffusion of lipid-soluble substances across membranes **41**

7.6 Diffusion across a membrane **41**

8 ALZHEIMER'S DISEASE **43**

8.1 Cellular pathology of Alzheimer **43**
8.1.1 Hypoperfusion and beta-amyloid 46
8.1.2 Energy deficiency and beta-amyloid 47
8.1.3 Hypoxia and beta-amyloid 47

8.2 Watershed Zones **49**

8.3 Causes and treatment of Alzheimer's **50**

9 BINARY TREE **52**

10 LITERATURE REVIEW **54**

10.1 Arterial branching classification **55**

10.2 Arterial bifurcation and Murray's law **56**

10.3 Arterial models **61**
10.3.1 Zero-dimensional models 62
10.3.2 One-dimensional models 63
10.3.3 Two-dimensional models 64
10.3.4 Three-dimensional models 66

10.4 Morphometric characteristics of optimized arterial tress **67**

10.5 Cerebral cortex microcirculation morphometry. **72**

11 METHOD **75**

11.1 Comparing CCO and SM Methods **75**
11.1.1 Global Model Parameters and Physiological Values 77

11.1.2 Data Structure 79
11.1.3 Boundary Conditions 82
11.1.4 Bifurcation Conditions 84
11.1.5 Random Coordinates 85
11.1.6 Supporting Area 87
11.1.7 Adding a Terminal Segment 90
11.1.8 Spatial optimization of new bifurcation 94

11.2 Search algorithms 97
11.2.1 Tree search 97
11.2.2 Bread Crumb search 102

11.3 Alzaidi model 103

11.4 Geometrical properties 106

11.5 Statistics and Perfusion Area diagram 107

12 RESULTS AND DISCUSSION 109

12.1 Graphical results 110

12.2 Morphological Results 112

12.3 Geometric properties of T2000 120

12.4 Branching angles 120
12.4.1 Bifurcation symmetry index 121
12.4.2 Area expansion ratio 123

12.5 Flow rate per area 124

12.6 Physiological Results 128
12.6.1 Pressure 128
12.6.2 Flow Rate 131

12.7 Comparing experimental result with T250 133

12.8 Run time results 135
12.8.1 SM Tree Data 136

13 CONCLUSION 137

14 FURTHER RESEARCH 137

15 REFERENCES 139

16 APPENDIX A 143

16.1 An Example of ASCII file AllNodes. 143

17 APPENDIX B 144

17.1 An Example of ASCII file AllNodesLevels. 144

18 APPENDIX C 145

19 APPENDIX D 146

Table of Figures

Figure 1: The major parts of the brain 7
Figure 2: Anterior and posterior view of the brainstem 8
Figure 3: Cross section of the cerebellum. 11
Figure 4: The Diencephalon. 13
Figure 5: The Cerebrum. 17
Figure 6: Arteries of the head and neck. 19
Figure 7: Arteries of the brain , inferior view 20
Figure 8: Structure of an artery. 22
Figure 9: Neuron in the CNS 25
Figure 10:Astrocytes, surrounding a blood vessel 27
Figure 11:Oligodendrocytes 28
Figure 12: Ependymal cells 29
Figure 13:Microglia 30
Figure 14: Paracrine signalling 32
Figure 15: Endocrine signalling 32
Figure 16: Synaptic signalling 33
Figure 17: Action potential. 38
Figure 18: Schematic of a senile plaque. 44
Figure 19: Mechanism of amyloid generation 45
Figure 20: AD and the connection to vascular circulation 50
Figure 21: Binary tree structure 52
Figure 22: Binary subtree 53
Figure 23: Models used in Zamir's research. 58
Figure 24: The distribution of bifurcation index in relation to the segments radii 60
Figure 25: The distribution of the area ratio in relations to the segment radii 61
Figure 26: Schematic picture of Olufsen's arterial tree 63
Figure 27: (A) Schematic representation of a dichotomous branching network. (B) Cross section at each level. (C) Tree is replaced by a single tube with continuously increasing radius. The area of the cross section of the tube is equal to the total area of the cross section of each level of the tree. (D) volume preserving transformation of the varying radius[41]. 64
Figure 28: Schreiner and Buxbaum arterial binary tree of 4000 terminal ends 65
Figure 29: Morphometric comparison between model of 250 terminals and the left coronary artery trees of two humans 66
Figure 30: Three-dimensional perfusion volumes of different square slabs 68
Figure 31: Arterial trees generated by CCO to perfuse volumes of different shapes 69

Figure 32: Comparison of the results from two-dimensional CCO model tree with data from experimental measurements in the rats mesentery 71
Figure 33: (A) Three Coronal section (S1, S2, S3) of Indian ink injected human brain for data acquisition taken from Lauwers et al 73
Figure 34: The morphometric results from Lauwers et al research. (A) The distribution of diameter of the arterioles without mapping. (B) The distribution of diameter after mapping. (C) The distribution of length without the mapping (D) length after mapping. (E) The distribution of diameter of the capillaries 74
Figure 35: Flow diagram explaining the SM program structure. 78
Figure 36: Schematic figure showing pointers connecting nodes forming a small binary tree.....80
Figure 37: Schematic figure explaining the structure of ASCII files in relation to the binary tree structure.....82
Figure 38: Schematic figure showing the relationship between unit circle $Aunit$ and perfusion circle$Aperf$.....89
Figure 39: Schematic figures explaining the addition of a new terminal segment to the SM tree. 92
Figure 40: Schematic figure showing the change of the geometry of the new bifurcation that is formed when a new branch is added to the existing binary tree.....95
Figure 41: Schematic figure showing the two subtrees, right and left. 98
Figure 42: Schematic figure showing the movements of the traveller and follower pointers. (A) moving down the tree. (B) moving up the tree 99
Figure 43: Schematic figure representing the tree search algorithm. 101
Figure 44: Schematic figure showing the bread crumb path. 102
Figure 45: Schematic figure explaining the resistance and flow rate calculations in the binary tree.....105
Figure 46: The six different stages in the run of the model simulation of 2000 terminals.....110
Figure 47:Schreiner and Buxbaum tree of 4000 terminal segments (A) [25]. The SM tree T2000 (B).....112
Figure 48: The total number of segments and the number of terminal segments per bifurcation level of the SM T2000 tree.....113
Figure 49: (A) The mean radii of the SM T2000 as well as the maximum and minimum values. (B) The mean radii of the terminal segments of SM T2000 tree as well as the maximum and minimum values. 115
Figure 50: (A) The distribution of segment diameters from the SM tree of 2000 terminals. (B) Shows the distribution of diameter mapped with inverse square root mapping. (C) The distribution of Lauwers et als results diameter. (D) The distribution of Lauwers et als result diameter with inverse square root mapping. 116

Figure 51: Logarithmic plots of smaller and larger daughter segments from three different arterial trees.....118
Figure 52: Comparing segment lengths of SM tree of 2000 terminals and experimental results published by Lauwers et al 119
Figure 53: The distribution of the bifurcation angle in SM T2000 121
Figure 54: The distribution of the bifurcation symmetry index in the SM T2000 tree. 122
Figure 55: The distribution of the bifurcation symmetry index reproduced from VanBavel and Spaan research. 122
Figure 56: The distribution of the area expansion ratio. 124
Figure 57: Perfusion diagram of different sized SM trees 125
Figure 58: Perfusion diagram of the T2000 SM tree with, (A) 441 equal sized areas and (B) 1681 equal sized areas. 127
Figure 59: Pressure through the SM tree. (A) The average pressure of all segments per bifurcation level as well as maximum and minimum values. (B) The distribution of pressure in the SM tree.....129
Figure: 60 The systemic and pulmonary circulation pressures in the human body. 129
Figure 61: (A) Pressure in the SM T2000 tree in relations to the segment radii. (B) Pressure found in Karch et al tree in relation to the radii of the segments, experimental data from rat mesentery 130
Figure 62 (A) the flow rate through the SM tree plotted on a logarithmic scale in respect to the tree radii. (B) the flow rate through the Karch et al model and the flow rate in the rat mesentery 132
Figure 63: Comparison between SM results and the left coronary arterial trees of two humans. 134
Figure 64: Run time of SM tree with different number of terminal segments. 135

List of Tables

Table 1: Four minimisation functions of the optimal bifurcation geometry 57
Table 2: Statistical description of different CCO trees perfusing square slabs 70
Table 3: Global parameters of the SM model 77
Table 4: Properties of the Class BiNode 79
Table 5: An example of the ASCII files produced by the SM model. 81
Table 6: Root radius of T2000 binary tree at six different intervals....111
Table 7: SM T2000 compared with Lauwers et al and Karch et al results. ...120
Table 8: Comparing SM tree bifurcation symmetry index with other models and experimental results. 123

1 Acknowledgments

The author wishes to express sincere appreciation to Professors Timothy David and Dr Philip Wilson for their assistance in the preparation of this manuscript. Their guidance throughout this project is invaluable and the advice and help with the final layout of the thesis made all the difference.

I would specifically like to thank Professor Timothy David for his patience and understanding as well giving me the chance to work on this thesis at Canterbury University. To Dr. Philip Wilson, I´d like to express my gratitude for his labour intensive proof reading and suggestions to improve the final editions of this thesis.

In addition, special thanks to Dr. Samara Alzaidi, for explaining and assisting in the use of her model, and Dr Stephen Moore for kindly sharing images from his Ph D thesis.

2 Abstract

The role of the cardiovascular system is is to deliver oxygen and nutrients via arteries to the tissues of the body and to remove their waste products through the venous system. Due to certain pathological processes, arteries can be damaged resulting in a reduction of well oxygenated nutrient rich blood delivered to the tissues. Chronic hypoperfusion to the brain has been related to Alzeimer‘s disease (AD). AD primarily affects people over 55 years of age, with an average duration of 7-10 years, resulting in death. Currently there are 600 million people in the world aged 60 years and over. This figure is expected to double by 2025 and to reach 2 billions by 2050. Finding a cure for a neurodegenerative disease such as AD would herald a major breakthrough in medical care. Currently AD is being widely investigated, but in order to find a cure, the complete pathophysiology of AD needs to be understood. Physilogical modelling could play a significant role to further develop that understanding. The underlying cause for AD is debated although several genetic loci have been identified for AD. Scientists have also demonstrated a strong connection with cerebral hypoperfusion. This results in tissue oxygen and nutrition deprivation which is a possible causative factor in the development of AD. In this thesis a Simulation model (SM) has been built to produce an arterial tree which resembles a natureal arterial tree. The SM model is based on Schreiner et al´s Constrained Constructive Optimization (CCO) method. The SM model produces a binary tree by choosing a random point in a defined area, and connects it to an exising tree structure, each time forming a new bifurcation. This bifurcation is optimized using the target function total minimum volume of the tree. The main difference between the CCO and SM method is the handling of the constrained areas in which the binary trees are grown within. The CCO method inceases the constrained area each time a segment is added to the tree structure, resulting in

rescaling of the total tree each time. The SM tree utilizes a unit circle for the tree to grow in and uses a scaling factor to retrieve the real values of the tree segments as needed. Two trees were produced using the SM method, containing 250 (T250) and 2000 (T2000) terminals respectively. The segment Radii and length of the T2000 terminal tree was extracted and reorganized to fit the data structure of a zero-dimensional model developed by Alzaidi. This model was used to produce pressure and flow rate results for the T2000 tree. The relative perfusion of the infiltrated area in the T2000 tree was also calculated. This thesis shows a close resemblance between the SM tree and a true arterial tree, both visually and geometrically. The morphometric distribution of radii and length showed a good correlation between the SM tree and previous experimental research. The real values of radii and length found in the T2000 SM tree were found to be of larger radii and shorter length compared to previously reported values in the literature. However the results from the T250 SM tree showed excellent correlation with previous experimental results. The physiological parameters of pressure changes in the SM T2000 tree strongly mimic known in vivo physiological parameters from the human circulation. The flow rate in the tree was larger than expected, but can easily be rectified by changing the initial parameters of the SM program. The perfusion distribution diagram demonstrates a well known in vivo occurrence known as watershed zones which has recently been shown to be strongly associated with pathophysiological changes found on autopsies of brains from Alzheimer’s patients.

3 Glossary

Action potential: A momentary change in electrical potential on the surface of a cell, especially of a nerve or muscle cell, that occurs when it is stimulated, resulting in the transmission of an electrical impulse.

Antiport: A mechanism for the coupled transport of two different molecules or ions through a membrane in opposite directions

Carrier protein: membrane transport protein that binds to a solute and transports it across the membrane by undergoing a series of conformational changes

Chemical synapses: specialized junctions through which cells of the nervous system signal one another

CNS: The central nervous system (CNS) represents the part of the nervous system including the brain and the spinal cord.

Cytosol: contents of the main compartment of the cytoplasm excluding membrane-bound organelles.

Eukaryote: living organism composed of one or more cells with a distinct nucleus and cytoplasm. Includes all forms of life except viruses and bacteria (prokaryotes).

Omentum: One of the folds of the peritoneum that connect the stomach with other abdominal organs.

Pia mater: the membrane covering the outside of the brain and spinal cord

PNS: peripheral nervous system, the nervous system outside the CNS

Neurotransmitters: chemicals that are used to relay, amplify and modulate signals between neurons or other cell types.

Nodes of Ranvier: the gaps (about 1 micrometer in diameter) formed between myelin sheath cells along axons or nerve fibers. ...

Sarcoplasmic reticulum: The sarcoplasmic reticulum is a special type of smooth ER found in smooth and striated muscle.

4 Introduction

Chronic cerebral hypoperfusion has now been related to Alhzeimer´s disease (AD). AD mostly affects people of the age 55 or older and has a progression time of 7-10 year duration, finally resulting in death. Today there are 600 million people worldwide aged 60 years and over and this figure is expected to double by 2025 and reach 2 billion by 2050. The underlying aetiology for AD is debated, several genetic loci have been identified and recently a pathophysiological link has been established between cerebral hypoperfusion with decreased oxygen pressure, cortical watershed infarcts and the development and progression of AD. Currently there is no cure for AD. The economic burden of AD, which is by far the most common cause of dementia, is projected to increase. Currently around 50% of nursing home patients in the US have dementia, and AD is the 6th leading cause of death [1, 2]. Finding a cure for a neurodegenerative disease such as AD would herald a major breakthrough in medical care. Currently AD is being widely investigated, but in order to find a cure, the complete pathophysiology of AD needs to be understood.

Both in vivo and cadaver studies have been performed to asses the function and structure of arterial trees, but they can be labour intensive and usually only provide limited specific data. Physiological modelling of the arterial circulation structure and perfusion of brain tissue could provide valuable insight in the investigation of AD by providing multiple different data. In this thesis an arterial tree simulation model (SM) was developed based on a method developed by Schreiner and Buxbaum. The SM method was used to generate two trees of 250 terminals (T250) and 2000 terminals (2000). The

purpose of the model was to explore the geometrical, and physiological properties and compare it to previous literature and experimental results.

5 Basic Anatomy of the Brain

The nervous system is divided into the central nerves system (CNS) and the peripheral nervous system (PNS). The brain is that part of the CNS contained within the cranial cavity. It is the control centre for many of the body functions. The brain consists of the brainstem, diencephalon, cerebellum and cerebrum, Figure 1.

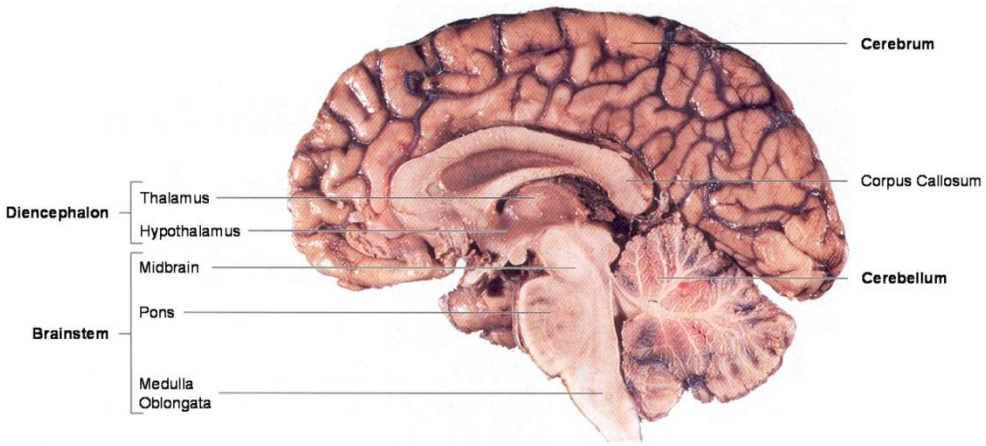

Figure 1: The major parts of the brain [3]

There are twelve pairs of cranial nerves, originating from the brain and are considered a part of the CNS. Two pairs arise from the cerebrum and the remaining ten from the brainstem, Figure 2.

5.1 The Brainstem

The Brainstem connects the brain to the spinal cord. It‘s divided into medulla oblongata, pons, mesencephalon or midbrain and reticular formation.

5.1.1 The Medulla oblongata

The medulla oblongata, or simply the medulla, is about three centimeters long and is the most inferior part of the brainstem. It connects to the spinal cord containing ascending and descending nerve tracts. On the surface, the spinal cord appears to blend into the medulla but a closer look reveals several differences between the two sections are observed. In the medulla oblongata, clusters of gray matters or discrete nuclei can be found, while in the spinal cord the gray matter extends as a continuous mass in the centre of the cord. There are two prominent enlargements on the anterior surface of the medulla oblongata called the pyramids, Figure 2

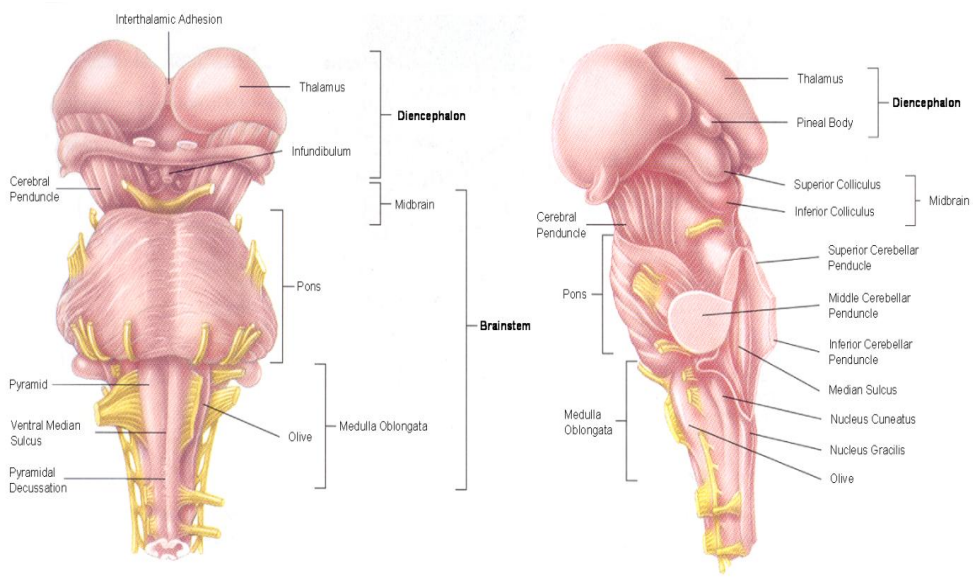

Figure 2: Anterior and posterior view of the brainstem [4]

The reason for the name is the shape of the enlargement, broader near the pons and taper toward the spine. The pyramids are descending nerve tracts involved in the conscious control of skeletal muscles. Near their inferior ends, most of the fibers of the descending nerve tracts cross to the opposite side or decussate. This decussating accounts in part for the fact that each half of the brain

controls the opposite half of the body. Two round oval structures, called olives, protrude from the anterior surface of the medulla oblongata just lateral to the superior margins of the pyramids. The olives are nuclei involved in functions such as balance, coordination and modulation of sound from the inner ear. The nuclei of cranial nerves V (trigeminal), IX (glossopharyngeal), X (vagus), XI (accessory), and XII (hypoglossal) are also located within the medulla.

5.1.2 The Pons

The part of the brainstem superior to the medulla oblongata is the pons, Figure 2. This contains ascending and descending nerve tracts and several nuclei. The pontine nuclei located in the anterior portion of the pons relay information from the cerebrum to the cerebellum. The nuclei for cranial nerves V (trigeminal), VI (abducens), VII (facial), VIII (vestibulocochlear) and IX (glossopharyngeal) are contained within the posterior pons, Figure 2. Other important pontine areas include the pontine sleep centre and respiratory centre that work with the respiratory centers in the medulla to help control respiration.

5.1.3 The Mesencephalon

The mesencephalon is the smallest region of the brainstem, Figure 2. It is superior to the pons and contains the nuclei of cranial nerves III (oculomotor), IV (trochlear) and V (trigeminal). The tectum (roof) of the mesencephalon consists of four nuclei that form mounds on the dorsal surface, collectively called corpora quadrigemina (four twins). Each mound is called a colliculus (hill) and the two superior mounds are called superior colliculi, and the two

inferior mounds are called inferior colliculi. The inferior colliculi are involved in hearing and are an integral part of the auditory pathways in the CNS. Neurons conducting action potentials from the structures of the inner ear to the brain, synapse in the inferior colliculi. The superior colliculi are involved in visual reflexes and they receive input from the eyes, the inferior colliculi, the skin and the cerebrum. The tegmentum (floor) of the mesencephalon largely consists of ascending tracts like the spinal lemniscus and the medial lemniscus from the spinal cord and the brain.

The tegmentum also contains the paired red nuclei, which are so named because in fresh brain specimens they are pinkish in colour reflecting their rich blood supply [3]. The red nuclei aid in the subconscious regulation and coordination of motor activities. Cerebral peduncles (the foot of a column) [3] constitute that portion of the mesencephalon ventral to the tegmentum. They consist primarily of descending tracts from the cerebrum to the brainstem and spinal cord and constitute one of the major CNS motor pathways. The substantia nigra is a nuclear mass between the tegmentum and cerebral peduncles containing cytoplasmic melanin granules that give it a dark gray or black colour. The substantia nigra is interconnected with other basal nuclei of the cerebrum.

5.1.4 Reticular formation

A group of nuclei collectively called the reticular formation are scattered throughout the length of the brainstem. The reticular formation receives axons from nerves that innervate the face.

5.2 The cerebellum

The cerebellum means little brain. The cerebellum is attached to the brainstem posterior to the pons, Figure 3. It communicates with other regions of the CNS through three large nerve tracts; the superior, middle and inferior cerebellar peduncles, which connect the cerebellum to the midbrain pons and medulla oblongata.

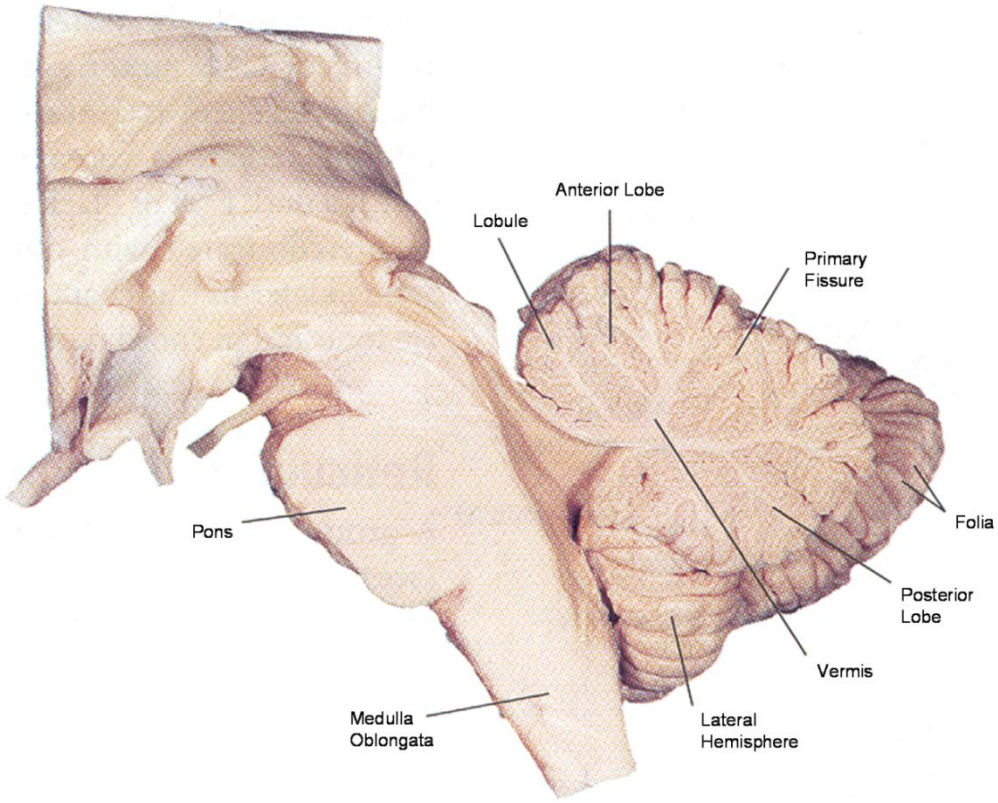

Figure 3: Cross section of the cerebellum [3].

The cerebellum has a gray cortex and nuclei with white medulla in between. The cerebellum cortex has ridges called folia. The white matter of the medulla resembles a branching tree and is called the arbour vitae (tree of life) [3]. The nuclei of the cerebellum are located in the deep inferior centre of the white

matter. The cerebellum consists of three parts a small inferior part, the flocculonodular lobe, a narrow central vermis and two large lateral hemispheres. The flocculonodular part controls balance and eye movements, the vermis and the medial portion of the lateral hemisphere are involved in the control of posture locomotion and fine motor coordination thereby producing smooth flowing movements. The major portion of the lateral hemispheres is involved with the cerebral cortex of the frontal lobe in planning, practicing and learning complex movements.

5.3 The Diencephalon

The diencephalon is the part of the brain between the brainstem and the cerebrum. Its main components are the thalamus, subthalamus, epithalamus and hypothalamus, Figure 4.

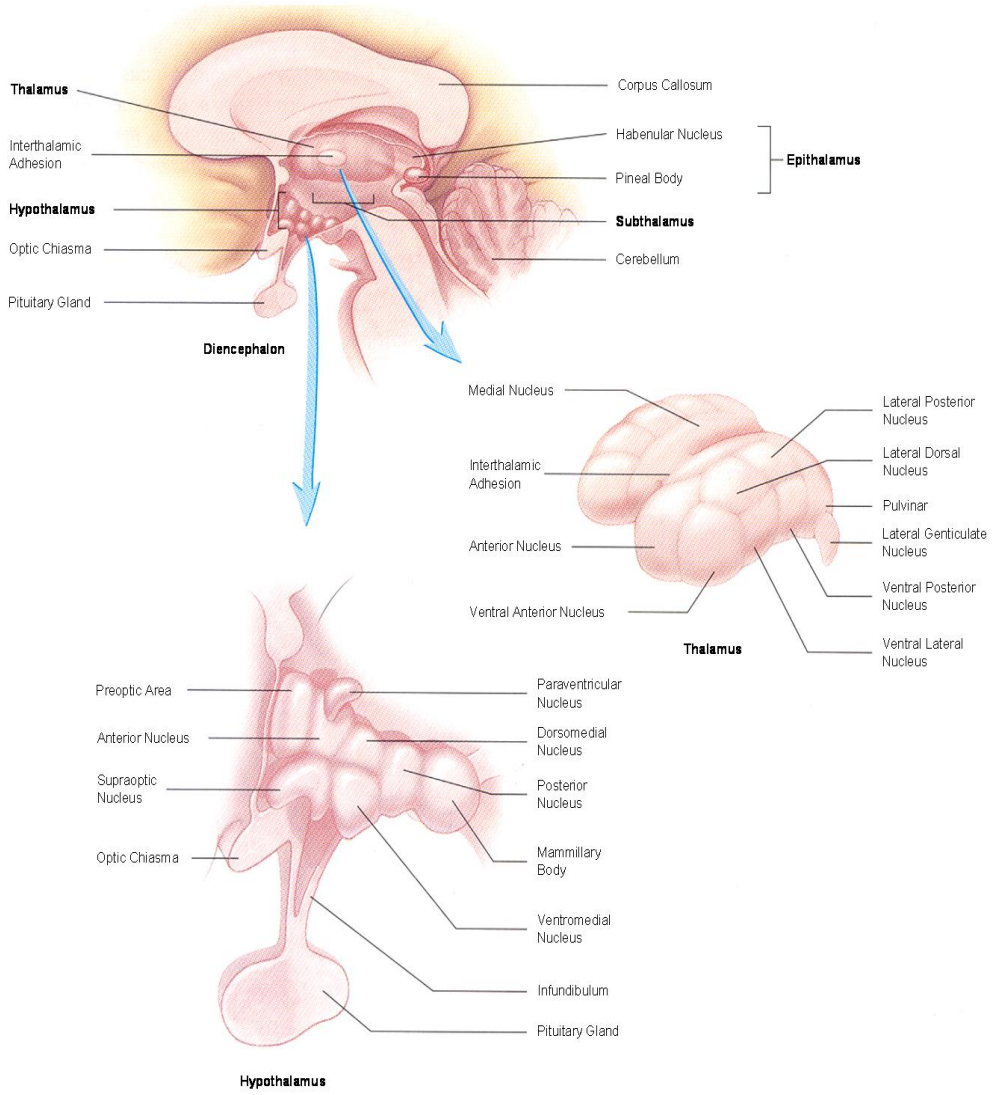

Figure 4: The Diencephalon [4].

5.3.1 Thalamus

Thalamus is by far the largest part of the diencephalon constituting about 75% of its weight [3]. It is a cluster of nuclei shaped somewhat like a yo-yo with two large lateral portions connected in the centre by a small stalk called the interthalamic adhesion or intermediate mass [3]. The space surrounding the interthalamic adhesion and separating the two large portions of the thalamus is

the third ventricle of the brain, Figure 4. Most sensory input projecting to the thalamus are sensory neurons synapsing with thalamic neurons which send projections from the thalamus to the cerebral cortex. Axons carrying auditory information synapse in the medial geniculate (bent like a knee) nucleus of the thalamus axons carrying visual information synapse in the lateral geniculate nucleus and most other sensory impulses synapse in the ventral posterior nucleus. The thalamus also influences mood and actions associated with strong emotions like fear or rage. The ventral anterior and ventral lateral nuclei are involved in motor functions communicating between the basal nuclei cerebellum and the motor cortex. The anterior and medial nuclei are connected to the limbic system and to the prefrontal cortex. They are involved in mood modification. The lateral dorsal nucleus is connected to other thalamic nuclei and to the cerebral cortex and is involved in regulating emotions. The lateral posterior nucleus and the pulvinar (pillow) [3] also have connections to other thalamic nuclei and are involved in sensory integration.

5.3.2 The Subthalamus

The subthalamus is a small area immediately inferior to the thalamus, Figure 4. It contains several ascending and descending nerve tracts and the subthalamic nuclei. A small portion of the red nucleus and substantia nigra of the midbrain extend into this area [3]. The subthalamic nuclei are associated with the basal nuclei and are involved in controlling motor functions.

5.3.3 The Epithalamus

The epithalamus is a small area superior and posterior to the thalamus, Figure 4. It consists of habenular nuclei and the pineal body. The habenular nuclei are involved in the sense of smell, emotional and visceral responses to odours. The

pineal body is shaped somewhat like a pinecone from which the name pineal is derived. It appears to play a role in controlling the onset of puberty but data are inconclusive [3].

5.3.4 The Hypothalamus

The Hypothalamus is the inferior portion of the diencephalon and contains several small nuclei and nerve tracts, Figure 4. The most conspicuous nuclei called the mammillary bodies appear as bulges of the ventral surface of the diencephalon. They are involved in olfactory reflexes and emotional responses to odours. A funnel-shaped stalk, the infundibulum, extends from the floor of the hypothalamus, connects it to the posterior pituitary gland or neurohypothalamus. The hypothalamus plays an important role in controlling the endocrine system because it regulates the hormonal secretion of the pituitary gland, which influences functions as diverse as metabolism, reproduction, responses to stressful stimuli and urine production. Sensory neurons that terminate in the hypothalamus provide input from; 1) visceral organs, 2) taste receptors of the tongue, 3) the limbic system that is involved in responses to smell, 4) specific cutaneous areas such as the nipples and external genitalia and 5) the prefrontal cortex of the cerebrum carrying information related to mood through the thalamus. Efferent fibres from the hypothalamus extend into the brainstem and the spinal cord where they synapse with neurons of the autonomic nervous system. Other fibres extend through the infundibulum to the posterior portion of the pituitary gland: some extend to trigeminal and facial nerve nuclei to help control the head muscles involved in swallowing and some extend to motor neurons of the spinal cord to stimulate shivering.

5.4 Cerebrum

The cerebrum accounts for the largest portion of the total brain weight that is about 1200gr in females and 1400gr in males. Brain size is related to body size, larger brains are associated with larger bodies, not with greater intelligence [3]. The cerebrum is divided into left and right hemispheres by a longitudinal fissure. The most conspicuous features on the surface of each hemisphere are numerous folds called gyri that greatly increase the surface area of the cortex. The intervening grooves between the gyri are called sulci. A central sulcus that extends across the lateral surface of the cerebrum from superior to inferior is located about midway along the length of the brain. The central sulcus is located between the precentral gyrus anteriorly which is the primary motor cortex and a postcentral gyrus posteriorly which is the primary somatic sensory cortex. Each cerebral hemisphere is divided into lobes and is named from the skull bones that overlie each area, frontal, occipital parietal and temporal, Figure 5. The frontal lobe is important in voluntary motor function, motivation, aggression, mood and the sense of smell. The parietal lobe is the major centre for the reception and evaluation of sensory information except for smell, hearing and vision. The frontal and parietal lobes are separated by the central sulcus. The occipital lobe functions in the reception and integration of visual input and is not distinctly separated from the other lobes. The temporal lobe receives and evaluates input for smell and hearing and plays an important role in memory. Its anterior and inferior portions are referred to as the psychic cortex and they are associated with such brain functions as abstract thought and judgement. The temporal lobe is separated from the rest of the cerebrum by a lateral fissure and deep within the fissure is the insula, often referred to as the fifth lobe. The insula is not visible from the surface [5].

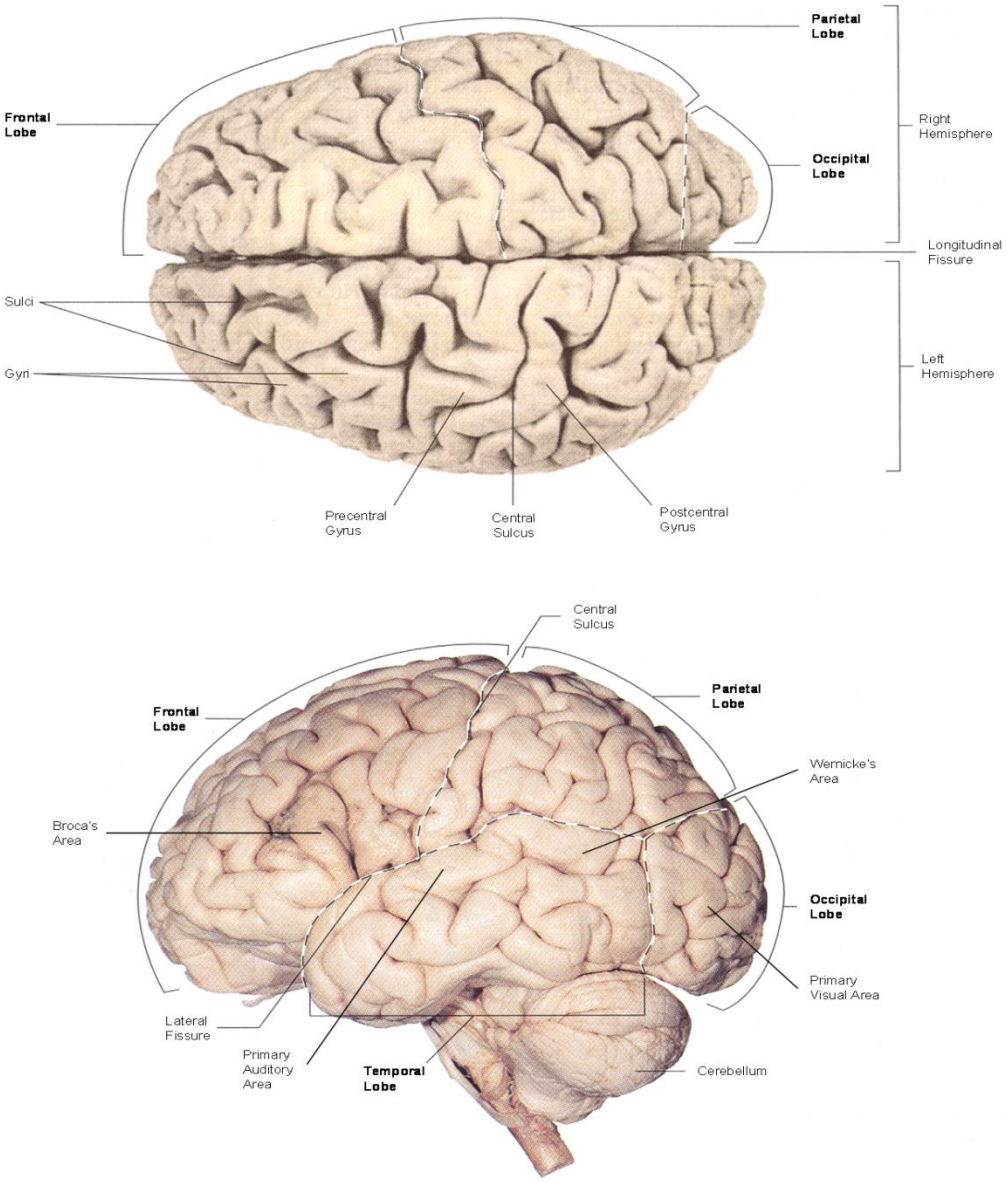

Figure 5: The Cerebrum [4].

The grey matter on the outer surface of the cerebrum is the cortex and the cluster of gray matter deep inside the brain are nuclei. The white matter of the brain between the cortex and nuclei is the cerebral medulla.

5.4.1 Basal Nuclei

The basal nuclei or basal ganglia are a group of functionally related nuclei located bilaterally in the inferior cerebrum, diencephalon and midbrain, Figure 4. These nuclei are involved in the control of motor functions. The nuclei in the cerebrum are collectively called the corpus striatum and include the caudate (having a tail) nucleus and lentiform (lens-shaped) nucleus [3]. They are the largest nuclei of the brain and occupy a large part of the cerebrum. The subthalamic nucleus is located in the diencephalon and the substantia nigra is located in the midbrain [3].

5.4.2 Limbic system

Parts of the cerebrum and diencephalon are grouped together under the title limbic system. The limbic system plays a central role in basic survival functions such as memory, reproduction and nutrition. It is also involved in emotions and memory. Limbus means border and the term limbic refers to deep portions of the cerebrum that form a ring around the diencephalon. Structurally the limbic system consists of cortical areas including the singular gyrus, located along the inner surface of the longitudinal fissure above the corpus callosum and the hippocampus, Figure 4. Various nuclei are found in the limbic system such as the habenular nuclei and the anterior nuclei of the thalamus. The hypothalamus including the mamillary bodies and parts of the basal nuclei are part of the limbic system. The olfactory cortex and tracts that connect the hippocampus to the thalamus and mamillary bodies are also considered to belong to the limbic system [5].

5.5 Arteries of the brain and neck

The first vessel to branch from the aortic arch is the brachiocephalic artery. It is a short artery and branches at the level of the clavicle to form the right common carotid artery, Figure 6. The right carotid artery then transports blood to the right side of the head and neck where as the right subclavian artery transports blood to the right upper limb.

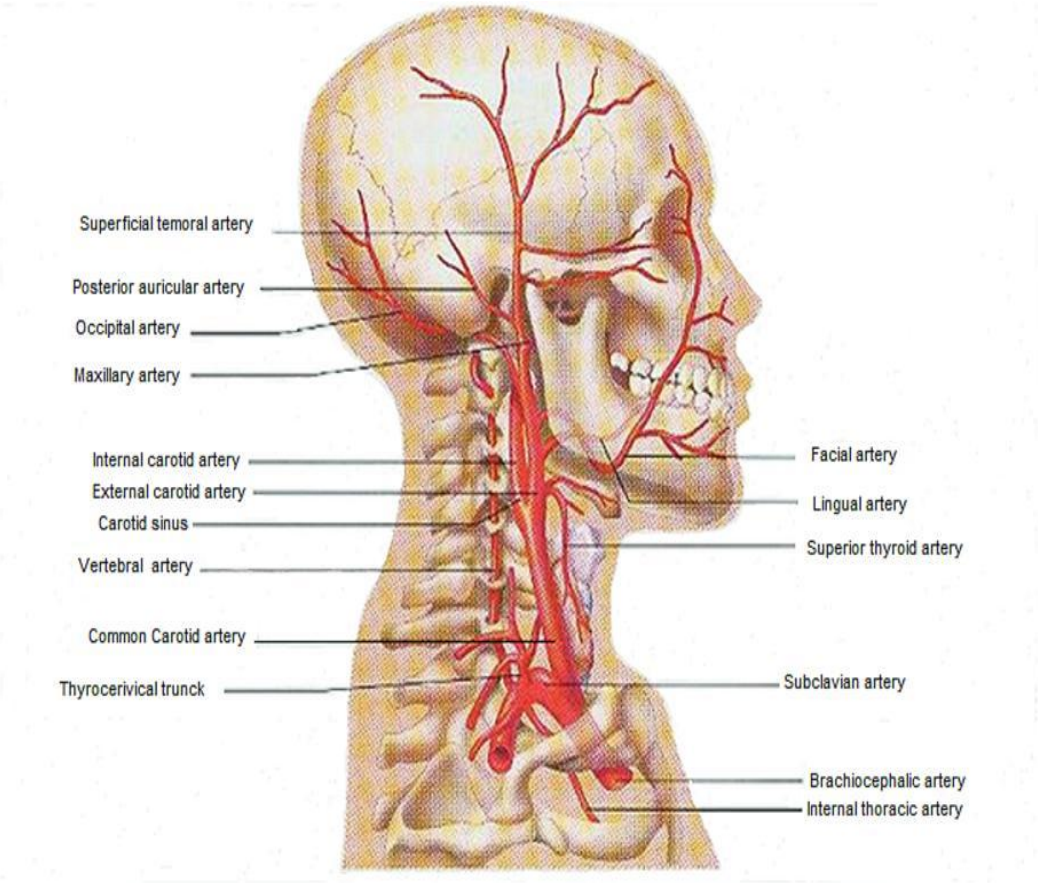

Figure 6: Arteries of the head and neck [4].

The second and third branches of the aortic arch are the left common carotid and subclavian arteries that transport blood to the head and left upper limb. The common carotid artery extends superiorly without branching along either

side of the neck from their base to the inferior angle of the mandible, where each common carotid artery branches into internal and external carotid arteries. At the point of bifurcation on each side of the neck, the common carotid artery and the base of the internal carotid artery are dilated slightly to form the carotid sinuous. The carotid sinuous monitors blood pressure through receptors called baroreceptor. The external carotid arteries have several branches that supply the structures of the neck and face. The internal carotid arteries together with the vertebral arteries, which are branches of the subclavian artery, supply the brain. Branches of the subclavian artery, the left and right vertebral artery enter the cranial cavity through the foramen magnum, give off arteries to the cerebellum and then unite to form a single midline basilar artery.

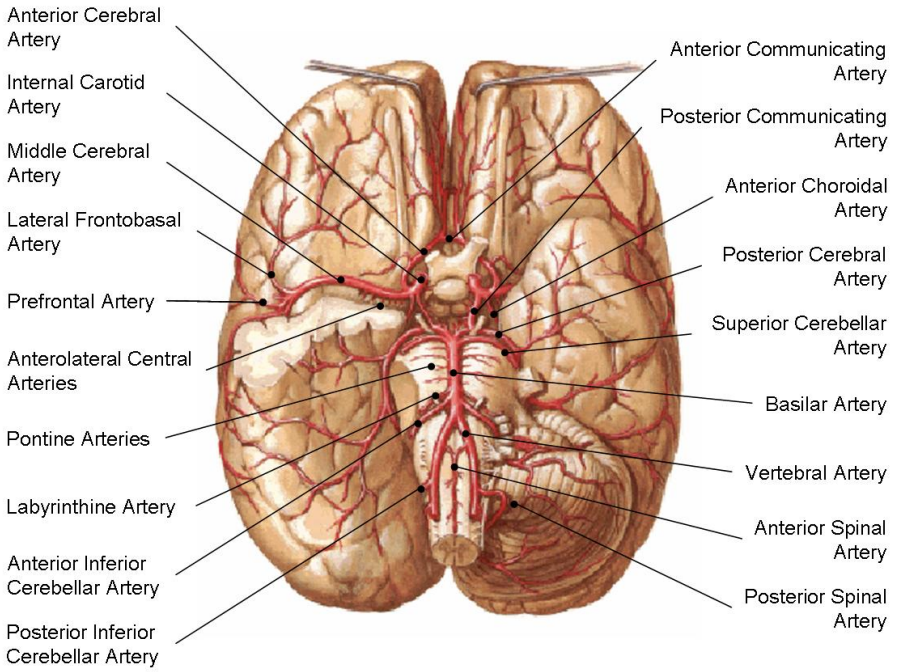

Figure 7: Arteries of the brain , inferior view [4]

The basilar artery gives off branches to the pons and the cerebellum and then branches to form the posterior cerebral arteries, which supply the posterior part of the cerebrum. The internal carotid arteries enter the cranial vault through the carotid canals and terminate by forming the middle cerebral arteries, Figure 7, which supplies large parts of the lateral cerebral cortex. Posterior branches of these arteries, the posterior communicating arteries, unite with the posterior cerebral arteries and finally the anterior branches form the anterior cerebral arteries which supply blood to the frontal lobes of the brain. The anterior cerebral arteries are in turn connected by an anterior communicating artery, which completes a circle around the pituitary gland and the base of the brain called the cerebral arterial circle or commonly known as 'the circle of Willis' [3]. These are the main arteries that supply the brain. The arteries then bifurcate into smaller arterioles which continue to further bifurcate into even smaller arterioles and finally terminate in capillaries.

5.6 Arterioles and capillaries

Arteries will branch up to six or eight times before they become small enough to be categorized as arterioles, which is when the internal diameter ranges between 10-15 micrometers, [6]. The arterioles will then branch two or five times reaching the diameter of 5-9 micrometers before they terminate in a capillary bed, just wide enough to allow the passage of a red blood cell [6].

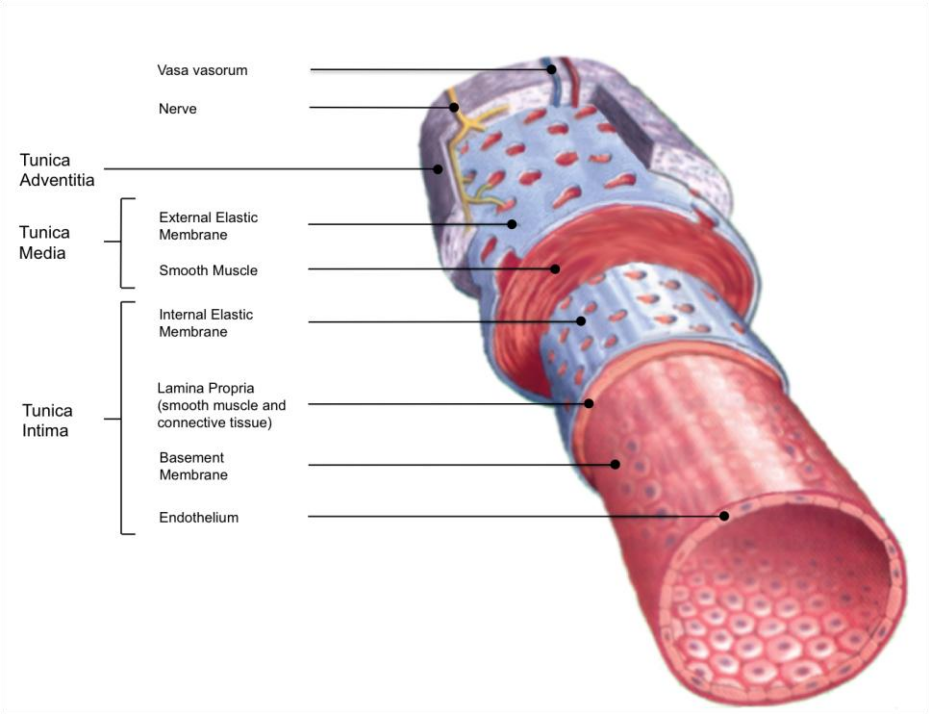

Figure 8: Structure of an artery [4].

The arterioles are highly muscular and can change their diameter radically, Figure 8. The arterioles smooth muscle enables the control of the blood flow to the tissue, depending on its requirements. The structure of the capillary however is different. The walls of the capillaries are extremely thin and are constructed of a single-layer of highly permeable endothelial cells. The capillaries have no smooth muscle cells. However smooth muscle cell fibres, called precapillary sphincters, encircle the vessel at intermittent points allowing for control of the blood flow within the capillary bed. The capillaries are made up by a single layer of endothelial cells. The endothelial cells are connected to a basement-membrane by different types of junctions, which will allow for variable diffusion. In the brain the junctions between the capillary endothelial cells are mainly tight junction that allow only extremely small molecules such as water oxygen and carbon dioxide to pass into or out of the brain tissue [6].

6 Basic Histology of the Brain

The human central nervous system is an enormously complex tissue serving the organism as a processing centre linking information between the outside world and the body. The principal functional unit of the CNS is the neuron although the principal cells of the CNS are neurons, glia and the cells that compose the meanings and blood vessels.

6.1 Neurons

Neurons are cells with long processes specialized to receive conduct and transmit signals in the nervous system. Neurons vary considerably in structure and size throughout the nervous system and within a given brain region. They can be structurally classified as multipolar, bipolar and unipolar neurons. Whatever their shape they all have the following basic elements, a cell body, dendrites and axons, Figure 9.

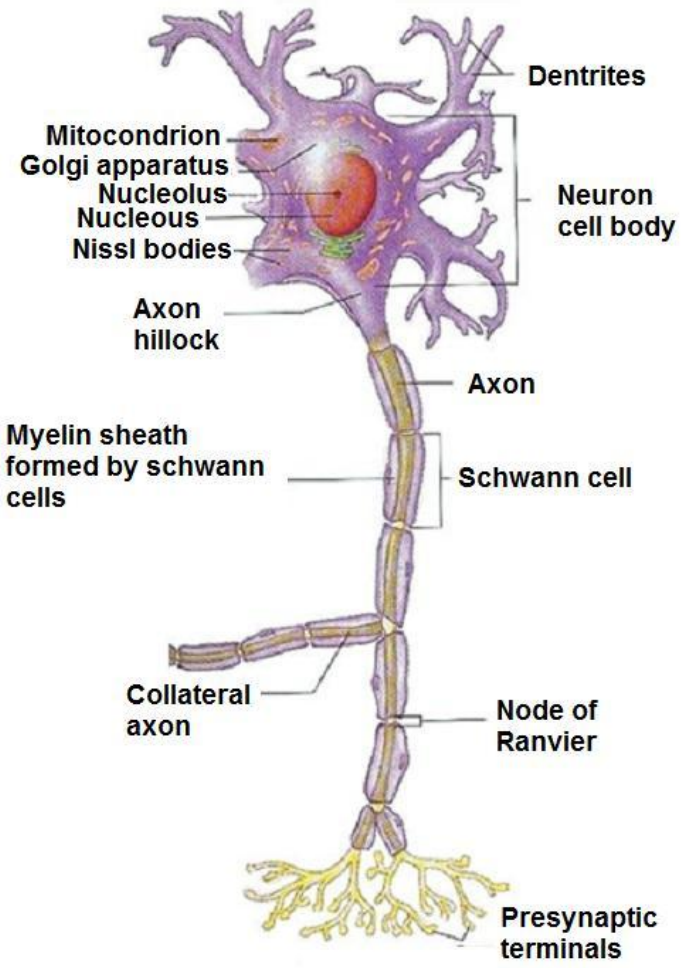

Figure 9: Neuron in the CNS

The neuron cell body contains a single relatively large and centrally located nucleus with a prominent nucleolus. Extensive rough endoplasmic reticulum and Golgi apparatuses surrounding the nucleus and a moderate number of mitochondria and other organelles are also present. Randomly arranged lipid droplets and melanin pigments accumulate in the cytoplasm of some neuron cell bodies. The lipid droplets and melanin pigments increase as human age but their functional significance is unknown. Large numbers of intermediate filaments (neurofilaments) and microtubules form bundles that course through the cytoplasm in all directions. The neurofilaments separate areas of rough

endoplasmic reticulum called chromatophilic substance or Nissl bodies. The presence of organelles such as rough endoplasmic reticulum indicates that the neuron cell body is the primary site of protein synthesis within neurons. The dendrites are short often highly branched cytoplasmic extensions that are tapered from their bases at the neuron cell body to their tips. Dendrites are the input part of the neuron. Axons arise from a cone-shaped area of the neural body called the axon hillock [3]. An axon can remain a single structure or branch to form collateral axons. Axons terminate in an enlarged ends called presynaptic terminals. From the presynaptic terminal the neuron releases chemicals or neurotransmitters into the synaptic cleft. Depending on the chemical and the receiving cell, these neurotransmitters will stimulate or inhibit the postsynaptic cell.

6.2 Glia

Glia cells are derived from neuroectoderm or the bone marrow. The cells that are derived from neuroectoderm are astrocytes, oligodendrocytes and ependyma. The cells that are derived from the bone marrow are called microglia. Glia cells have important structural and metabolic interactions with neurons and their dendrite and axon processes. They also have a primary role in a wide range of normal functions and reactions to injury including inflammation, repair, fluid balance and energy metabolism.

6.2.1 Astrocytes

This glia cell is found throughout the CNS in both gray and white matter. Protoplasmic astrocytes occur mainly in the gray matter fibrous astrocytes occur in the white and gray matter. The cell derives its name from its star-

shaped appearance, due to the cytoplasmic processes that extend from the cell body, Figure 10.

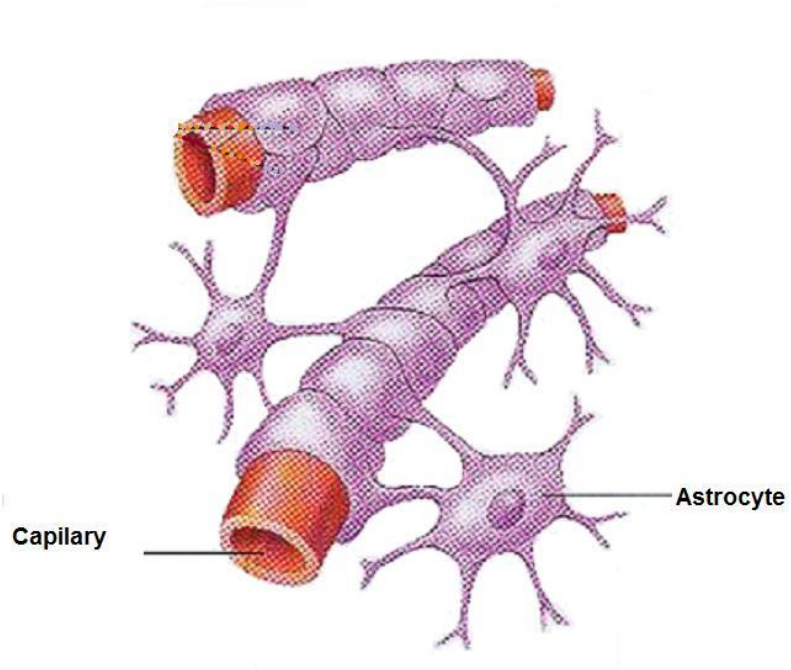

Figure 10:Astrocytes, surrounding a blood vessel,[3]

These extensions widen and spread out to form foot processes which cover the surface of blood vessels, neurons and the pia mater. Astrocytes have an extensive cytoskeleton of microfilaments that enables them to form a supporting framework for blood vessels and neurons. Astrocytes play a role in regulating the extracellular composition of brain fluid. They release chemicals that promote the formation of tight junctions between the endothelial cells of capillaries. The endothelial cells with their tight junctions form the blood-brain barrier, which determines what substances can pass from the blood into the nervous tissue of the brain and spinal cord. Some astrocytic processes are directed toward neurons and their processes and synapses where they are believed to act as metabolic buffers or detoxifiers, suppliers of nutrients and

electrical insulators. Astrocytes are also the principal cells responsible for repair and scar formation in the brain, [7].

6.2.2 Oligodendrocytes

Oligodendroglial cytoplasmic processes wrap around the axons of neurons of neurons to form myelin in a manner analogous to the Schwann cells of the peripheral nervous system, Figure 11.

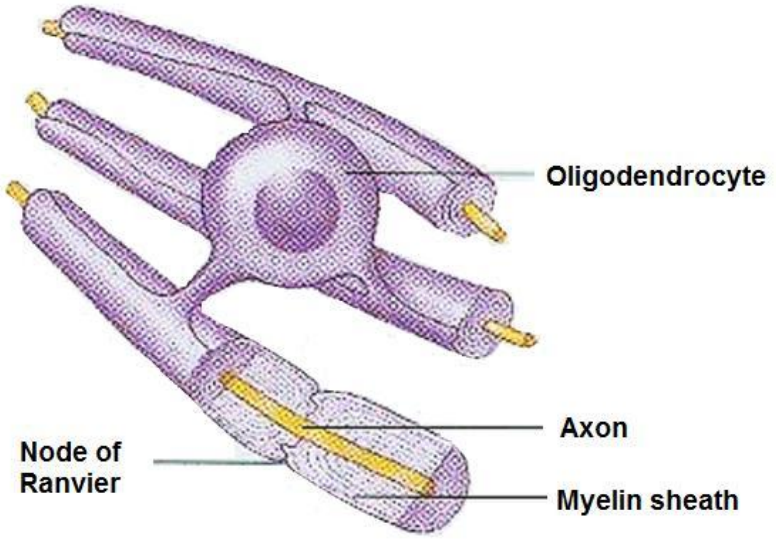

Figure 11:Oligodendrocytes,[3]

Unlike the Schwann cells which form the myelin of a single internodes, each oligodendrocyte myelinates numerous internodes on multiple axons. In routine sections oligodendrocytes are recognizable by their small rounded lymphocyte-like nuclei often in linear arrays. Injury to oligodendrocytes is a feature of acquired demyelinating disorder (e.g. multiple sclerosis) it is also seen in the leukodystrophies, [7].

6.2.3 Ependymal cells

Ependymal cells line the ventricular systems, Figure 12. They are closely related to the cuboidal cells comprising the choroids plexus which secretes the cerebrospinal fluid that circulates through the ventricles of the brain,[7].

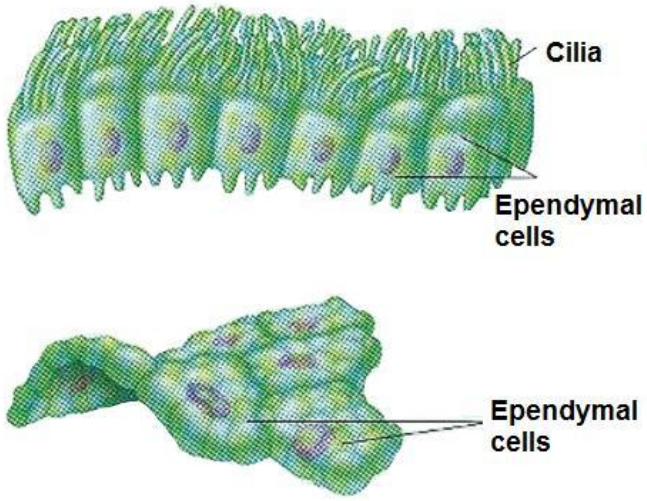

Figure 12: Ependymal cells,[7]

The free surface of the ependymal cells frequently has patches of cilia that assist in moving cerebrospinal fluid through the cavities of the brain.

6.3 Microglia

Microglia are mesoderm derived cells. Its primary functions are to serve as a local defense against foreign objects (macrophage system) in the CNS Figure 13.

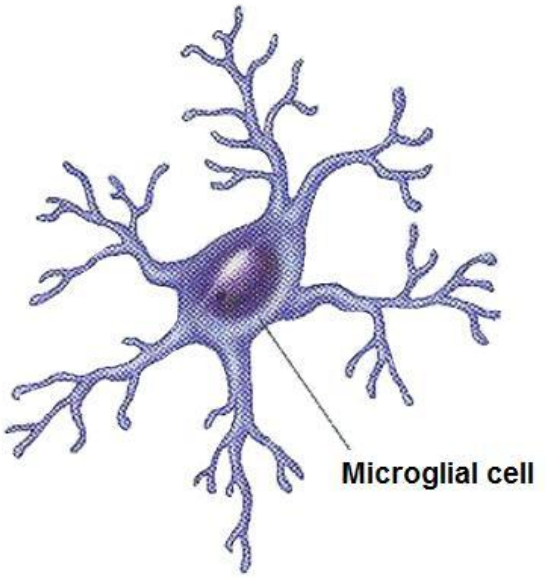

Figure 13:Microglia,[7]

Microglias respond to injury by proliferation and develop elongated nuclei and form aggregates about small foci of tissue necrosis. They also congregate around cell bodies of dying neurons. In addition to resident microglia, blood – derived macrophages are the principal phagocytic cells present in inflammatory foci.

7 Basic Physiology of the Brain

The nervous system is subdivided in to the central nervous system (CNS) which is the brain and the spinal cord and the peripheral nervous system (PNS) which is external to the CNS. The nervous system is involved in some way in most body functions. The major functions of the nervous system are sensory input integration, homeostasis and mental activity as well as muscle and gland control[1]. All these functions are based on nerve signals or cell communications. The fundamental task of the neuron is to receive, conduct and transmit signals. To perform these functions neurons in general are extremely elongated. A single nerve cell in a human being extending from the spinal cord to a muscle in the foot may be a meter long with thin processes radiating outward from it. Usually there is one long axon to conduct signals away from the cell body toward distant targets and several shorter branching dendrites which extend from the cell body like antennae and provide an enlarged surface area to receive signals from the axons of the other verve cells. Signals are also received on the cell body itself. The axon commonly divides at its far end into many branches and so can pass on its message to many target cells simultaneously. Likewise the extent of branching of the dendrites can be very great in some cases sufficient to receive as many as 100.000 inputs on a single neuron [5].

7.1 Cell communication

There are two ways in which human cells can communicate firstly by secreting chemical signals e.g. communication between neuron in the CNS and secondly by contact-dependent signals via membrane-bound molecules e.g. between cells in the heart muscle [5].

7.1.1 Chemical signaling

Signaling molecules, that a cell secretes can be destined for a distant target or can be meant to act as local mediators affecting only cells in the immediate environment of the signaling cells. These different types of signaling are divided into three categories: paracrine, endocrine and synaptic signaling [5] .

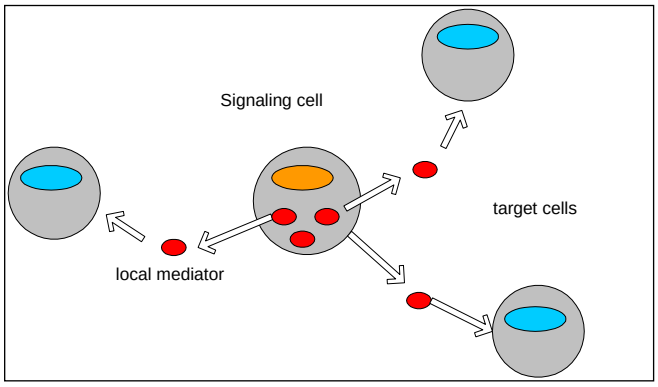

Figure 14: Paracrine signalling

The paracrine signaling, Figure 14, affects only cells in the immediate environment of the signaling cells while the endocrine signaling appears to function much in a similar way, Figure 15, the difference lies in the pathway of the signaling molecule.

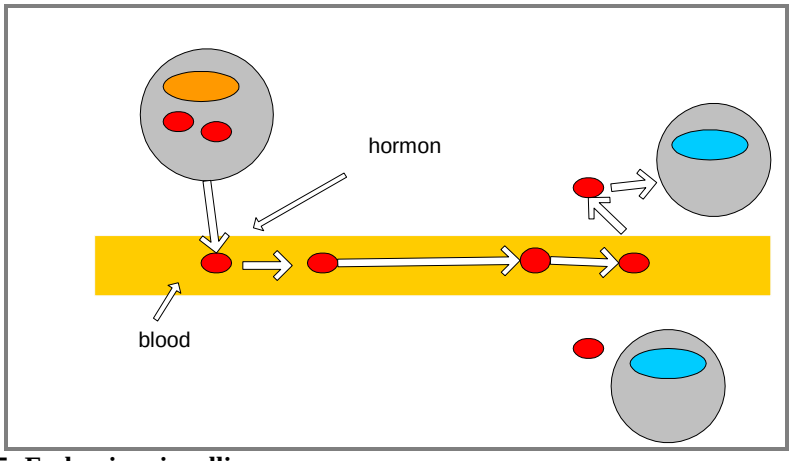

Figure 15: Endocrine signalling

Signaling molecules from endocrine cells need to travel longer distances to reach their target cells. The endocrine signaling cells secrete their signaling molecules, called hormones, into the bloodstream which carries the signal to target cells distributed widely throughout the body.

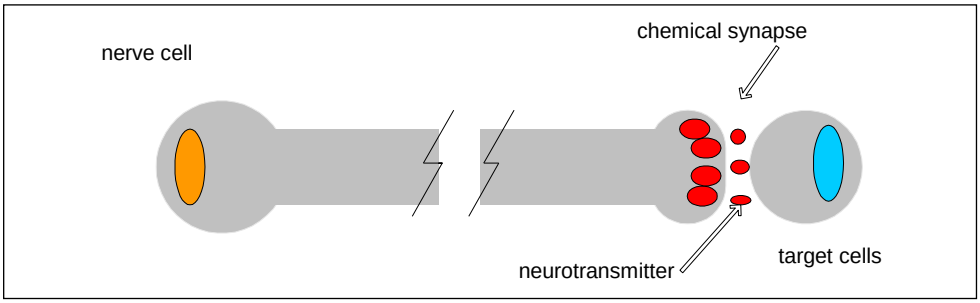

Figure 16: Synaptic signalling

The synaptic signaling process, Figure 16, is used by neurons in the CNS. When activated by signals from the environment or from other nerve cells, a neuron sends electrical impulses or action potential along its axon. When an impulse reaches the nerve terminals at the end of the axon; it stimulates the terminals to secrete a chemical signal called a neurotransmitter [5]. The nerve terminals contact their target cell at specialized cell junction called chemical synapses, which are designed to ensure that the neurotransmitter is delivered to the postsynaptic target cell rapidly, and specifically [5].

7.1.2 Neuronal signals

Neuronal signals are transmitted from cell to cell at specialized sites of contact known as synapses. The usual mechanism of transmission is indirect. The cells are electrically isolated from one another, the presynaptic cell being separated from the postsynaptic cell by a narrow synaptic cleft. A change of electrical potential in the presynaptic cell triggers it to release a small signaling molecule

knows as a neurotransmitter which is stored in membrane-bounded synaptic vesicles and is released by exocytosis. The neurotransmitter rapidly diffuses across the synaptic cleft and provoked an electrical change in the postsynaptic cell by binding to transmitter-gated ion channels. After the neurotransmitter has been secreted, it is rapidly removed either by specific enzymes in the synaptic cleft or by re-uptake either by the nerve terminal that released it or by surrounding glial cells. Re-uptake is mediated by a variety of Na+ dependent neurotransmitter carrier proteins. Rapid removal ensures both spatial and temporal precision of signaling at a synapse. It prevents the neurotransmitter from influencing neighboring cells and clears the synaptic cleft before the next pulse of neurotransmitter. That ensures that repeated rapid signaling events can be accurately communicated to the postsynaptic cell. Signaling trough chemical synapses is far more versatile and adaptable than direct electrical coupling via gap junctions at electrical synapse, which are also used by neurons but to a much lesser extent [8].

Transmitter gated ion channels are specialized for rapidly converting extracellular chemical signals into electrical signals at chemical synapses. The channels are concentrated in the plasma membrane of the postsynaptic cell in the region of the synapse and open transiently in response to the binding of neurotransmitter molecules thereby producing a brief permeability change in the membrane. Unlike the voltage-gated channels responsible for action potentials, transmitter gated channels are relatively insensitive to the membrane potential and therefore cannot by themselves produce a self-amplifying excitation. Instead they produce local permeability changes and exchanges of membrane potential that are graded according to how much neurotransmitter is released at the synapse and how long it persists there. An action potential can be triggered from this site only if the local membrane

potential increases enough to open a sufficient number of nearby voltage-gated cation channels that are present in the same target cell membrane [8].

7.2 Cells and action potentials

Voltage-gated action channels are responsible for the generation of action potentials in electrically excitable cells. The plasma membrane of all electrically excitable cells, not only neurons but also muscle, endocrine and egg cells contain voltage gated cation channels which are responsible for generating the action potentials. An action potential is triggered by a depolarization of the plasma membrane that is by a shift in the membrane potential to a less negative value. However, for an action potential to be triggered there has to be a difference between the solute inside the cell as opposed to the outside of the cell. This difference is maintained by a carrier protein in the lipid bilayer of the membrane of the cells as well as in the membrane of the sarcoplasmic reticulum, collectively called ion-pumps [8].

7.2.1 The plasma membrane $Na^+ - K^+$ pump

The concentration of K^+ is typically 10 -20 times higher inside cells than outside whereas the reverse is true of Na^+. The Na^+- K^+ -pumps maintain this concentration difference and are found in the plasma membrane of virtually all animal cells ,[8]. The pumps operate as an antiporter actively pumping Na^+against its steep electrochemical gradient and pumping K^+ in. The Na^+ gradient produced by the pump regulates cell volume through osmotic effects and is exploited to drive transport of sugars and amino acids into the cell. Almost one-third of the energy requirement of a typical animal cell is consumed in fuelling this pump, as electrically active nerve cells are

repeatedly gaining small amounts of $Na^{+}$and losing small amounts of K^{+} during the propagation of nerve impulses.

7.2.2 Cell Ca^{++} pumps

Eukaryotic cells maintain very low concentrations of free Ca^{++} in their cytosol (10^{-7}) in the face of much higher extracellular Ca^{++}concentrations (10^{-3}). Even a small influx of Ca^{++}significantly increases the concentration of free Ca^{++}in the cytosol and the flow of Ca^{++}down its steep concentration gradient in response to extracellular signals in way of transmitting these signals rapidly across the plasma membrane. The maintenance of a steep Ca^{++} gradient is therefore important to the cell. Ca^{++}-channel pumps in the plasma membrane that actively transports Ca^{++} out of the cell help maintain the Ca^{++}gradient. One of these pumps is an ATPase while the other is an antiporter that is driven by the Na+ electrochemical gradient. The best understood Ca^{++}pump is a membrane-bound ATPase in the sarcoplasmic reticulum of muscle cells. The sarcoplasmic reticulum, a specialized type of endoplasmic reticulum forms a network of tubular sacs in the cytoplasm of muscle cells and serves as an intracellular store of Ca^{++} (When an action potential depolarizes the muscle cell membrane, Ca^{++} is released from the sarcoplasmic reticulum into the cytosol stimulating the muscle to contract). The Ca^{++}pump which accounts for about 90% of the membrane protein of the organelle is responsible for pumping $Ca^{++}$from the cytosol into the sarcoplasmic reticulum ,[8].

7.2.3 The generation of action potential

Despite the varied significance of the signals carried by different classes of neurons the form of the signals is always the same consisting of changes in the electrical potential across the neurons plasma membrane. Communication occurs because an electrical disturbance produced in one part of the cell spreads to other parts. Such a disturbance becomes weaker with increasing distance from its source unless energy is expended to amplify it as it travels. Over short distance, this attenuation is unimportant in fact many small neurons conduct their signals passively without amplification. For long-distance communication however passive spread is inadequate. Thus larger neurons employ an active signaling mechanism which is one of their most striking features an electrical stimulus that exceeds certain threshold strength triggers an explosion of electrical activity that is propagated rapidly along the neurons plasma membrane and is sustained by automatic amplification all along the way. This travelling wave of electrical excitation known as an action potential or nerve impulse can carry a message without attenuation from one end of a neuron to the other at speed as great as 100 meter/second or more. Action potentials are a direct consequence of the properties of voltage –gated action channels [8] .

In nerve and skeletal muscle cells, a stimulus that causes sufficient depolarization promptly cause voltage-gated Na^+ channels to open, allowing a small amount of Na^+ to enter the cell down its electrochemical gradient. The influx of positive charge depolarised the membrane further thereby opening more Na^+ channels which admit more Na^+ channels which admit more Na^+ ions causing still further depolarization. This process continues in a self-amplifying fashion until within a fraction of a second the electrical potential in the local region of the membrane has shifted from its resign value of about -

70mV almost as far as the Na^+ equilibrium potential of about + 50mV. At this point when the net electrochemical driving force for the flow of Na^+ is almost zero the cell would come to a new resting state with all of its Na^+ channels permanently open if the open conformation of the channels were stable. The cell is saved from such a permanent electrical spasm because the Na^+ channels have an automatic inactivating mechanism which causes the channels to reclose rapidly even though the membrane is still depolarized. The Na^+channels remain in this inactivated state unable to reopen until a few milliseconds after the membrane potential returns to its initial negative value, figure 19.

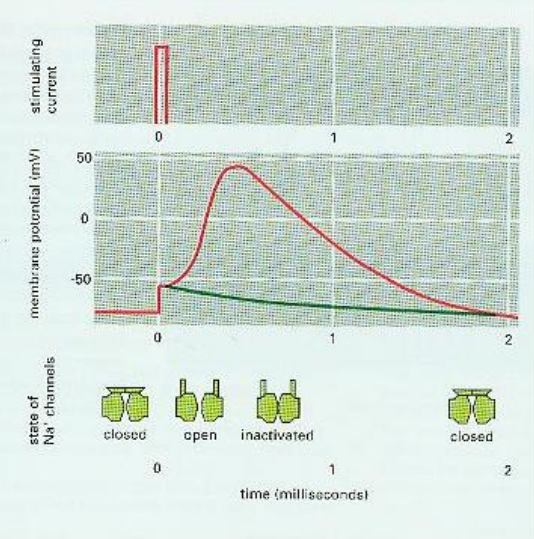

Figure 17: Action potential. Action potential is triggered by a brief pulse of current (the upper graph), which partially depolarizes the membrane (lower graph). The green curve shows how the membrane would relax back to the resting value after the initial depolarizing stimulus if there had been no voltage-gated ion channels in the membrane. This slow return of the membrane potential to its initial value of -70 mV in the absence of open Na+ channels is automatic because of the efflux of K+ through K+ channels, which drives the membrane back toward K+ equilibrium potential. The red curve shows the course of the action potential that is caused by the opening and subsequent inactivation of voltage-gated Na+ channels whose state is shown at the bottom. The membrane cannot fire a second action potential until the Na+ channels have returned to the closed conformation. Until then the membrane is refractory to stimulation [8].

The above description of an action potential concerns only a small patch of plasma membrane. This self-amplifying depolarization of the patch however is sufficient to depolarize neighboring regions of membrane, which then go through the same cycle. In this way, the action potential spreads as travelling wave from the initial site of depolarization to involve the entire plasma membrane. In addition to the inactivation Na^+ channels in many nerve cells, a second mechanism operates to help bring the activated plasma membrane more rapidly back toward its original negative potential, ready to transmit a second impulse. Voltage gated K^+ channels open so that the transient influx of Na^+ is rapidly overwhelmed by an efflux of K^+which quickly drives the membrane back toward the K^+equilibrium potential even before the inactivation of the Na^+ channels is complete. These K^+channels respond to changes in the membrane potential in much the same way as the Na^+ channels do but with slightly slower kinetics. Because of this slow onset, these channels are sometimes called delayed K^+channels ,[8].

7.3 Myelination

The axons of many vertebrate neurons are insulated by a myelin sheath, which greatly increases the rate at which an axon can conduct an action potential. The importance of mediation is dramatically demonstrated by the demyelinating disease multiple sclerosis in which myelin sheaths in some regions of the central nervous system is destroyed by an unknown mechanism. Where this happens, the propagation of nerve impulses is greatly slowed often with devastating neurological consequences [8]. Myelin is formed by specialized supporting cells called glial-cells (see previous discussion of histology). The glial cells are the Schwann cells in peripheral nerves and Oligodendrocytes in the central nervous system. These glial cells wrap layer

upon layer of their own plasma membrane in a tight spiral around the axon thereby insulating the axonal membrane so that almost no current leaks across it. The sheath is interrupted at regularly spaced nodes of Ranvier where almost all the Na+ channels in the axon are concentrated. Because the unsheathed portions of the axon membrane have excellent cable properties, a depolarization of the membrane at one node almost immediately spreads passively to the next node. Thus, an action potential propagated along a myelinated axon by jumping from node to node, a process called saltatory conduction. This type of conduction has two main advantages action potential travels faster and metabolic energy is conserved because the active excitation is confined to the small regions of axonal plasma membrane at nodes of Ranvier ,[8].

7.4 Transport of substances through the cell membrane

All molecules and ions in the body fluids, including water molecules and dissolved substances, are in constant motion, each particle moving its own separate way. Motion of these particles is what physics call "heat" –the greater the motion the higher the temperature –and the motion never ceases under any conditions except at absolute zero temperature [1]. Diffusion is the continual movement of molecules among one another in liquids or in gases. Ions diffuse in the same manner as whole molecules and even suspended colloid particles diffuse in similar manner except that the colloids diffuse far less rapidly than molecular substances because of their larger size.

Diffusion through the cell membrane is divided into two subtypes called simple diffusion and facilitated diffusion [1]. Simple diffusion means that kinetic movements of molecules or ions occur through a membrane opening or through intermolecular spaces without any interaction with carrier proteins in

the membrane. Simple diffusion happens by two pathways 1) through the interstices of the lipid bilayer if the diffusing substance is lipid soluble and 2) through watery channels that penetrate all the way through like some of the large transport proteins [1]. Facilitated diffusion requires interaction of a carrier protein. The carrier protein aids passages of the molecules or ions through the membrane by binding chemically with them and shuttling them through the membrane in this form [1].

7.5 Diffusion of lipid-soluble substances across membranes

The most important factors that determine how rapidly a substance diffuses through the lipid bilayer are the lipid solubility of the substance. For instance the lipid solubility of oxygen nitrogen is high so that oxygen can dissolve directly in the lipid bilayer and diffuse through the cell membrane. Large amounts of oxygen can be transported to the interior of the cell almost as though the cell membrane did not exist [1].

7.6 Diffusion across a membrane

Known as Brownian motion, molecules in gases as well as dissolved molecules and ions in a liquid (solvent) are moving constantly around in a random fashion as a result of their thermal energy [6]. If any differences in solute concentration exist anywhere in the solution there will be a net movement i.e., net diffusion along the concentration gradient until all differences are eliminated [6]. As a result of a membrane semi-permeable function and the Na/K pump actions a cell inside is negatively charged compared to the outside. This transverse difference in voltage is known as the membrane potential. The equilibrium potential is between –70-100 milli-Volts

(mV). This potential can be calculated for an i.e., K+ ion by using the Nernst equation:

$$\Delta\Psi_k = \frac{61}{n} * \log\left(\frac{C_o}{C_i}\right)$$

Nernst equation

- Where Co/Ci= concentration outside/inside
- n=ion valence, $\Delta\Psi_{k=}$ equilibrium potential in mV for the ion K+ [6].

Nernst equation is extremely important in understanding the transmission of nerve impulse [1].

8 Alzheimer's disease

Alois Alzheimer was the first to describe the neuropathological findings in 1907 that are now known as Alzheimer's disease (AD) [9]. AD is a neurodegenerative disease characterized by progressive cognitive deterioration along with a decline in activities of daily life. The early symptom of AD is memory loss (amnesia), which starts as minor forgetfulness that becomes steadily more pronounced as the illness progresses, but with relative preservation of older memories [1]. As the disease progresses further, cognitive impairment extends to the domains of language(aphasia), learned motor skills (apraxia), recognition (agnosia), mathematical skills and functions related to the frontal and temporal lobes affecting for example decision-making and planning [1]. Other common clinical symptoms are agitation, aggression, sleep disturbances and social withdrawal [10]. AD is the most common type of dementia, affecting about 50% of those above 85 years of age [9]. Currently, there is no cure for AD.

8.1 Cellular pathology of Alzheimer

The pathology of the AD brain is characterised by amyloid-beta-peptide (Aβ) that forms plaques in neurones and other cell types of the brain [11]. Figure 18 shows a schematic of the senile plaque and how it entangles the cells of the brain tissue.

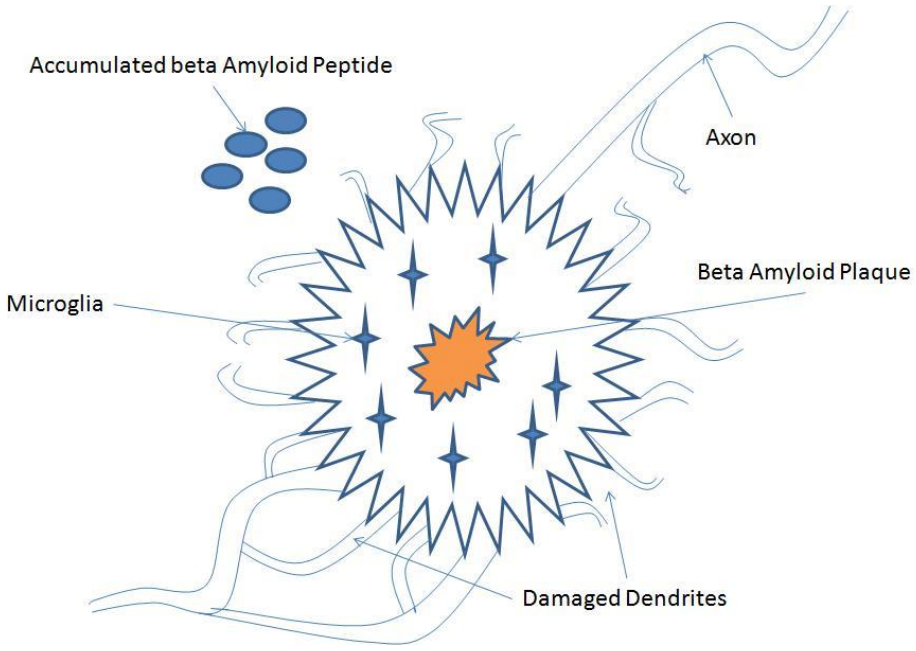

Figure 18: Schematic of a senile plaque.

The aetiology of AD is currently not clearly understood, however the accumulation of Aβ is likely to play an important role in the pathogenesis of AD [11].

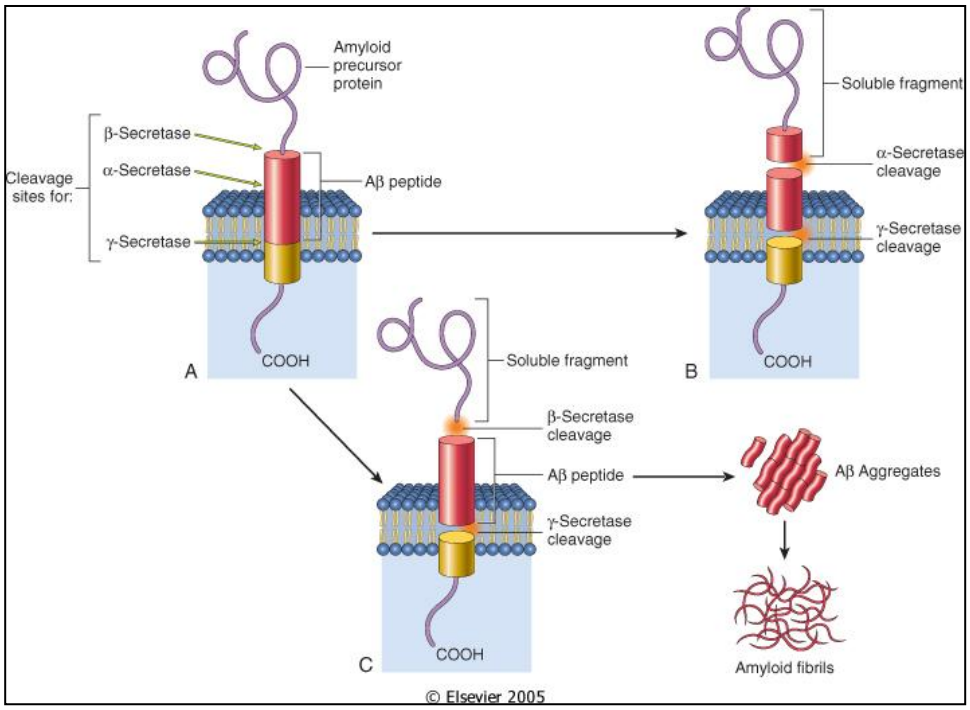

Figure 19: Mechanism of amyloid generation. Amyloid Precursor Protein (APP) is a transmembrane protein with a potential cleavage for three distinct enzymes (α-, β-, γ-secretases) as shown in A. The Aβ domain extends from the extracellular site of the protein into the transmembrane domain. If APP is cleaved by the α-secretase (B), then a subsequent cleavage by γ-secretase will not yield Aβ. On the other hand a cleavage by β-secretase followed by the γ-secretase (C) produces Aβ, which aggregates and forms fibrils [1].

The current understanding of AD has been led by the research into properties of Aβ. This derived from APP which is a transmembrane protein with a potential cleavage for three distinct enzymes (α-, β-, γ- secretases), Figure 19. The Aβ domain extends from the extracellular site of the protein into the transmembrane domain. When APP is cleaved by the α-secretase and subsequently cleaved by γ-secretase the product is not Aβ. In contrast, cleavage by β-site cleaving enzyme 1 (BACE1) followed by the γ-secretase does result in production of Aβ, which can aggregate and form fibrils [11]. Amyloid fibrils form the core of several kinds of senile plaques including those found in AD [12]. Because BACE1 initiates the formation of Aβ factors

that elevate the levels of this particular intracellular enzyme may promote AD. Recent studies have shown that BACE1 levels are indeed increased in post-mortem AD brains. The increase of BACE1 has been found primarily in the neurons at the presynaptic structure [11]. It has also been found that the amyloid plaques include BACE1 in the surrounding neurons at early stages of the pathology resulting in a positive-feedback loop, even before any neuron death occurs [11].

8.1.1 Hypoperfusion and beta-amyloid

The function of the brain depends on the correct balance of glucose and oxygen through blood flow and the energy demands imposed by the neural activity. As described above, Aβ is believed to be of great importance in AD pathogenesis. Whether it contributes directly or indirectly to the vascular factors observed in AD has not been established, although recent findings indicate that Aβ does exert vasoactive effects[13]. The regulation of cerebral blood flow distribution of specific regions depending on demand is called functional hyperaemia and is largely controlled by neurovascular units (NV). The NV unit is composed of perivascular neurones, astrocytes, endothelial cells and vascular smooth muscle cells. There is evidence suggesting a dysfunction of the NV unit during the early stages of AD [14]. Research has also shown that Aβ has direct effect on vasculature in mice as well as a reduction in the response of CBF to somatosensory activation [15].This failure in CBF appeared before amyloid plaques appeared in the vasculature. The reduction of CBF was a result of soluble Aβ causing vasoconstriction and reducing vasodilatation [15]. Other researchers have found that Aβ impacts cerebrovascular function only after vascular deposition [13]. However cerebrovascular pathology, including cerebral amyloid angiopathy (CAA), is

frequently observed in AD patients and can lead to vascular weakening of the vessels involved , sometimes leading to haemorrhagic stroke and ischemic infarcts, both risk factors for AD [13].

8.1.2 Energy deficiency and beta-amyloid

Although the function of BACE1 and APP is unclear both have been implicated in the stress/injury response [16]. The formation of Aβ is through cleavage of APP by BACE1. It has been established that BACE1 is the rate-limiting enzyme for the production of Aβ [17]. The reason for the increase of BACE1 is, however, unknown. It been observed that cerebral glucose and blood flow are both reduced in preclinical AD [16]. Furthermore, diminished brain glucose metabolism has also been reported in patients with mild cognitive impairment (MCI) suggesting that insufficient energy production may be a factor in preclinical AD [18]. These observations led to the discovery that impaired energy production does indeed lead to increase of BACE1 thereby leading to overproduction of Aβ in the brain [16].

8.1.3 Hypoxia and beta-amyloid

Recent studies have shown that a history of stroke can increase AD prevalence two-fold among elderly patients [19]. Chronic brain hypoperfusion is a preclinical condition of MCI a condition believed to precede AD development [13]. Hypoxia is a direct consequence of hypoperfusion and may play an important role in AD pathogenesis [19]. In a study conducted by Sun and colleagues it was found that hypoxia significantly increased BACE1 gene expression resulting in increased β-secretase activity and Aβ production. Furthermore, hypoxia was shown to markedly increase Aβ deposition and

neuritic plaque formation as well as potentiate the memory deficit of Swedish mutant APP mice. These results therefore indicate that hypoxia can facilitate the pathogenesis of AD [19]. Chronic hypoxia results in significant cellular adaption. An important component of this functional adaptation is an altered ion channel expression. Oxygen has been known to alter the state of cells in the carotid body which is a small organ that detects changes in the blood gas and pH levels in the body. This is done through oxygen-sensitive K+ (potassium) channels found in type I cells of the carotid body. The sensitive K^+ channels of type I cells are active at normal resting membrane potential. When the oxygen level fall, the K^+ channel activity decreases and the type I cells depolarise. Such depolarization causes voltage gated Ca^{++}(Calcium) channels to open, permitting Ca^{++} influx which triggers exocytosis of sensory neurones [20] . Rats have at least two distinct K+ channels that respond to hypoxia thus causing depolarisations. Firstly, a high-conductance Ca^{++}-activated K^+ (BK) channel and secondly an acid-sensitive tandem domain K^+ channel (TASK) [20]. Since these initial discoveries oxygen sensitive channels have emerged in a wide variety of cell types. In neurones, BK and TASK channels have a strong negative influence on excitability. The inhibition of the BK and TASK channels by hypoxia therefore leads to cell depolarisation which may account for excitotoxicity associated with the excessive glutamate release [20]. Studies on the reaction of PC12 cells to a reduction of oxygen showed that hypoxia induced a Cd^{++} (Cd^{++} is a non-selective Ca^{++} channel blocker) resistant Ca^{++} entry pathway into the cell coupled to catecholamine release. These pathways were found to be formed by Aβ-peptides believed to be connected to AD [20]. Oxygen is undoubtedly an active physiological regulator of numerous ion channels. Evidence suggests that alteration of ion channel expression by chronic hypoxia occur at various levels in the life-cycle of specific channel proteins. Immuno-cytochemical

studies have now confirmed that chronic hypoxia does indeed cause a dramatic increase of Aβ-peptide in the plasma membrane of hypoxic PC12 cells [20].

8.2 Watershed Zones

At the arterial tree periphery lies what is known as the watershed zone. In the cerebral hemispheres, this is most significant at the border zone between the anterior and posterior circulation. This area plays a role in the pathogenesis of watershed infarcts, which are the formation of sickle-shaped band of tissue necrosis in the brain, most commonly associated with episodes of hypotension and decreased blood blow [1]. Other mechanisms include micro-embolism and uni-lateral carotid occlusion resulting in decreased overall perfusion of the brain arterial tree. Watershed infarcts constitute approximately 10% of all brain infarcts [21].

The significance of the watershed zones in stroke syndromes and the possible pathogenesis in the development of AD has been a matter of more recent investigation. MRI studies have demonstrated lesions in the watershed areas of the brain in patients with stenosis of their carotid artery, who presented to hospital with a stroke. Many of the patients with a unilateral lesion of a carotid artery had bilateral lesions in the watershed areas, suggesting a haemodynamic insufficiency of the arterial tree [22].

Oda-Christina et al, put forward the hypothesis that cortical watershed microinfarcts should be common in AD. This hypothesis was based on the known association of AD and cerebral hypoperfusion and the established fact that the watershed zones are the first to be deprived of blood flow in the event of cerebral hypoperfusion. They performed brain autopsies on 105 patients with definite AD and 79 age-matched controls. They found a significant association between watershed infarcts and AD, with an occurrence of 32.4%

versus 2.5% in controls. They therefore concluded that not only does cerebral hypoperfusion induce white matter changes in AD, but also produces cortical watershed infarcts, further aggravating the dementia process [23], but there may be a number of confounding variables in this analysis.

8.3 Causes and treatment of Alzheimer's

It is likely that the cause of AD results from multiple environmental and genetic factors that affect both the production and clearance of Aβ in the brain. The importance of the vascular system and CBF in relations to the development of AD is addressed in Figure 20.

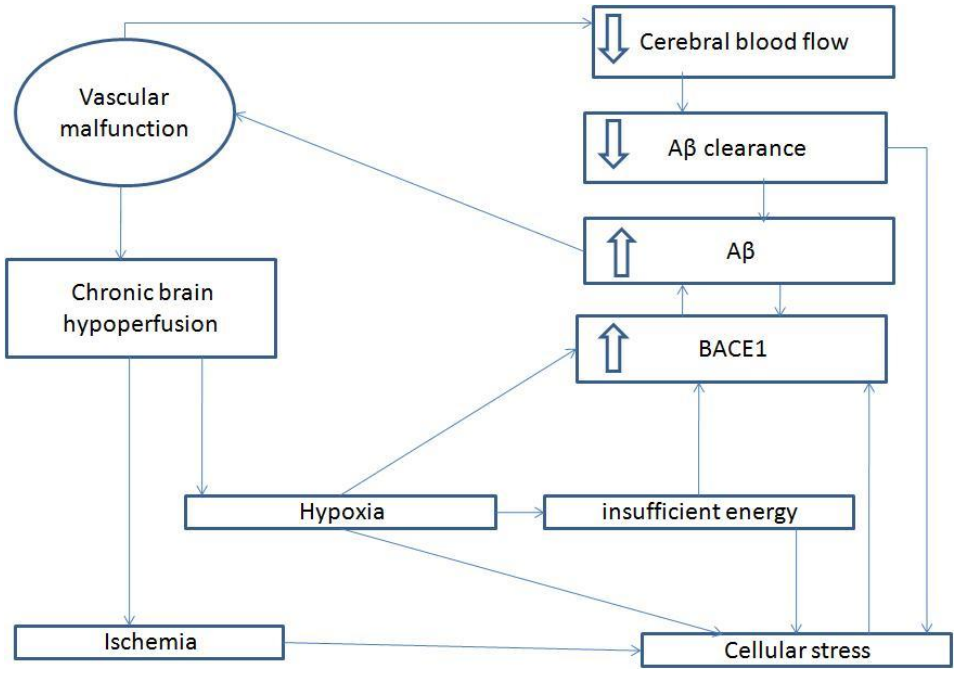

Figure 20: AD and the connection to vascular circulation. Vascular malfunction (such as occlusion or stenosis of a vessel in the circle of Willis) will directly affect the cerebral blood flow (CBF) as well as having the potential to cause chronic hypoperfusion resulting in hypoxia/ischemia. Decreased CBF will result in reduction of Aβ clearance, while hypoxia will result in increase of BACE1 enzyme which will cause an increase in Aβ production [24].

In the case of vascular malfunction (such as occlusion or stenosis of a vessel in the vascular system, for example in the circle of Willis), the direct effect will be a decreased cerebral blood flow (CBF). In the case of occlusion a state of chronic hypo-perfusion will result in hypoxia or ischemia. Studies have now shown that decreased CBF will result in the reduction of Aβ clearance as explained earlier, while hypoxia will result in an increase of BACE1 enzyme which will cause an increase in Aβ production.

There is no cure available for patients suffering from AD although medications are available that target neurotransmitters, mainly acetylcholine (Ach) or cholinesterase inhibitors. These drugs exert their effect by impeding the enzyme cholinesterase from breaking down Ach, believed to be essential for inter-neuronal communication [9]. Treating AD indirectly through increasing CBF has shown some promise. A controversial treatment where the omentum is surgically implanted directly on the brain of a AD patient has been shown to increase CBF and in some cases reverse the AD symptoms [9].

In closing we note that the development of AD is extremely complicated with many different factors contributing to the pathology. However the focus of interest is increasingly shifting towards blood flow and perfusion through the brain tissue.

9 Binary Tree

When representing relationship between data, binary tree data structure is quite useful. All binary trees are hierarchical in nature, meaning that a parent-child relationship exists between the nodes of the tree,

Figure **21**.

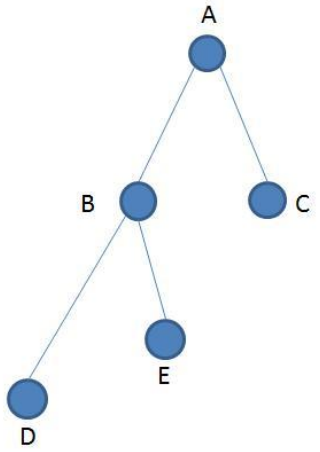

Figure 21: Binary tree structure

If node *n* is above node *m* in the tree then node *n* is the parent of the node *m* and node *m* is the child of the node *n*. In

Figure **21** the node *A* is parent of nodes *B* and *C*, where *B* and *C* are siblings. Each node in the tree has at most one parent. Each binary tree has only one node called the *root*, being the root of the tree. The root has no parents and in

Figure **21** , node A is the root of the tree. Nodes that have no children are called leaves and in

Figure **21** nodes *D, E* and *C* represent the leaves of the binary tree. Leaves of binary trees are also referred to as the terminal nodes of a tree [25]

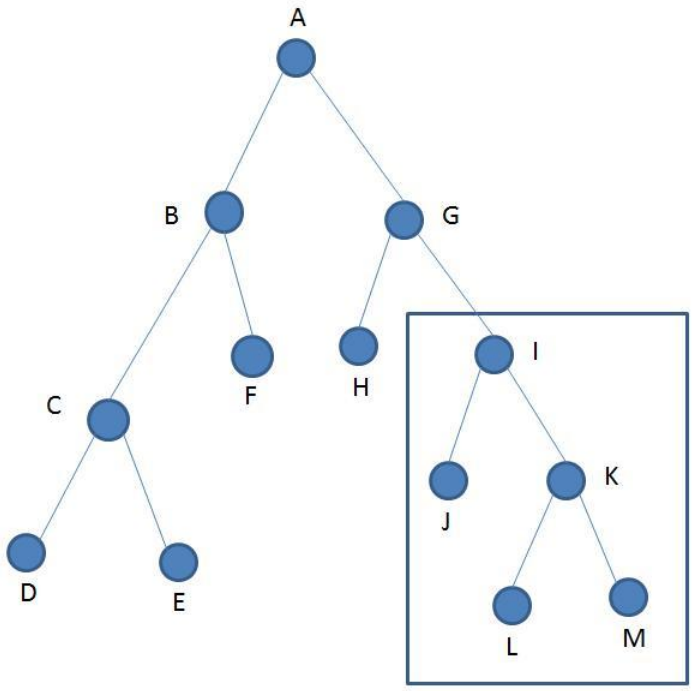

Figure 22: Binary subtree

A binary tree can be divided into subsets of smaller trees. Generally a binary tree is a set of one or more nodes such that the tree can be partitioned into disjoint subsets with a single root and sets that are in itself, binary trees and are called subtrees of the root [26]. Figure 22 demonstrates the relationship between a whole binary tree and its subtrees. A box has been drawn around a potential subtree in Figure 22 , where the node *I* is the subtrees root and nodes *J* and *K* its children.

10 Literature review

Ever since William Harvey established the idea of the circulation of blood in the year 1628, scientists have attempted to gain insight into the physiological and physical relationship between the elements that drive the blood in the extremely complicated anatomical structure of the vascular system. A century after Harvey's idea it was recognized by Hales in 1733 that the intermittent flow from the left ventricle was transformed into a steadier outflow. Hales described the whole arterial system as being one elastic chamber, which was later known as the Windkessel model[27]. The function and structure of the arterial system has intrigued scientists ever since, and an answer to the question of what governs the architecture of the circulation has been pursued.

The spatial branching pattern of an arterial model for the brain is the focus of this thesis. We have attempted to build a computer simulation model (SM) based on the Constrained Constructive Optimization (CCO) model of Schreiner et al [25, 28]. Their model realistically simulates the structure of the arteries of the brain as well as producing realistic results of pressure and flow rate for the tree structure. Specific arterial models of the cerebrovascular tree are hard to find in the literature, since this is a relatively new field of research. Lauwers et al [29] recently examined the arterial structure of the cerebral cortex; To the best of our knowledge this is the first study to specifically focus on the arterial structure of the brain. A likely reason for the lack of research specifically aimed at the arterial structure in the brain is that the branching of arteries is found to be similar in all the organs of the body, presumably since the blood flow is guided by the exact requirements of each organ[6]. The brain requires a constant supply of oxygen and glucose; however the distribution is not equal throughout the brain tissue. The grey matter receives up to four times the amount of blood flow compared with the white matter [6]. The reason

being that the grey matter holds the cell bodies of neurons and therefore has a higher metabolic demand than the white matter. The organ that receives the most blood flow per weight is perhaps surprisingly not the brain, but the kidneys, with an average of 360 ml/min/100gr tissue, compared to 50ml/min/100gr in the brain. This is understandable when the kidneys role in excretion of waste products is considered. The brain receives a fair share of the total cardiac output or a flow of around 750-900 ml/min [6].

10.1 Arterial branching classification

Mair Zamir has contributed much to the research of arterial structure and properties of arterial trees. In 1988 Zamir et al conducted research on the arterial network in rats [30]. An arterial tree of 1313 arterial vessels was mapped and divided into well-defined levels. The length and diameter of the arteries were measured. They established that the most common mode of branching was the dichotomous mode where the parent vessel divides into two daughter vessels. Zamir et al also proposed a different classification of a vessel and the levels in an arterial tree than the one used at that time. They abandoned the concept that an arterial tree is composed of distinct whole vessels and instead adopted the view that at a branching site a vessel changes its diameter as well as its identity regardless of the size of the branch. Zamir et al proposed the use of the word vessel-segment rather than vessel for an individual arterial vessel. This method is different from the classification sometimes used for arterial trees called Strahler's Method[31] where branches of the same properties are grouped together to form different levels of a tree. Strahler's method is commonly used in the classification of rivers but is now also utilized in classifying arterial tree structures [6]. However, the classification

suggested by Zamir and Phipps [32] is the one used for this thesis work, and the vessels in this thesis are referred to as segments.

10.2 Arterial bifurcation and Murray's law

The arrangement of branching vasculature in mammals has been found to largely obey Murray‘s law, which states that the cube of the radius of a parent vessel equals the sum of the cube of the radii of the daughters [33]. The Poiseuille relationship states that under appropriate hemodynamic conditions in isolated vessels, blood flow is proportional to the fourth power of the vessels diameter. Using Poiseuille‘s relationship Murray states: „the total work involved in the circulation of blood in a section of an artery, sufficiently small so that the pulsating changes in the kinetic energy of the blood stream in it can be neglected as compared to the work required to overcome friction” [33]. Murray investigated the optimal cost of blood flow in terms of geometric resistance as well as the angle of bifurcation at bifurcation junctions. He derived the following condition for dichotomous arterial trees

$$r_0^3 = r_1^3 + r_2^3 \quad (10.1)$$

Where r_0 denotes the parent radii of an arterial tree and r_1 and r_2 its daughter branch radii [33]. He also derived the following equations

$$cos\theta_1 = \frac{r_0^4 + r_1^4 - r_2^4}{2r_0^2 r_1^2} \quad (10.2)$$

$$cos\theta_2 = \frac{r_0^4 + r_2^4 - r_1^4}{2r_0^2 r_2^2} \quad (10.3)$$

Where $\theta_1$and θ_2 are the branching angles of the daughter branches [33, 34]. He concludes that the theoretical minimum total angle $(\theta_1 + \theta_2)$ for a blood vessel at a simple bifurcation was 75°. He also reported experimental results from a small arterial tree where $x = 3.0$ for the following equation

$$r_0^x = r_1^x + r_2^x + r_3^x \quad (10.4)$$

which supported his previously derived equation. He did however note that the experimental findings were limited to small arterial trees.

This idea of optimal functions determining the angle at arterial junctions was developed further by [32]. He proposed that four minimization functions contributed to the optimal geometrical structure at an arterial junction. These minimal functions are; vascular surface area, vascular volume, drag force stress and power loss. He examined the four optimal principles which were based on the following hypothesis. For the minimum lumen surface the hypothesis states: "An arterial junction is in an optimum state when the total lumen surface of the arteries involved is a minimum" [32]. For the total minimum volume the hypothesis states: "An arterial junction is in an optimum state when the total lumen volume of the arteries involved is a minimum" [32]. For the minimum drag force the hypothesis states: "An arterial junction is in an optimum state when the total drag force acting on its lumen walls is a minimum" [32]. Finally for the minimum power the hypothesis states: "An arterial junction is in an optimum state when the power required for pumping blood through that junction is a minimum". [32]. His hypothesis are summarized in Table 1

Table 1: Four minimisation functions of the optimal bifurcation geometry

Hypothesis	Explanation
Vascular surface area	An arterial junction is in an optimum state when the total lumen surface of the arteries involved is a minimum
Vascular volume	An arterial junction is in an optimum state when the total lumen volume of the arteries involved is a minimum
Drag force	An arterial junction is in an optimum state when the total drag force acting on its lumen walls is a minimum
Power loss	An arterial junction is in an optimum state when the power required for pumping blood through that junction is a minimum

In his research, Zamir investigated the geometries of three different models representing the majority of the arterial bifurcation cases. The first model gives rise to a small vessel without changing its course; the second model is where the vessel is discontinuous and splits into two distinct vessels; and the third one a far less frequent occurrence where a parent artery gives rise to two branches and then proceeds in its original course without a change of direction, Figure 23.

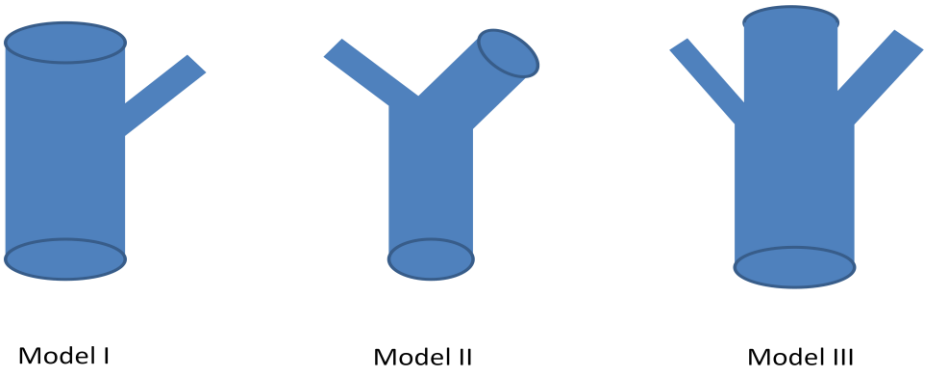

Figure 23: Models used in Zamir's research.

Zamir then applied the four optimization principles on the models. In order to compare the four optimization functions that predicted an angle, Zamir introduced the following area ratio index

$$\beta = \frac{\pi r_1^2 + \pi r_{2..}^2}{\pi r_0^2} \quad (10.5)$$

Zamir discovered a large general difference in the predicted angles using the four optimization principles. However the results did demonstrate that when the area ratio $\beta \approx 1.26$ and the power index is at a constant of $x = 3.0$, the four optimisation principles where closest in the bifurcation angle predictions or within a range of 75°-102°. This turned out to be a unique optimum state where the lumen surface, the lumen volume, the pumping power and the drag force were all close to a minimum. He suggested that in order for an arterial

junction to be in an optimal state all four of the optimal principles ought to be applied simultaneously [32].

Evaluation of Murray's law has been conducted by biologists ever since he published his findings. Suwa et al [35] measured the arteries of humans in 1963 by infusing an acrylic resin at a high pressure, gathering data from various organs including heart, kidney, and lungs. They concluded that the human arteries over a large range in size and organs could be represented by a fixed power exponent of 2.7, see equation 10.4. Furthermore Suwa et al did not find changes in the cross-section data until an arterial diameter of the order 0.5 mm was reached. Later Mayrovitz and Roy set out to determine if in vivo blood flow was in fact related to vessel diameter in the optimal manner originally put forward and whether it was in proportion to the cube of the vessel diameter [36]. The experiment was done on eight male rats, observing the Cremaster muscle. The experimental results strongly suggested a third-power dependence of flow on the diameter.

Zamir et al carried out a study in 1992 of the major branches of the arch of the aorta where he demonstrated that the cubic law might not be suitable for the first generation of the arterial tree, where capacitance and gross anatomy were important [37]. They concluded that the early generation of an arterial tree is governed by a square law rather than a cubic law. Zamir again addressed the question of the fractal properties of arterial trees in 1999 when he investigated the structure of the right coronary arterial tree focusing on its geometrical properties [38]. Through this research Zamir established three properties of the arterial bifurcation. They are; the *bifurcation index* measuring the relationship between the daughter segments in a tree as follows:

$$bifurcation\ ratio = \frac{r_{smaller}}{r_{larger}} \quad (10.6)$$

where $r_{smaller}$ denotes the smaller daughter radius and r_{larger} is the larger daughter radius at any bifurcation; *the area ratio* (β) measuring the cross section area available to the flow as it progresses from the parent segment to the daughter segment; and the *power law index* governing the fluid dynamic efficiency of the bifurcation. Zamir discovered that the value of the bifurcation index α was almost uniformly distributed between 0 and1, Figure 24.

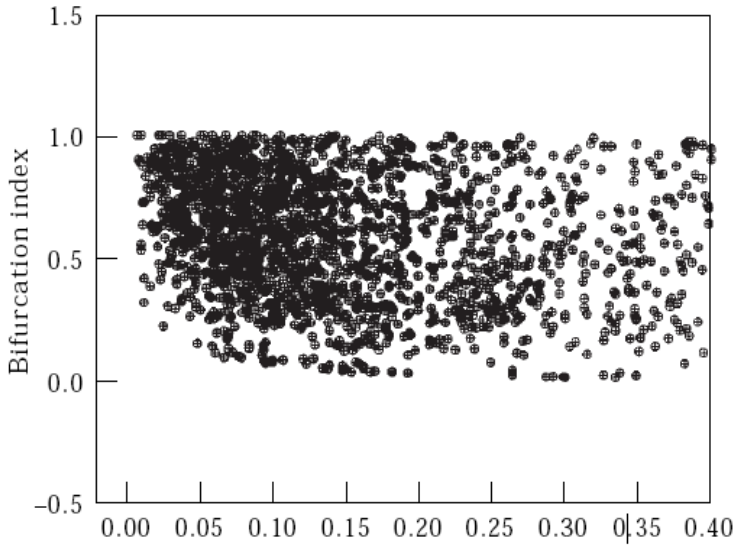

Figure 24: The distribution of bifurcation index in relation to the segments radii [38].

These findings indicated that the arteries deep in the tissue were not mostly symmetrical as had been assumed until then. Zamir also investigated the area ratio β and found it to be highly mixed at all levels of the arterial tree.

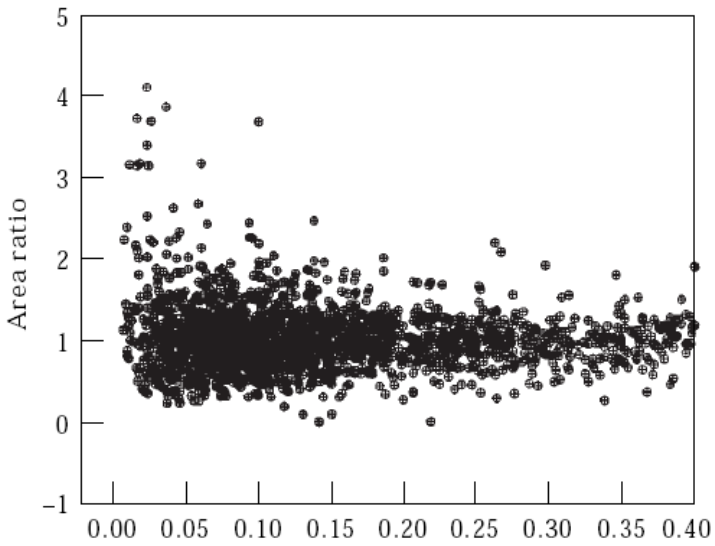

Figure 25: The distribution of the area ratio in relations to the segment radii [38].

However the results also indicated that much of the area expansion occurred within the middle and lower diameter ranges as had been generally assumed, Figure 25. The area expansion did however not occur consistently in this region, but appeared to be accompanied by contractions at other bifurcation areas. Zamir also found the power index, equation 4, ranged between 1 and 3. Based on those findings he suggested that a distinction ought to be made between the vasculature trees of organs with different functional roles, such as the purely metabolic functioning organs, the brain and heart, and the ones that serve a processing function, such as the lungs and kidneys.[38]

10.3 Arterial models

Arterial models can be divided according to spatial properties into zero-dimensional models, two-dimensional and three-dimensional models.

10.3.1 Zero-dimensional models

The zero-dimensional models have the advantage of simplicity and low computational cost. One of the first zero-dimensional models was developed by Avolio in 1980 [27]. By dividing the systemic vasculature into 128 arterial segments and arranging them according to the anatomical architecture of the human arterial system he simulated the systemic arterial system. Peripheral arteries were terminated by a resistance giving a specified reflection coefficient. The basic unit was a segment of artery. The segment was assumed to be a thin-walled uniform cylindrical tube with internal viscous, elastic and inertial properties. This model exhibited the essential features of the muscular system with respect to vascular impedance and distribution of pressure and flow waveforms. The arterial circulation in the brain is not considered here in detail and terminates at the internal cerebral artery by a terminal resistance. Mette Olufsen developed a fractal-structured tree based on the properties of small arteries reported by Zamir [38]. The tree is described using a bifurcating self-similar tree which is characterized by three parameters. The first parameter describes the branching relationship across bifurcations between the radius of the parent vessel and the radii of the daughter vessels using area ratio β or power law exponent k. The second is the asymmetry index describing the relationship between the daughter vessels α, while the third is the length of the arteries [39, 40], Figure 26. The radius of the branches are therefore defined as functions of the α and β which are set at a constant. The model uses a system of equations that calculates the root impedance of the fractal tree.

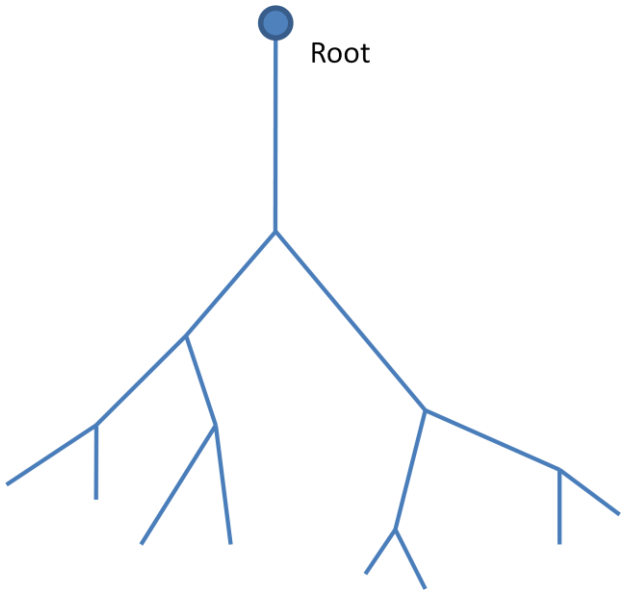

Figure 26: Schematic picture of Olufsen's arterial tree. The radii of the tree are reduced travelling downstream from the root. No small terminal arteries can be found at the first levels of the tree. All terminal arteries are found at the lowest levels of the tree.

Due to the nature of Olufsen's arterial model no small arterioles are found at the first branching levels of the tree. Indeed, the terminal arterioles are only found at the lowest branching levels.

10.3.2 One-dimensional models

Dokoumetzidis et al [41] developed a vascular tree model based on the scaling laws of fractal structure. The model describes the disposition of a substance inside a tree-like fractal network by using solute kinetics in the fluid in the system. The vessels in the network are assumed to be non-elastic tubes where each level consists of parallel vessels. The total flow across a section of the entire network is assumed to be constant which allows for replacement of the tree with a single one-dimensional tube, Figure 27.

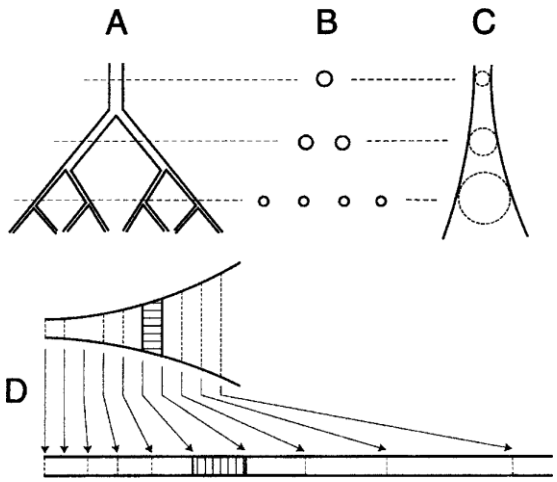

Figure 27: (A) Schematic representation of a dichotomous branching network. (B) Cross section at each level. (C) Tree is replaced by a single tube with continuously increasing radius. The area of the cross section of the tube is equal to the total area of the cross section of each level of the tree. (D) volume preserving transformation of the varying radius[41].

The tree is not area preserving, Figure 27 (C), the total cross sectional area at subsequent levels increases and therefore the tube formed from the fractal tree will not be cylindrical, Figure 27 (A-C). The fluid velocity is kept constant through the branching by calculating a suitable length, Figure 27 (D). This model simplifies the general structure of a vascular tree into a single one-dimensional tube, which is useful in modelling substance dispersion in the circulatory system.

10.3.3 Two-dimensional models

The computational method of constrained constructive optimisation (CCO) developed by Schreiner et al is derived from the principle of optimal design [25, 28]. The first model produced a binary tree which is grown in a computer model by adding terminal vessels to the optimal site of an existing tree. The

first segment is added at the border of a defined area and grown by adding new terminal segments that connect randomly to chosen points within a specified area. At each step of growth the geometry of the newly created bifurcation is optimized under a prescribed set of physiological boundary conditions [25, 28]. Figure 28 shows the result of the CCO method producing a binary tree of 4000 terminals.

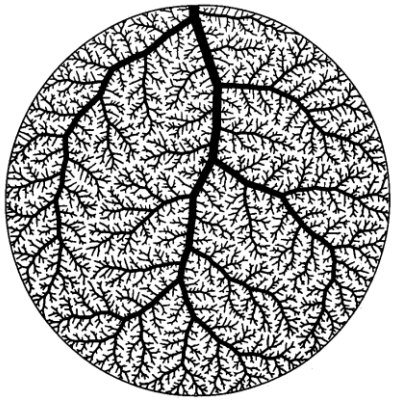

Figure 28: Schreiner and Buxbaum arterial binary tree of 4000 terminal ends.[25]

This model produced a binary tree which visually strongly resembles an arterial tree. A smaller tree, with 250 terminal segments also produced by the CCO method, shows a good correlation with the radii from experimental results from corrosion casts of two human left coronary arteries, Figure 29

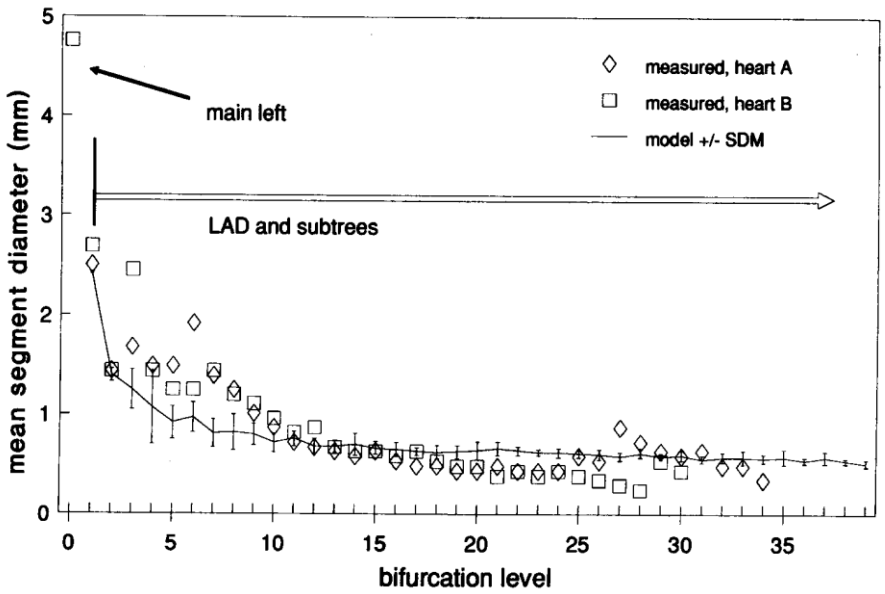

Figure 29: Morphometric comparison between model of 250 terminals and the left coronary artery trees of two humans [25].

Close agreement with the measurements was found for the model diameters for level two and for levels higher than ten. The discrepancies between levels three and ten where concluded to be due to possible inappropriate optimization so close to the tree root. [25].

This model is the basis of the model developed in this thesis and is described in detail in the method chapter.

10.3.4 Three-dimensional models

Three-dimensional models provide a more realistic definition of the arterial network. They are, however, computationally expensive. A three dimensional model was developed by Karch et al [31] using the computational method of constrained constructive optimization (CCO). The model grows a binary tree in a computer model that grows in a sphere where the arterial tree is represented as a binary branching network. The arterial network is presented

as a dichotomous branching structure of rigid cylindrical tubes. The tree is extended by adding a terminal vessel to the existing tree, each time choosing a connecting place that results in a minimum total volume of the tree. The tree is then rescaled each time adjusting the tree's root parameters. No direct information from topographic anatomy is used in the model, but the resulting arterial tree closely resembles corrosion casts of real arterial trees.

10.4 Morphometric characteristics of optimized arterial tress

The relationship between the shape of an organ and the cost of blood transport to perfuse its tissue was the topic of research conducted by Karch et al [42]. The evaluation was based on the optimized arterial model tree simulated to perfuse a square-based volume of $100\ cm^3$. The volumes were all of different rectangular shapes, differing in thickness of the volume, see Figure 30. The effects of the volume shape on the tree structure were investigated as well as the effect on blood transport and hemodynamic characteristics. The arterial trees were generated using the CCO method based on an identical set of model parameters.

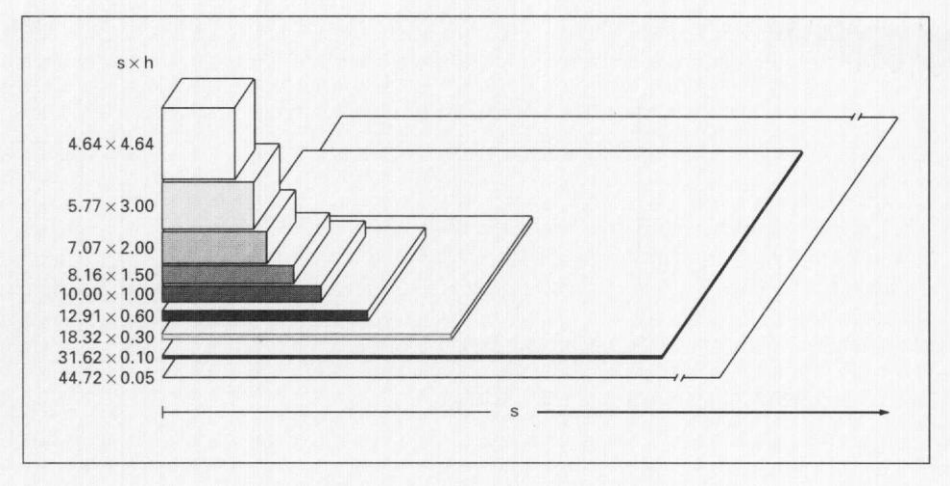

Figure 30: Three-dimensional perfusion volumes of different shape at constant volume $V_{perf} = 100cm^3$, h and s denote the height and side length of each square slab and the numbers for $s * h$ are given in centimetres , excluding the flattest volume $s = 44.72\ cm$ all slabs are drawn to scale [42].

In order to compare the functional differences of arterial tree perfusion in different thicknesses of volume they defined a series of nine square slabs of different height h with a constant perfusion volume $V_{perf} = 100cm^3$. The side length s was chosen so that $s^2 * h = V_{perf}$ ($44.72\ cm \geq s \geq 4.64$, Figure 30Figure 30. For comparison between two-dimensional and three-dimensional CCO structures Karch et al additionally defined two flat perfusion volumes.

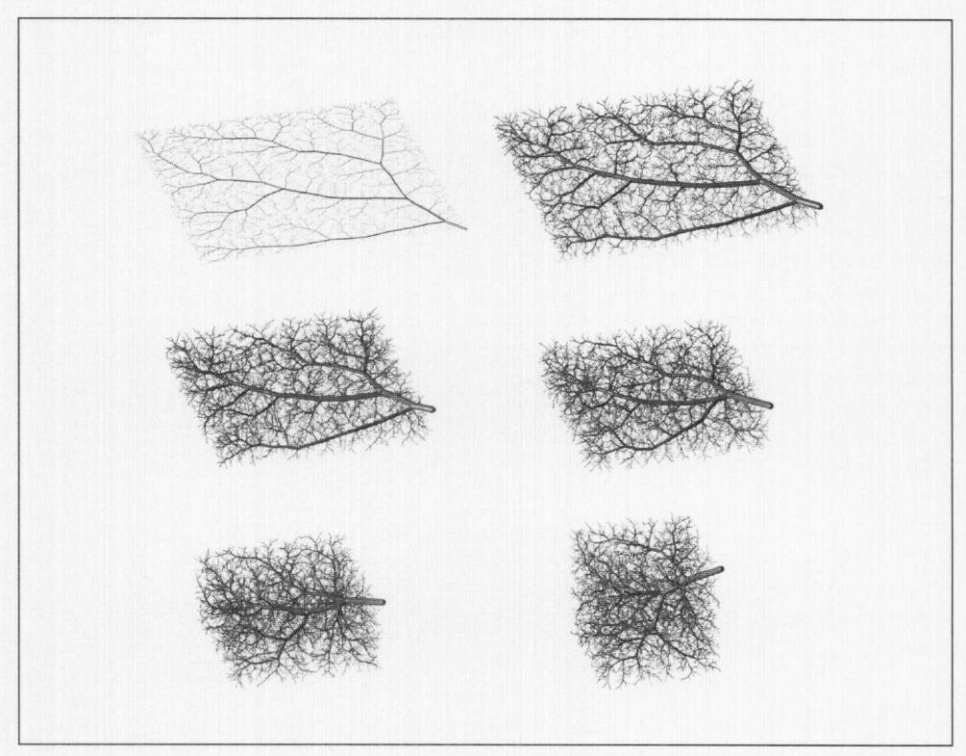

Figure 31: Arterial trees generated by CCO to perfuse volumes of different shapes. Side length = 44.72, 10.00, 8.16, 7.07, 5.77, 4.64 and height h= 0, 1, 1.5, 2, 3 and 4.64 (from the top left to bottom right). Except for the two-dimensional tree where $s = 44.72\ cm$, the perfusion volume is constant at $V_{perf} = 100cm^3$. Figures are drawn to scale [42].

Karch et al found that a decrease in thickness (h) and a concomitant increase of side-length increased the mean transport length. By stretching the side-length and flattening the perfusion volume, there was a seven-fold increase in the mean transport length and a twelve-fold increase of deposition time. This resulted in an approximately nine-fold overall increase in intravascular volume. Statistical descriptions of different CCO trees are presented in Table 2.

Table 2: Statistical description of different CCO trees perfusing square slabs of side-length s and height h [42].

CCO tree $s \times h$ cm × cm	Segment radius r mm	Segment length l mm	Nearest neighbor distance d_n, mm	Area-expansion ratio A_{exp}	Segment orientation φ deg	Bifurcation symmetry ξ_{rad}	Deposition time T_d s	Bifurcation level Λ_{bif}
44.72 × 0.00	0.13 (0.09–0.21)	1.89 (0.11–3.18)	2.35 (1.54–3.31)	1.18 (1.10–1.23)	69.6 (33.2–113.7)	0.56 (0.36–0.74)	1.16 (0.76–1.61)	103 (73–129)
44.72 × 0.05	0.13 (0.08–0.21)	1.88 (1.06–3.18)	2.35 (1.54–3.30)	1.18 (1.10–1.23)	68.3 (33.7–111.6)	0.57 (0.36–0.74)	1.15 (0.76–1.60)	102 (72–125)
31.62 × 0.10	0.12 (0.09–0.19)	1.35 (0.76–2.25)	1.69 (1.14–2.35)	1.18 (1.10–1.24)	69.5 (34.9–112.1)	0.58 (0.37–0.76)	0.68 (0.45–0.96)	91 (64–115)
18.26 × 0.30	0.10 (0.08–0.16)	0.97 (0.60–1.49)	1.36 (1.00–1.75)	1.20 (1.11–1.25)	72.2 (42.6–107.8)	0.63 (0.40–0.81)	0.31 (0.21–0.43)	68 (47–85)
12.91 × 0.60	0.10 (0.08–0.14)	0.89 (0.55–1.40)	1.30 (0.95–1.65)	1.22 (1.15–1.25)	75.8 (49.2–105.4)	0.68 (0.48–0.84)	0.19 (0.13–0.26)	54 (38–68)
10.00 × 1.00	0.09 (0.07–0.13)	0.88 (0.53–1.38)	1.30 (0.95–1.65)	1.22 (1.15–1.25)	75.4 (49.6–103.4)	0.68 (0.50–0.83)	0.15 (0.10–0.19)	45 (32–58)
8.16 × 1.50	0.09 (0.07–0.13)	0.88 (0.54–1.37)	1.28 (0.94–1.63)	1.22 (1.16–1.25)	74.7 (49.2–101.4)	0.68 (0.50–0.84)	0.12 (0.09–0.16)	41 (29–51)
7.07 × 2.00	0.09 (0.07–0.13)	0.88 (0.52–1.37)	1.28 (0.97–1.62)	1.22 (1.15–1.25)	75.5 (49.5–104.5)	0.68 (0.49–0.83)	0.11 (0.08–0.15)	32 (23–41)
5.77 × 3.00	0.09 (0.07–0.13)	0.87 (0.52–1.37)	1.29 (0.96–1.64)	1.22 (1.15–1.25)	74.6 (48.3–103.6)	0.68 (0.50–0.83)	0.10 (0.08–0.13)	30 (22–36)
4.64 × 4.64	0.09 (0.07–0.13)	0.88 (0.53–1.36)	1.30 (0.96–1.63)	1.22 (1.15–1.25)	72.6 (47.1–101.6)	0.68 (0.49–0.83)	0.10 (0.08–0.13)	28 (21–35)
R^2	0.079	0.143	0.178	0.032	0.002	0.032	0.714	0.532

In Table 2 the values are median with first and third quartiles in the brackets. The values for R^2 are taken from analyses of variance of ranked data. Table 2 shows a large variety of characteristics and properties of tree structure. The maximum number of bifurcation levels is highly sensitive to changes in shapes of the perfusion volume. Increasing the side lengths resulted in an eight-fold increase in length of the main vessel in the two dimensional tree from 4.64cm to 68.17 cm. At the same time the number of bifurcation levels increased only three fold. The bifurcation levels per unit length is drastically reduced (from 6.43 to 2.64) when the perfusion volume flattens from cubic to square.

The haemodynamics of the two-dimensional tree model was considered. The blood flow and pressure was calculated and compared with experimental results from the vasculature of a rat mesentery [43],

Figure 32.

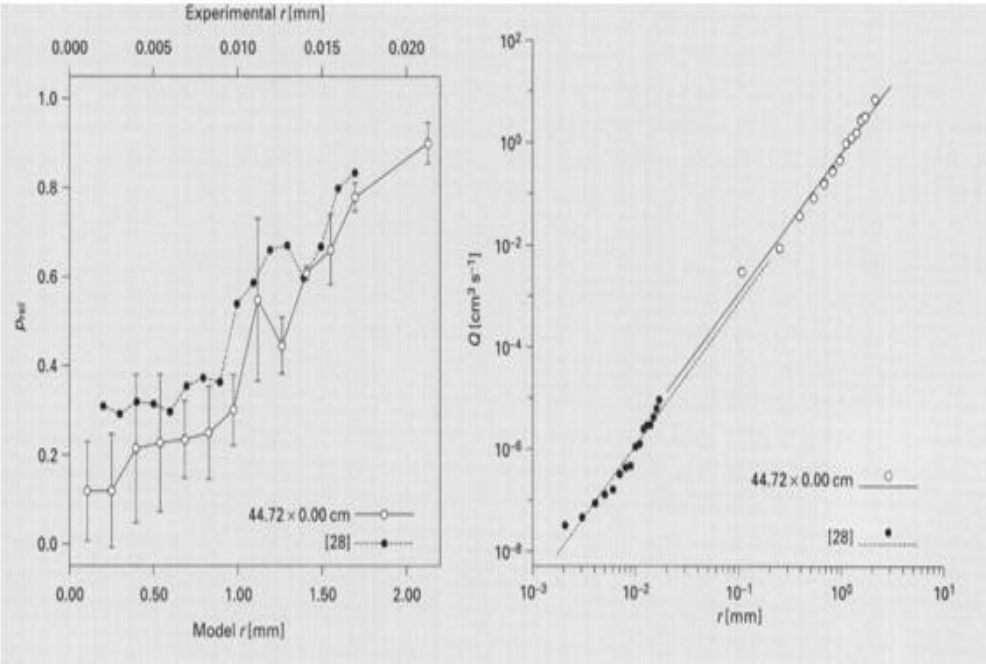

Figure 32: Comparison of the results from two-dimensional CCO model tree with data from experimental measurements in the rat mesentery. Relative mid-segment pressure (p_{rel}) and volumetric flow (Q) as classified by radii (r). Model (O) and experimental (●) are represented as means. The bars present the standard deviation of the model data from p_{rel}). Axes on the bottom and top refer to model and experiment, respectively. Straight lines were fitted to the points of the model (———) and experimental data (- - - -) [42].

From these measurements the missing flow velocities were calculated from diameters by an empirical linear regression pressure, and volumetric flow rates per segment were estimated by means of network flow simulations based on the experimentally determined topology, geometry and haemodynamic boundary condition. For volumetric flow, Q, the power law was used on experimental data as well as the model data. The pressure results from the model shows good agreement with the pressure calculated from the experimentally acquired data. Their results produced almost identical slopes of the radius –flow relationship from the model data and the experimental data, Figure 32.

10.5 Cerebral cortex microcirculation morphometry.

There is not much quantitative data on the brain microcirculation. Lauwers et al [29] scanned a large volume of the human cerebral cortex and digitized more than 300.000 vascular segments, Figure 33. By injecting Indian ink into the brain a three-dimensional projection was produced. The vessels of the scanned arterial tree were split into two groups, arteriolar and capillary. The statistical distribution of the vessels diameter and length were measured and the results plotted, Figure 34. The distribution of the diameter and length proved to be asymmetrical. However by mapping the diameter of the arterioles, using a function which calculates the inverse square value a normal distribution was acquired.

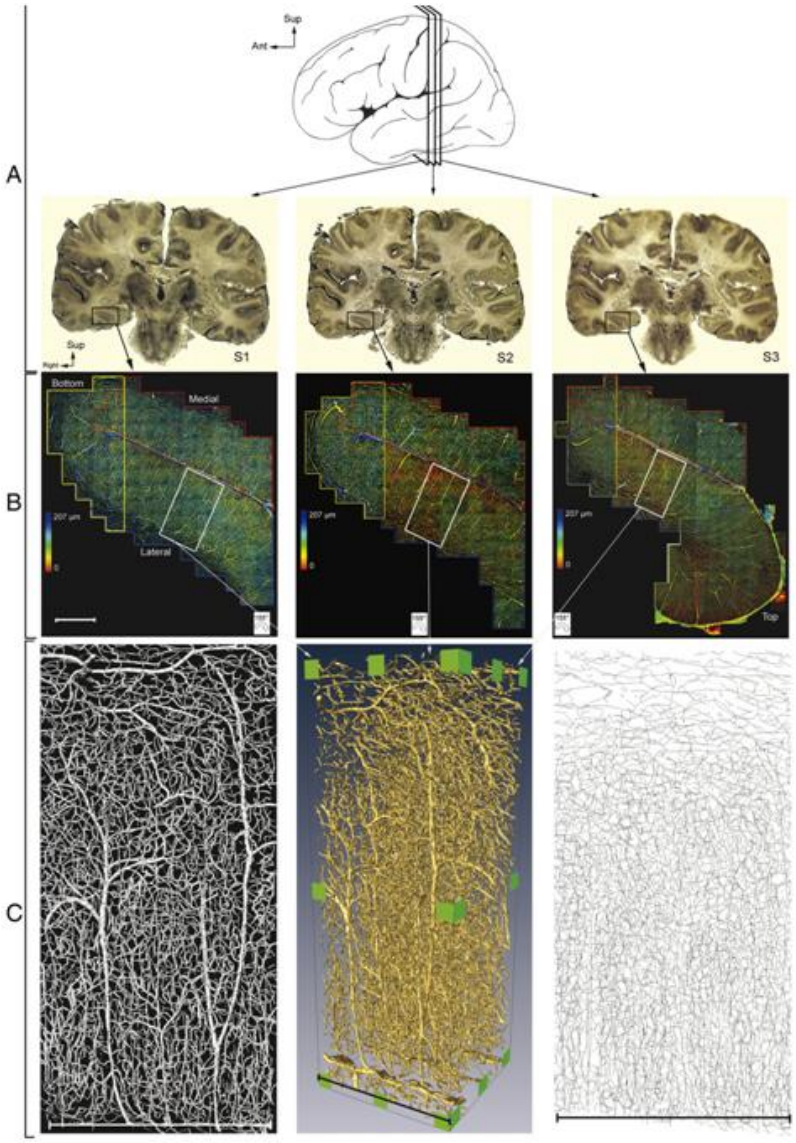

Figure 33: (A) Three Coronal section (S1, S2, S3) of Indian ink injected human brain for data acquisition taken from Lauwers et al published article [29]. The region of interest is located around the collateral sulcus in the right temporal lobe, black rectangular. (B) Depth coded ink-injected human brain for date acquisition taken form Lauwers et al published article [11]. The region projection of the zones is reconstructed by confocal microscopy. The 10 mosaics are outlined; three mosaics are cut out from each section according to the cortical pattern. A fourth mosaic is defined in S3 in the superficial gyral area. (C) Three-dimensional volume rendering of a selected zone, white rectangle, after alignment of the three sections, bottom centre. Vascular skeleton of the same zone as in S1, bottom right. Three dimensional reconstruction of this part of S1 Skeleton, bottom left. Scale bar 1mm [29].

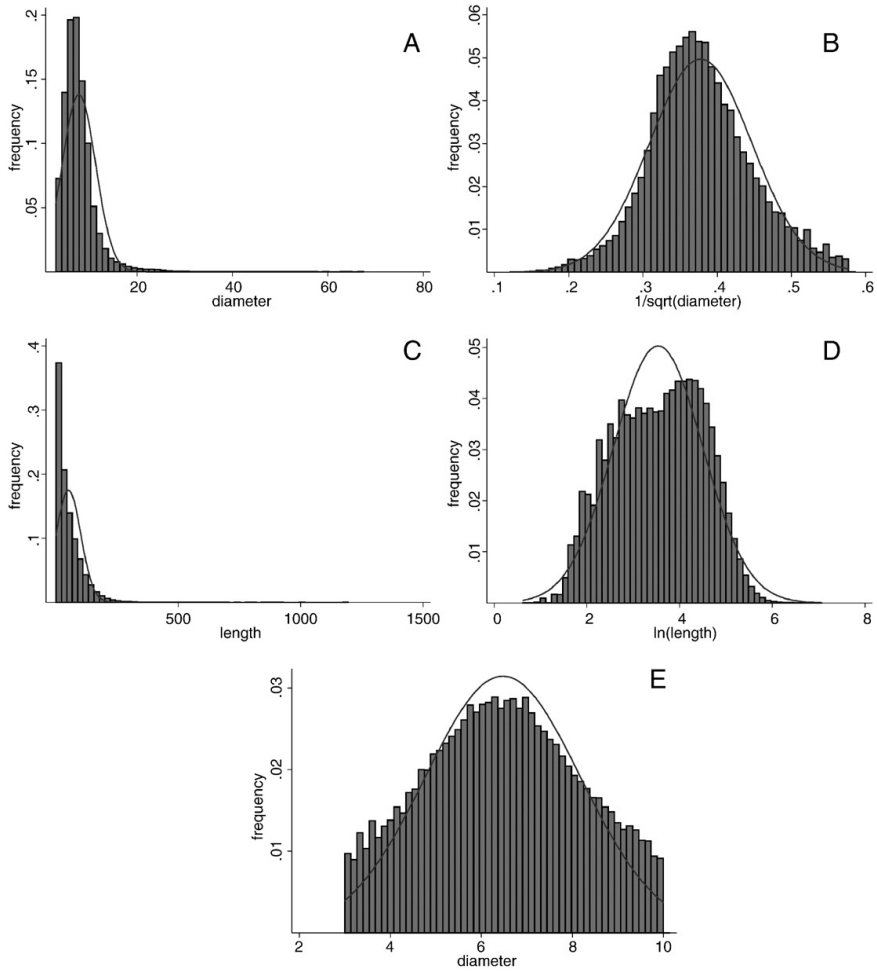

Figure 34: The morphometric results from Lauwers et al research. (A) The distribution of diameter of the arterioles without mapping. (B) The distribution of diameter after mapping. (C) The distribution of length without the mapping (D) length after mapping. (E) The distribution of diameter of the capillaries [29].

Mapping the length by using the natural logarithm also resulted in a normal distribution. The distribution of the capillary diameter was on the other hand naturally normally distributed. Lauwers et al are the first to provide quantitative information on the cerebral cortex.

11 Method

The simulation model (SM) program developed here produces a binary tree structure that resembles an arterial vessel structure. The SM program is based on the constrained constructive optimization (CCO) method developed by Schreiner and Buxbaum [25].Two SM binary trees were grown: a tree of 2000 terminal nodes (T2000) and a tree of 250 terminal nodes (T250). Furthermore the growth of the T2000 tree was observed at 15, 75, 150, 500, 1000 and 2000 terminal node stages. The statistics geometry and physiological properties of the T2000 tree were investigated. The physiological properties were acquired by taking the radii and length of the T2000 tree and running it through a model built by Alzaidi [44] which calculates the pressure and flow rate. All calculations on the SM trees were conducted in Matlab. The results from the T250 tree were used to compare with results form a CCO tree of the same size as well as comparing it with experimental results. The SM program is developed in Visual studio using the C/C++ programming language. In the following section the CCO method and SM method are compared and explained.

11.1 Comparing CCO and SM Methods

The SM method represents the arterial tree as binary branching trees of nonintersecting rigid cylindrical tubes or segments in the same way as the CCO method does. In both models the arterial structure is assumed to be perfused at a steady state and laminar flow conditions subject to boundary conditions. The optimization principle used to determine the bifurcation structure in the CCO method was the minimum volume principle. Schreiner and Buxbaum [28] decision to use the minimum volume is based on the fact that blood requires a significant portion of the body resources. It is therefore

logical to assume that minimum volume is desirable. They also demonstrated the feasibility of the developed method and for an isolated location it was shown that by minimizing the volume, an optimal geometric structure is acquired. The SM method also uses the minimum volume function. This enables comparison between binary tree structures produced by SM and CCO. The algorithm for the SM method like the CCO method is based on the assumption that the volume to be perfused is a circle and the tree is represented as a binary branching network of rigid cylindrical tubes or segments. The tree starts at the root segment and is truncated in the form of a terminal segment or leaves whose number is chosen before the run of the program. The leaves are considered to provide a microcircular box with blood flow. The model should deliver a tree that fills the space of the perfusion volume as evenly as possible without intersection of segments. The tree grows within a constrained area both in the SM and CCO method but the constrained areas are handled in different ways between the models. In the CCO, prior to a new branch, the supporting area (A_{supp}) in which the tree is grown is enlarged so that all the coordinates of the existing tree need to be scaled accordingly. This is not the case for the SM method where the A_{supp} is replaced by A_{unit} which has the constant value of 1.0, as explained in section 11.1.6. The CCO and SM binary trees are grown by random selection of coordinates in a restricted area A_{supp} and A_{unit} respectively. If the coordinates meet a criteria of minimum distance from all the existing segments the point is connected to the existing tree structure using pointers of the nodes. Often the chosen coordinates will result in a number of possible connections to the existing tree. All the possible connections form new bifurcations which are optimized one by one using the target function minimum total volume. When all the possible connections have been optimized, the new branch that yielded the lowest total

volume for the tree is chosen as a suitable addition to the existing tree. Figure 35 shows the flow diagram of the SM program.

11.1.1 Global Model Parameters and Physiological Values

The global parameters used in the SM program are based on the CCO parameters given by Schreiner and Buxbaum [25] to enable comparison between the two methods, see Table 3.

Table 3: Global parameters of the SM model

Parameter	Meaning	Value
A_{perf}	Perfusion area	$0.00785\ m^2$
P_{perf}	Perfusion pressure	$1.33 * 10^4\ Pa$
P_{term}	Terminal pressure	$8.38 * 10^3\ Pa$
Q_{perf}	Perfusion flow	$8.33 * 10^{-6} m^3/s$
Q_{term}	Terminal flow	$4.165 * 10^{-9} m^3/s$
N_{term}	Number of terminals	2000/250
η	Viscosity of blood	$3.6 * 10^{-3}\ Pa\ s$
γ	Bifurcation exponent	3.00

The detail of blood rheology is not considered in the CCO or the SM method. Instead the blood is modeled as an incompressible homogeneous Newtonian fluid at a steady-state and laminar flow conditions. The viscosity η has a constant value of $3.6 * 10^{-3}$ Pa s . The perfusion pressure P_{perf} was set to 100 mmHg, the terminal pressure P_{term} at 60 mmHg and the total perfusion flow Q_{perf} at 500 ml/min.

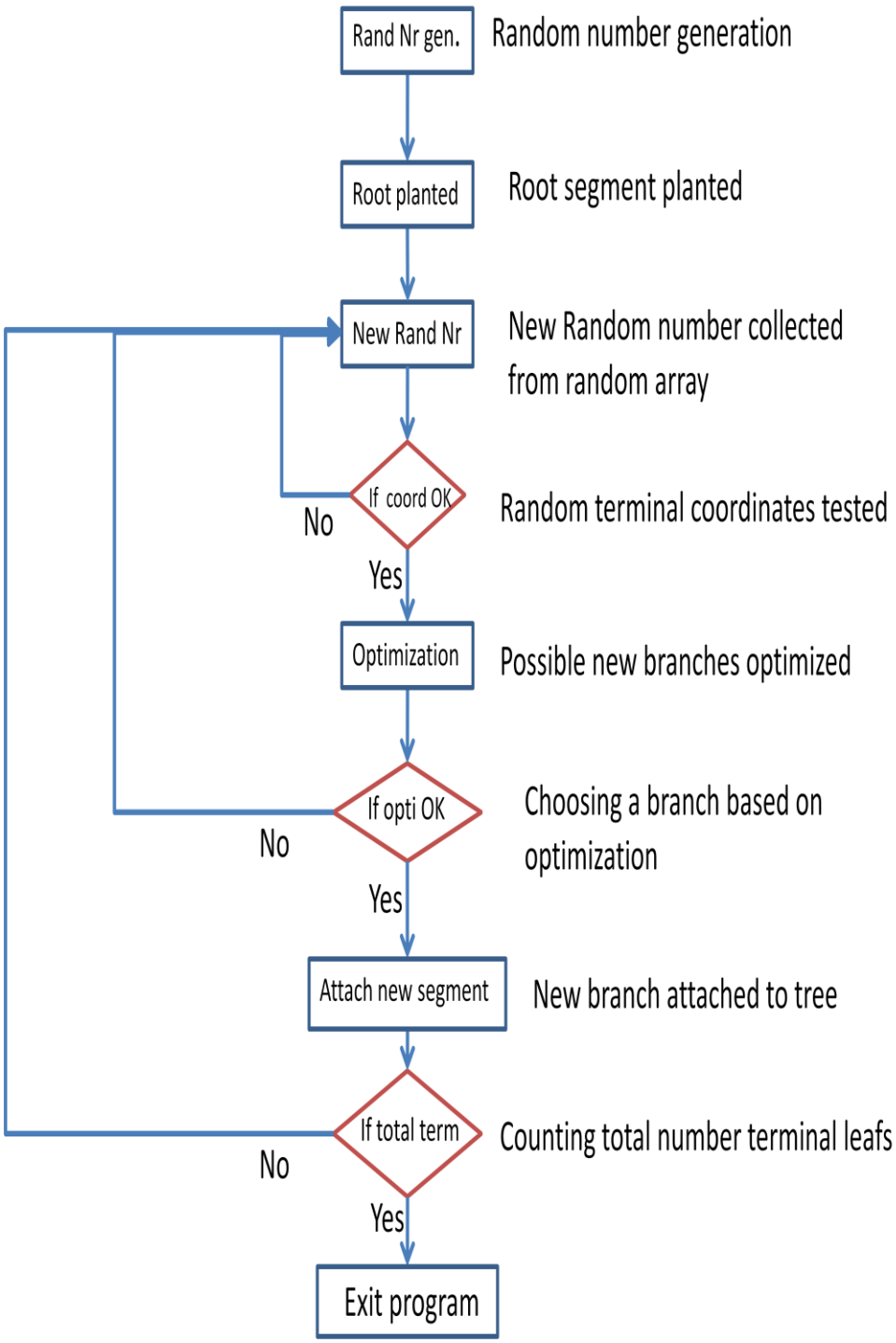

Figure 35: Flow diagram explaining the SM program structure.

11.1.2 Data Structure

The arterial tree is built up on nodes which are connected to each other by pointers, Figure 36. In the program a node is an object derived from the class BiNode. The object has properties which are outlined in Table 4.

Table 4: Properties of the Class BiNode

BiNode properties	Explanation of properties
itail_L	BiNode pointer, points to the left daughter node
itail_R	BiNode pointer, points to the right daughter node
iPrevious	BiNode pointer, points to the parent node
Id_number	Unique identification number for each node in the tree
x	The x coordinates of a node
y	The y coordinates of a node
radius	The radii of a segment
length	The length of a segment
distal_resistance	The resistance of the peripheral subtree with respect to current node
distal_leaf_count	The distal leaf count with respect to current node
branch_volume	The volume of the current branch
sub_tree_volume	The volume of the subtree with respect to current node
path	A Boolean variable which is set to true if a node belongs to a path which leads down to a connection point of a new branch

The nodes are connected by the three pointers; itail_L, itail_R and iPrevious found in each node. The tail pointers (itail_L, itail_R) point to the daughter nodes of a parent node while the iPrevious pointer points to the parent node, Figure 36 . The term left and right in relations to the SM binary tree refers to moving downstream from the root towards the terminal ends. The pointers provide a connection through the data structure, enabling traverses up and down the tree. Except for the root node, every node has a previous node to which its IPrevious pointer points to. Similarly, all nodes except for the terminal nodes have daughter nodes to which the Itail pointers point to. The purpose of the tree is to structurally represent a sample of the arterial system. This is done by defining a segment vessel as the distance between a parent

node and a daughter node, Figure 36. Properties of each segment vessel e.g. its length and radius are stored in the node that is further from the root node.

The SM model developed here has added properties in its tree nodes compared with the model developed by Schreiner & Buxbaum. The added properties are length, distal_resistance, distal_leaf_count, branch_volume, sub_tree_volume and path. All these properties could be calculated by traversing up and down the tree each time if needed, but storing these values in each node is simpler.

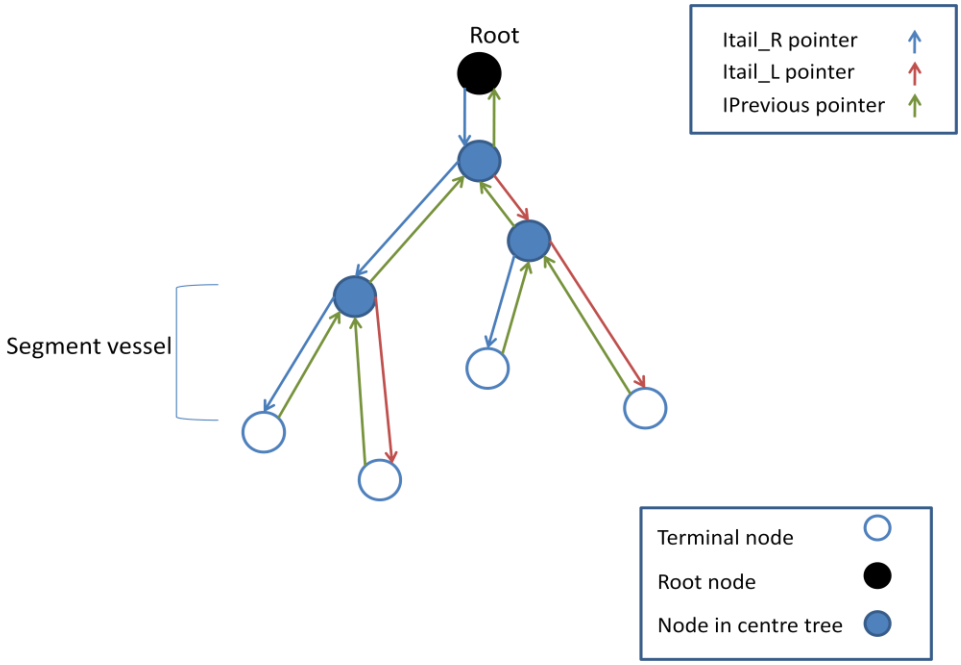

Figure 36: Schematic figure showing pointers connecting nodes forming a small binary tree.

Once the program has produced a binary tree of the desirable size, the data stored in all the nodes is transferred to two ASCII files, AllNodes and ALLNodeLevel. The ASCII file named AllNodes holds the id number, coordinates, radii and length associated with each node, while the other ASCII

file named ALLNodeLevel holds all the other information found in the nodes. Table 5 shows the structure of an AllNode ASCII file.

Table 5: An example of the ASCII files produced by the SM model.

Row	Id Node-A	X Node-A	Y Node-A	radii Node-A	length Node-A	Next node
1	*0	3.16e-007	1	0	0	|
2	37	0.00023	0.999	0.00172	0.00049	|

Table 5 cont.

Row	Id Node-B	X Node-B	Y Node-B	radii Node-B	length Node-B	End of line /seg.
1	37	0.00023	0.999	0.00172	0.00049	#
2	58	0.0926	0.988	0.12980	0.09301	#

*The inlet root node has the id number zero.

The two ASCII files are structured in the same way so that each row represents a segment in the tree structure. Reading the ASCII file from left to right to the "|"sign, provides the information found in node A. The "|"sign indicates an end of information in A node and the start of information in B node. The information from the "|" sign to "#" sign are all stored in node B.

In the ASCII file node A is always the proximal node or the node closer to the root whereas node B is the distal node. Figure 37 shows a schematic figure explaining the structure of the ASCII files in relation to the binary tree structure by looking at row one and two from Table 5.

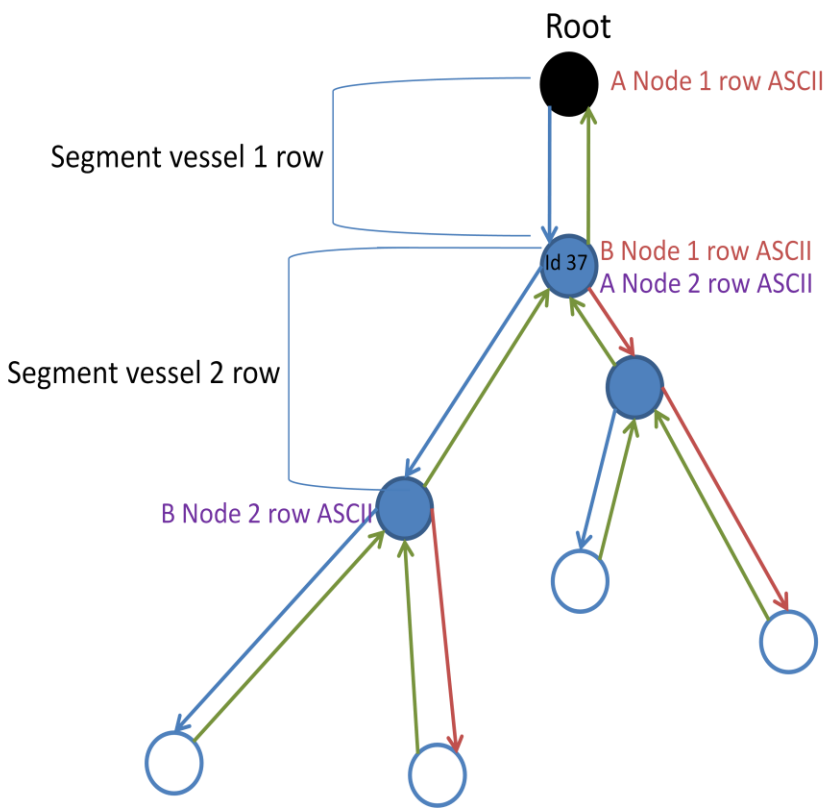

Figure 37: Schematic figure explaining the structure of ASCII files in relation to the binary tree structure.

From Figure 37 we see that the same node id 37 can be presented as node B in row one in the ASCII file and then in row two in the ASCII file as node A. Both ASCII files have the same structure where each row represents a segment of the tree. An example of both the ASCII files can be found in Appendix A.

11.1.3 Boundary Conditions

The generation of the arterial model tree with the CCO method is based on the assumptions that the area to be perfused is two-dimensional and that the tree segments are rigid cylindrical tubes perfused at a steady state under laminar

flow conditions. This is also the basis of the SM method. The SM and CCO method both assume blood to be an incompressible homogeneous Newtonian fluid and that the hydrodynamic resistance R_i of each segment is given by Poiseulle‘s law:

$$R_j = \left(\frac{8\eta}{\pi}\right)\frac{l_i}{r_i^4}, \quad (11.1)$$

where l_i and r_i denotes the length and internal radius of segment i and η is the constant viscosity of blood. Given R_i the pressure drop Δp_i of the model tree along the segment i is determined by the flow Q_i through the segment i as:

$$\Delta p_i = R_i Q_i. \quad (11.2)$$

The total hydrodynamic resistance R for both the CCO and the SM tree is calculated by decomposing the tree into subtrees and then from the bottom up to the root. This is done by using the repetitive relations of both the parallel and serial resistance of the segments in the SM tree using the following equations respectively:

$$R_{parallel} = \frac{R_{left}\, R_{right}}{R_{left} + R_{right}}, \quad (11.3)$$

$$R_{series} = R_{periferal} + R_{distal}. \quad (11.4)$$

The basic physiological boundary conditions and constraints are that the pressure p_{term} at the distal ends of terminal segments is equal and assumed to be the inflow pressure into the microcirculatory box:

$$\Delta p = p_{perf} - p_{term}, \quad (11.5)$$

where p_{perf} denotes the perfusion pressure in the root artery. The laminar flow resistance of the whole tree induces a given total perfusion flow Q_{perf} across the overall pressure drop. The net flow Q_{perf} is the same at each step of tree generation. The flow through a segment Q_i is proportional to the number of terminal segments or more accurately the number of distal micro circular boxes:

$$Q_i = \text{NDIST} * Q_{term}, \quad (11.6)$$
$$Q_{term} = \frac{Q_{perf}}{N_{term}}, \quad (11.7)$$

where NDIST is the number of distal microcircular boxes and N_{term} is the total number of terminal segments.

Each terminal segment i delivers an amount of blood flow $Q_{term,i}$ into the microcirculation against the constant terminal pressure p_{term} and Q_{perf} is the same at each step of the tree generation.

The terminal segments N_{total} are arranged such that their distal ends are evenly distributed within the perfusion area. The total number of segments in the binary tree is:

$$N_{total} = 2N_{term} - 1 \quad (11.8).$$

This is true for all binary tree structures.

11.1.4 Bifurcation Conditions

The terminal ends of the tree are arranged in such way that they are evenly distributed through the perfused volume. To ensure realistic bifurcation

conditions the radii of the parent segment and its daughters obey the following bifurcation law:

$$r_{parent}^{\gamma} = r_{left}^{\gamma} + r_{right}^{\gamma}, \quad (11.9)$$

with a constant exponent $\gamma = 3$ (bifurcation exponent) base on Murray's law [33]. The relation determines the shrinkage of the segment radii across bifurcations, or the amount of expansion in the cross sectional areas of parent and daughter segments. If a segment bifurcates, the radii of the segment are stored as a ratio of its parent segment:

$$\beta^{l}(i) = \frac{r\left(D_i^{l}\right)}{r(i)} \quad (11.10)$$

$$\beta^{r}(i) = \frac{r(D_i^{r})}{r(i)} \quad (11.11)$$

where β^{l} is the left daughter radius ratio, β^{r} is the right daughter radius ratio, $r\left(D_i^{l}\right)$ is the left daughter radius, $r(D_i^{r})$ is the right daughter radius and $r(i)$ is the parent radius.

The only segment storing real radius is the root segment and all the other radii in the tree are therefore a ratio of the root segment radius.

11.1.5 Random Coordinates

The binary tree growth depends on a random number generator to produce the coordinates for the terminal end of a new branch. The random number generator used by the SM program is Mersenne Twister, a pseudorandom number generating algorithm developed by Makoto Matsumoto and Takuji Nishimura in 1996 and 1997[45]. The random number used by Schreiner and Buxbaum was from NAG library. The generator designed by Makoto Matsumoto and Takuji Nishimura has the period of $2^{19937} - 1$ of uniform distributed random numbers. Before starting the actual making of the binary

tree, the random generator code is executed, storing the numbers in an array. The numbers from the array are then used to produce the terminal coordinates for the new branches in the tree. All the random numbers generated are a ratio of the biggest number generated so they are all smaller or equal to 1.0. The x,y coordinates are derived from polar coordinates produced using the random numbers to calculate random radius r_{rand} and degree $degree_{rand}$ of the unit circle with the radius $r_{unit} = 1.0$. The r_{rand} is simply given the value of the random number unchanged from the random array. The $degree_{rand}$ are the product of a second random number from the random array multiplied by 360. The radii and degrees are then converted to Cartesian coordinates ($x_{newTerm}$, $y_{newTerm}$) which now represent a possible terminal end of a new segment in the tree.

The evaluation of the possible new random coordinates are conducted in the same way in both the CCO and SM method The distance from the ($x_{newTerm}$, $y_{newTerm}$) coordinates to all other segments in the existing tree structure is calculated in the following way. If $x_{A,i}$, $y_{A,i}$ are the coordinates of node A and $x_{B,i}$, $y_{B,i}$ of B node of segment i in an existing tree and the $x_{newTerm}$, $y_{newTerm}$ are the generated random coordinates then the first projection of the new terminal coordinates on to the segment i is calculated by:

$$d_{proj\ (x,y,i)} = \begin{pmatrix} x_{A,i} - x_{B,i} \\ y_{A,i} - y_{B,i} \end{pmatrix} \cdot \begin{pmatrix} x_{newTerm} - x_{B,i} \\ y_{newTerm} - y_{B,i} \end{pmatrix} l_i^{-2} \qquad (11.12)$$

Here the "·" denotes a scalar product. If $0 \leq d_{proj} \leq 1$ the projection lies within segment i. In this case the orthogonal distance is calculated:

$$d_{crit} = d_{ortho(x,y,i)} = \left| \begin{pmatrix} x_{A,i} - x_{B,i} \\ y_{A,i} - y_{B,i} \end{pmatrix} \cdot \begin{pmatrix} x_{newTerm} - x_{B,i} \\ y_{newTerm} - y_{B,i} \end{pmatrix} \right| l_i^{-1} \qquad (11.13)$$

For other values of d_{proj} the distance between $x_{newTerm}$, $y_{newTerm}$ and the segments i end points may still be critical and is calculated as follows:

$$d_{crit} = d_{end}(x, y, i)$$
$$= Min\left\{\begin{matrix}\left(\left(x_{newTerm} - x_{B,i}\right)^2 + \left(y_{newTerm} - y_{B,i}\right)^2\right)^{\frac{1}{2}}, \\ \left(\left(x_{newTerm} - x_{A,i}\right)^2 + \left(y_{newTerm} - y_{A,i}\right)^2\right)^{\frac{1}{2}}\end{matrix}\right\} \quad (11.14)$$

Once the value of d_{crit} has been calculated it is compared to a threshold value (d_{thresh}) which is defined by:

$$d_{thresh} = \left(\pi * r_{supp}^2 / k_{term}\right)^{1/2} \quad (11.15)$$

where k_{term} is the current number of terminal segments, r_{supp} or r_{unit} is the radius of the circle in with the tree is gowing in. If d_{crit} exceeds the threshold distance d_{thresh} then the coordinates are accepted to become the location of a new terminal segment. If however the coordinates ($x_{newTerm}$, $y_{newTerm}$) do not fulfill the above requirements a new pair of random numbers is chosen. When a new random number is chosen based on a failed attempt a counter (N_toss_count) is incremented. If failed attempts happen eight times in a row or N_toss times, then d_{thresh} is multiplied by 0.9 and a new pair of random numbers are drawn from the array.

11.1.6 Supporting Area

The CCO algorithm defines a perfusion area (A_{perf}) and divides it into smaller supporting areas (A_{supp}) as follows:

$$\pi r_{supp}{}^2 = A_{perf} / N_{term} \quad (11.16).$$

At the start of the run of the program, radius r_{supp} will equal the radius of one micro circular area and then grow with every new terminal branch so that each new branch has a micro circular box to infiltrate. The first branch is planted in the A_{supp} so that the root node is at the edge of the circle and the second node is planted randomly in the circle. The two nodes are now connected by pointers and radius of the new branch is calculated and stored in the distal node. Now a tree of one branch has been created which is scaled and has total resistance and the flow through the branch is adequate for the number of terminal branches of the tree. Before adding a new branch to the existing tree the supporting area A_{supp} is increased.The increas is formulated in the following way:

$$r_{supp} = \sqrt{\frac{(k_{total} + 1) * (A_{perf} / N_{total})}{\pi}} \qquad (11.17)$$

where k_{total} is the total number of branches in the developing tree before adding a new branch, N_{total} is the total number of segments of the tree, A_{perf} is the perfusion area and r_{supp} is the radius of the support circle. The increase in the supporting area calls for stretching of all coordinates in the tree. This results in an increase in length of all segments, which in turns calls for an increase in radii and therefore a rescaling of the whole tree. When the supporting area has been increased and the values of the tree rescaled the planting of a new branch can begin.

The use of support area was replaced by unit area (A_{unit}) in the SM program. The supporting area was assumed to be of the constant size with the radius (r_{unit}) of the constant value 1.0. All the coordinates of the tree branches are therefore based on the unit circle. The rescaling of the trees coordinates

happens once the tree is fully grown. However the length of each segment can easily be calculated because only the length is directly dependant on the circle in which the tree is growing in.

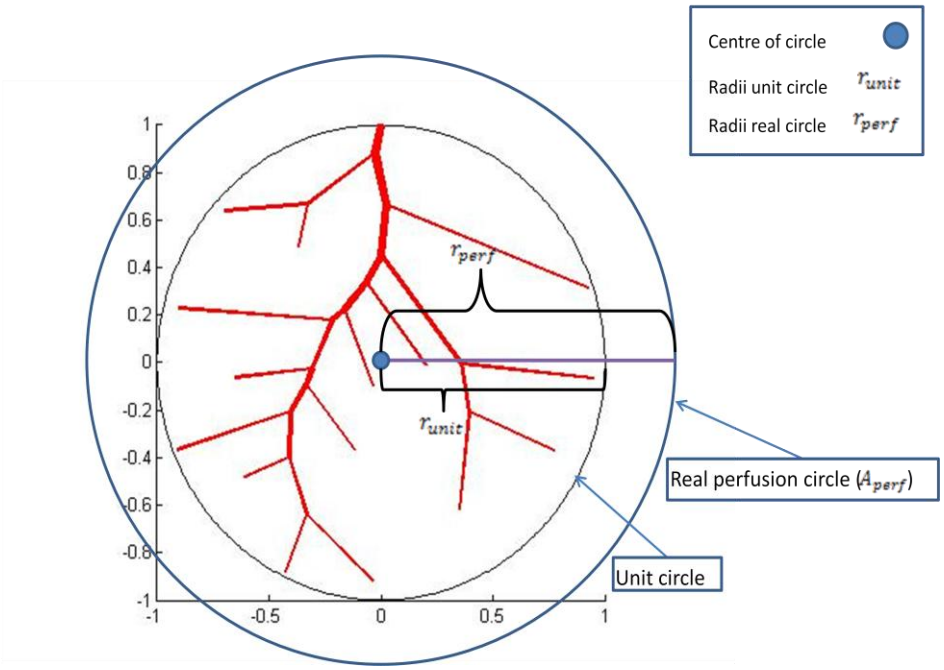

Figure 38: Schematic figure showing the relationship between unit circle A_{unit} and perfusion circleA_{perf}.

According to the CCO method the A_{perf} is divided by the number of terminal segments and then through the run of the CCO program the A_{supp} is incresed one segment at a time back to the size of A_{perf} , scaling the length of the tree each time. Now by replacing A_{supp} by a unit circle A_{unit} we get a circle with the radius of r_{unit} . The relation ship between the unit circle and the A_{perf} is defined in the following way:

$$a * r_{unit} = r_{perf} \quad (11.18)$$

Now the CCO method increases its supporting area until it equal the A_{perf}. However the SM method scales the segments length by a. If x,y and v,w are the coordinates of two nodes connected by pointers forming a segment the segments length would be calculated in the following way:

$$Segment's\ length = a\sqrt{(v-x)^2 + (w-y)^2} \quad (11.19)$$

$$a * r_{unit} = r_{perf} \quad (11.20)$$

$$r_{perf} = \sqrt{\frac{A_{perf}}{\pi}} \quad (11.21)$$

The scaling does not affect the target optimization function because the minimum of f(x,y) and f (ax,ay) is the same. Therefore the supporting circle introduced by Schreiner and Buxbaum is not necessary in the SM algorithm.

11.1.7 Adding a Terminal Segment

First a random number is tossed for and chosen as previously described. Once the coordinates have been accepted the new random point is connected to the possible segments in the existing tree structure one by one and each time the bifurcation formed is optimized and the total volume of the tree structure is stored along with the coordinate of the *ibif* node position, see Figure 39(D).

Once the connection to a possible segment is done a new bifurcation (*ibif*), has been formed as in Figure 39(D). This new bifurcation disturbed of the distribution of the segmental flows distal to the new bifurcation or inside the

rectangular Figure 39(D). This addition has resulted in the violation of the boundary conditions with regard to the terminal flows definition Q_{term} . In order to establish a correct terminal flow the hydrodynamic resistance of the tree has to be adjusted accordingly. Since the terminal pressure is assumed uniform the flow splitting ratio at the bifurcation segment $ibif$ is given in the following way:

$$\frac{Q_{icon}}{Q_{inew}} = \frac{R_{inew}}{R_{sub,icon}} = \frac{R^*_{inew}/r^4_{inew}}{R^*_{sub,icon}/r^4_{icon}} \quad (11.22)$$

where $R_{sub,icon}$ is the hydrodynamic resistance of segment $icon$ including its left and right subtrees and R_{inew} is the resistance of the new terminal segment $inew$. $R^*_{sub,icon} = R^*_{sub,icon}/r^4_{icon}$ and $R_{inew} = R^*_{inew}/r^4_{inew}$ are the corresponding reduced hydrodynamic resistances. It is assumed that that $R^*_{sub,icon}$ is independent of r_{icon} or to be more exact the radii ratio of *icon* or the β_i. The radii ratio of the segments below *icon* in the tree remains unaffected by the new added segment. The new segments resistance R_{inew} is calcaulated in the following way

$$R_{inew} = \frac{8\eta l_{inew}}{\pi} \quad (11.23)$$

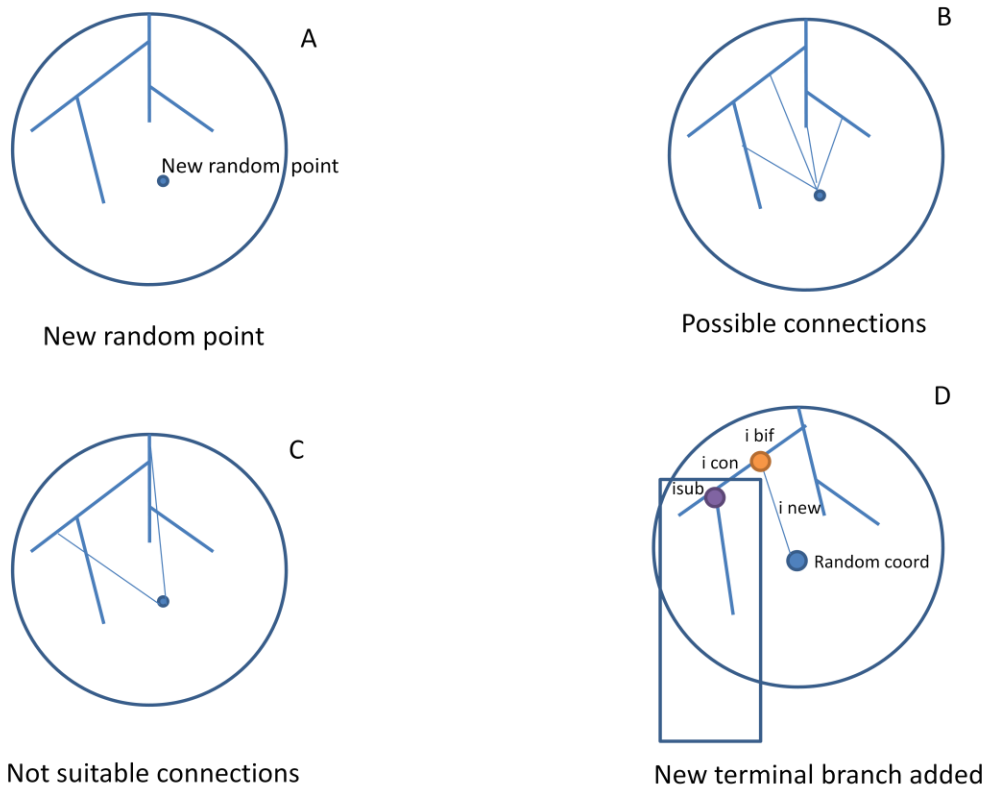

Figure 39: Schematic figures explaining the addition of a new terminal segment to the SM tree. (A) The new random coordinate in the unit circle. (B) The possible connections of the random coordinates to the existing tree structure. (C) Demonstrates the connections that are not suitable as possible connection points because of crossing the existing segments of the tree. (D) The adding of new terminal segments and the new bifurcation that are formed as a result. The rectangle indicates the subtrees of the ibif node. Ibif is the new bifurcation that is formed by adding the new terminal segment to the existing tree, icon is the peripheral part of the branch that now has been split in two by connecting the new random node, inew is the new segment and isub is the node storing the subtree resistance.

The reduced resistance of $R_{sub,icon}$ of the segment icon is calculated in the CCO by traversing the subtree of icon in postorder mode using equation 11.24.

$$R^*_{sub,i} = \left(\frac{8\eta}{\pi}\right) l_i + \left[\frac{\left(r_{left,i}/r_i\right)^4}{R^*_{left,i}} + \frac{\left(r_{right,i}/r_i\right)^4}{R^*_{right,i}}\right]^{-1} \quad (11.24)$$

$R^*_{left,i}$ is the reduced resistance and $r_{left,i}$ id the inlet radius of the left subtree of segment i.

The SM method stores the subtree resistance in each node. This is possible since the resistance of the subtree in the rectangle, Figure 39 (D), is not affected by the addition of the new segment. The resistance of the *ibif* subtree is therefore calculated by collecting the stored resistance of the *isub* subtree and adding the resistance calculated for *icon* segment (in series) finally, adding the new resistance of $inew$ (in parallel) to the resistance of the subtree $isub$.

From equation 11.25 the ratio of the radius of the daughter segments $inew$ and $icon$ is derived

$$\frac{r_{icon}}{r_{inew}} = \left(\frac{Q_{icon} * R^*_{sub,icon}}{Q_{inew} * R^*_{inew}}\right)^{1/4} \quad (11.25)$$

Using the bifurcation rule, equation 11.9, the bifurcation ratio are obtained with respect to segment $ibif$

$$\beta^{icon}_{ibif} = \frac{r_{icon}}{r_{ibif}} = \left[1 + \left(\frac{r_{icon}}{r_{inew}}\right)^{-\gamma}\right]^{-1/\gamma} \quad (11.26)$$

$$\beta^{inew}_{ibif} = \frac{r_{inew}}{r_{ibif}} = \left[1 + \left(\frac{r_{icon}}{r_{inew}}\right)^{-\gamma}\right]^{-1/\gamma} \quad (11.27)$$

Where γ equal 3.0. The last equation guarantees that the flow splits correctly between the subtree distal to $ibif$ and the new terminal segment $inew$.

As a result of the connection of the new terminal branch to the existing tree the radii of all the branch leading up to the root from the connection point need to be recalculated to compensate for the additional terminal branch using the previous equations (11.24, 11.25, 11.26, and 11.27). However once at the root the calculation of the root radius is done by the following equation

$$r_{root} = \left(\frac{R^*_{sub,iroot}}{R_{sub,iroot}}\right)^{1/4} = \left[R^*_{sub,iroot} * \frac{Q_{perf}}{(p_{perf} - p_{term})}\right]^{1/4} \quad (11.28)$$

where $R_{sub,iroot}$ denotes the hydrodynamic resistance of the whole tree including the root segment. The new random coordinate is connected to all the possible connection sites and the bifurcations that are formed are geometrically optimized, one by one as described. In the SM method following the optimization of each temporal bifurcation the coordinate of the connection point is stored as well as the total volume of the tree. Then the tree is restored to its previous structure by disconnecting the new branch and recalculating the values stored in the segments previously changed due to the adding of the new segment. Then the next possible temporal connection can be optimized in turn.

11.1.8 Spatial optimization of new bifurcation

Growing of the SM tree is conducted by successively adding a new terminal segment to the existing tree structure. The new randomly chosen coordinate is connected arbitrarily halfway within a chosen existing segment in the tree, Figure 40.

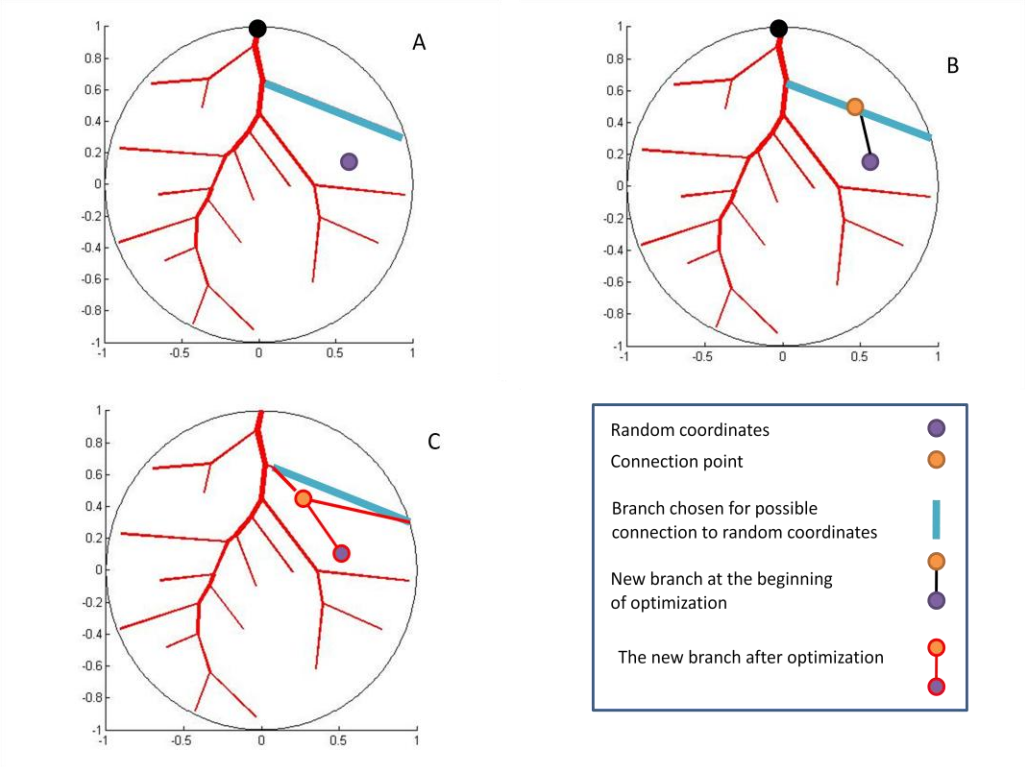

Figure 40: Schematic figure showing the change of the geometry of the new bifurcation that is formed when a new branch is added to the existing binary tree.

This adding of the new branch results in a splitting of the existing segment into two segments which now have different lengths. Once the values of the segments involved in the new bifurcation have been recalculated to meet the boundary conditions the optimization of the new bifurcation can commence. The optimization is done by finding the minimum total volume of the binary tree including the new segment, Figure 40. The total volume of the tree is calculated using the following equation

$$T = \pi \sum_{i=1}^{N_{tot}} l_i r_i^2, \quad (11.29)$$

In order to find the minimum volume and therefore the optimum geometry for the new bifurcation the connection point is moved slightly by changing the x and y coordinates. Following each incremental change on x and y a scaling up to the root is conducted in order to change the root radius and meet the boundary conditions. This results in a change of the total volume of the whole tree which subsequently requires a new calculation of the volume of each branch in the tree. This recalculation after each incremental change in x and y coordinates becomes increasingly time consuming as the tree grows. Small incremental changes to the x and y coordinates of the connection point are used to estimate the gradient of the target function T using the following equations:

$$\nabla T = \frac{\partial T}{\partial x(Connection\ point)}, \quad (11.30)$$

$$\nabla T = \frac{\partial T}{\partial y(Connection\ point)}, \quad (11.31)$$

The connection point is repeatedly moved along its descending gradient ending up with a geometric optimization of the possible connection point. This is repeated for all the possible connection points and finally the connection producing the lowest volume is chosen to be the next terminal end for the growing tree.

11.2 Search algorithms

Working with the data structure of a binary tree requires search algorithms that are able to travel throughout the tree. Two types of search algorithms are used in the binary tree program. The *tree search* visits the whole tree systematically whilst the second one *bread crumb search* [46] follows a marked path from the root to a specified bifurcation.

11.2.1 Tree search

When at a bifurcation junction in the binary tree produced by the SM model there are always two daughter segments, a right and a left segment. This is true for all nodes except for the root inlet node which only has a right segment. In order to travel the tree, two pointer objects are created named *traveller* and *follower*. The pointers travel through the tree starting at the root and moving down the tree. Due to the binary structure of the SM tree it can be divided into two subtrees immediately after the *root segment*. These subtrees are simply referred to as the right and left subtree, Figure 41, coloured red and blue respectively. In this figure the object pointers are positioned at the root of the tree as they would be at the start of a search through the tree. At the beginning of the search algorithm the right subtree is first traversed and then the left subtree.

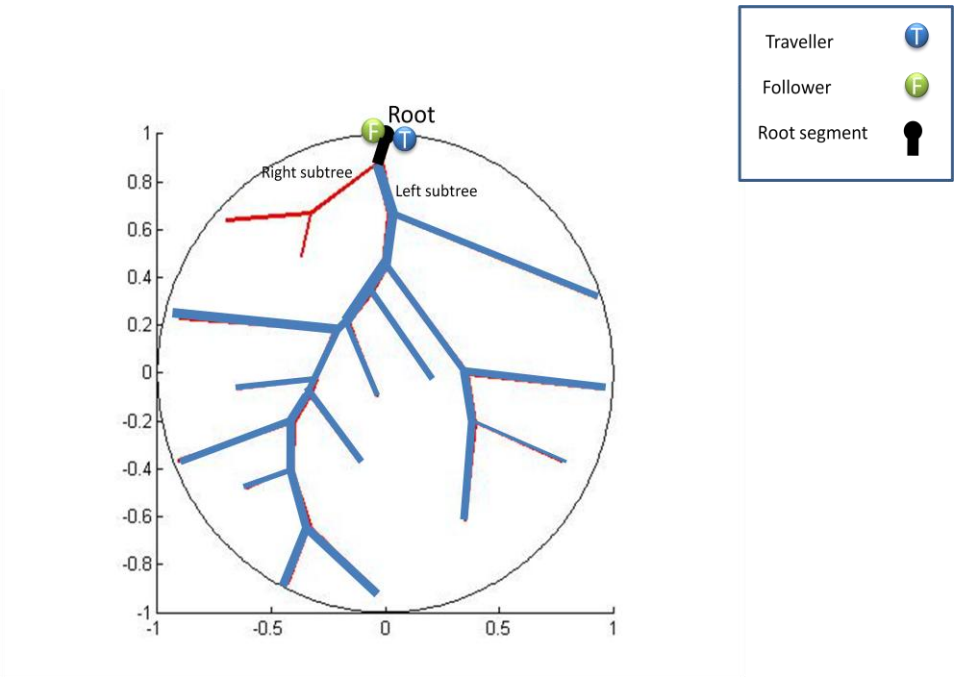

Figure 41: Schematic figure showing the two subtrees, right and left. The left subtree is indicated by blue branches. Also showing the position of the pointers, traveller and follower in an arterial tree at the beginning of the tree search algorithm.

When the right subtree has been traversed, a tree counter index is incremented and the traveller sent down the left subtree. Once the traveller has traversed the left subtree it reaches the root for the last time incrementing the tree index and exiting the search function.

The traveller pointer controls the overall movement through the tree. However the decision at each junction also depends on the position of the follower. When travelling down the tree, away from the root, the follower will always be higher in the tree structure, or closer to the root Figure 42 (A). First the traveller determines the positions of the follower in the tree. When the follower is higher in the tree than the traveller in relation to the root it means that the traveller is travelling down the tree and therefore will go down and to the right, Figure 42 (A).

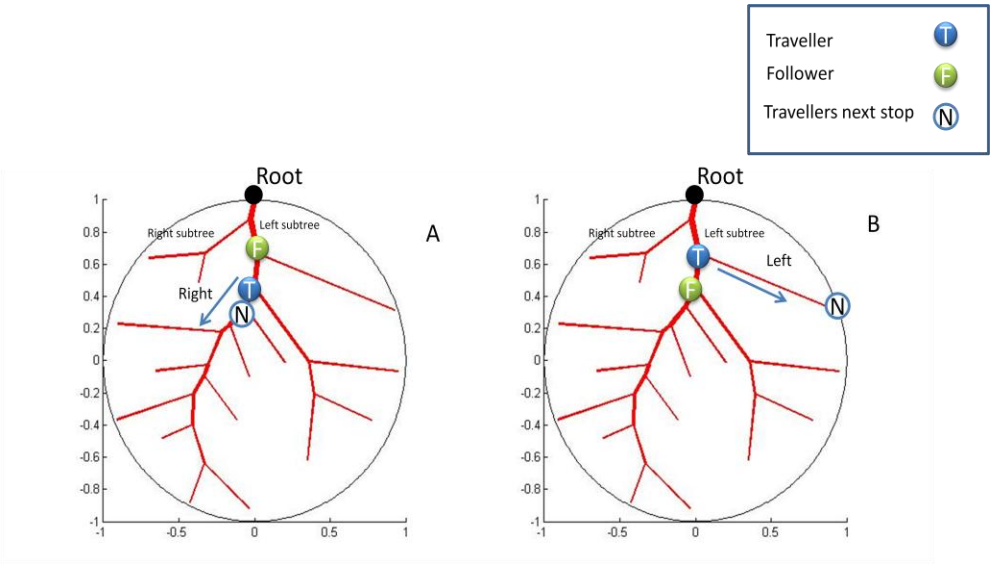

Figure 42: Schematic figure showing the movements of the traveller and follower pointers. (A) moving down the tree. (B) moving up the tree

The traveller moves one node down to the right and the follower follows by moving to the same node previously occupied by as the traveller. When travelling up the tree the follower will be lower in the tree in respect to the root Figure 42(B). Again the path chosen will depend on the follower's position. This time the precise position of the follower is needed, not only whether it is below or above. If the follower is sitting in a right node as it does in Figure 42 (B), then the traveller will go down towards the terminal end to the left as indicated in Figure 42Figure 42 (B). The follower will then move to the same node as the traveller occupied before. If on the other hand, the scenario in Figure 42(B) had been that the follower was sitting in a *left* node then the traveller would move up the tree structure by one node towards the root. The follower would still follow like before by occupying the exact same node as the traveller had vacated.

The tree search function is able to search through both irregularly and regularly built binary trees.

Figure **43** explains the tree search function schematically.

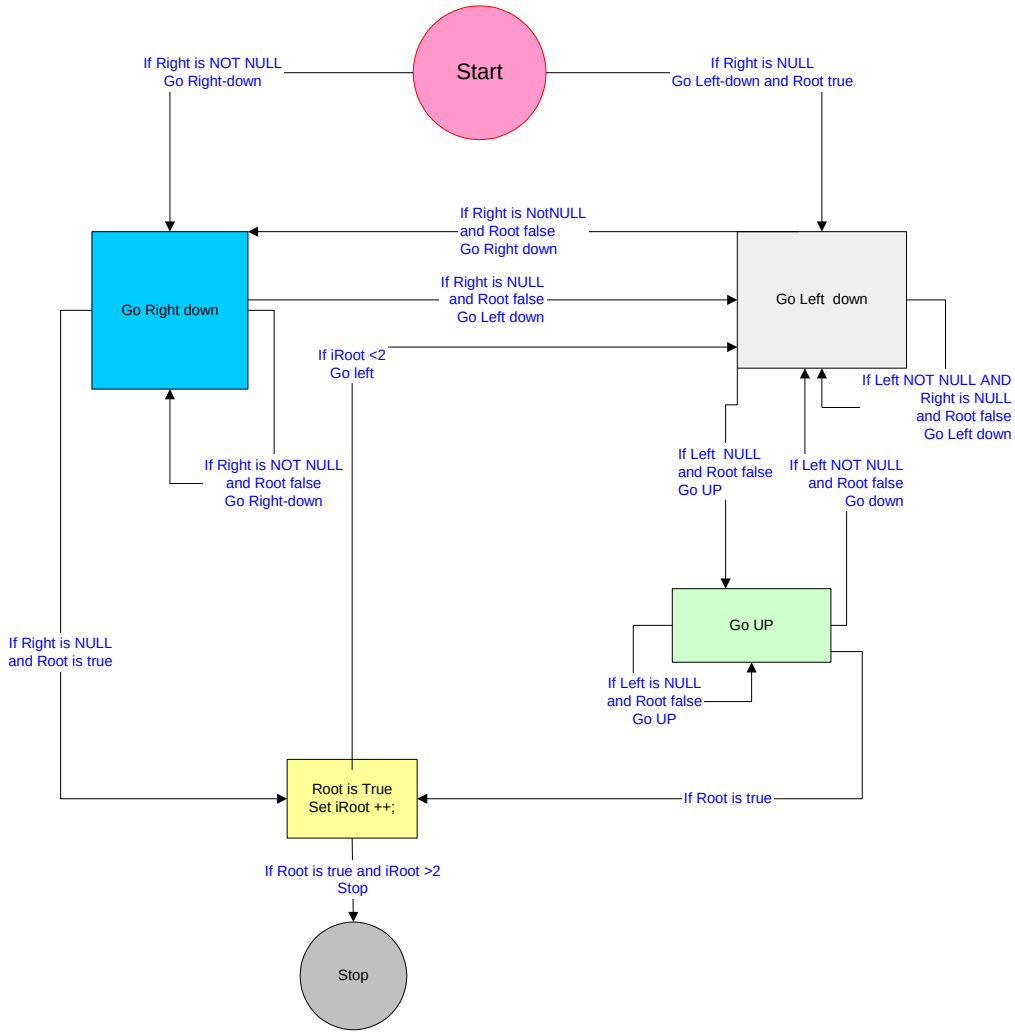

Figure 43: Schematic figure representing the tree search algorithm. The tree is divided into two subtrees, right subtree and left subtree. There are two pointers the traveller and the follower. The follower is always one node behind the traveller. The search starts in the root of the tree, going down to the right. The traveller always starts by going to the right and down in the tree .If the traveller cannot go to the right, it goes to the left and down. When the traveller has visited all the terminal ends of the right branch of the tree, it goes up to the root and down the left branch of the tree. Following the same rules as it did before. When the traveller has visited all the terminal branches of the left branch of the tree it goes up the root and stops.

11.2.2 Bread Crumb search

All segments radii are stored as ratio of parent radii with only the root holding the real value of the radius. When optimizing the connection bifurcation the total volume of the tree is required. Each nodes store the subtree volume in respect to its node as well is its own branch volume. When a new segment is added, it's volume is needed and therefore the real radius for the segment is required. Due to the radii ratio dependency it is necessary to calculate the real value of the radii from the root down to the desired vessel segment.

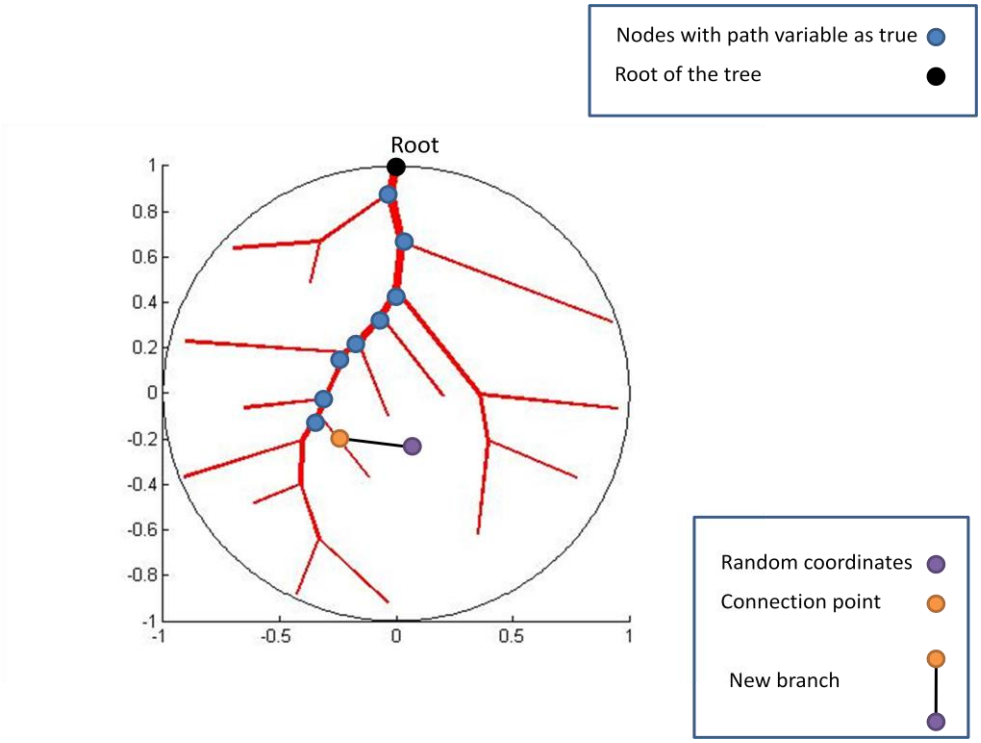

Figure 44: Schematic figure showing the bread crumb path formed by giving the variable path the value true, leaving a bread crumb to follow through the tree structure back to the connection point.

The bread crumb search was developed to enable travelling straight down from the root to a specific branch using the path variable, as bread crumbs

[46], rather than search through the whole tree using the tree search algorithm. Laying the bread crumb path is done to simplify the calculation of the real radii of the branches. Once the connection point is found and the new terminal segment has been added, the optimization function is run to find the minimum possible volume for the tree structure.

In order to find the real radii for the branches of the bifurcation that is being optimized it is necessary to travel up to the root from the bifurcation. Before leaving each node on the way up the tree, the path variable is set to true, leaving bread crumbs behind, Figure 44 . Once at the root the real value radius is put on a stack and now travelling down to the connection point is simply done by following the path variables, or metaphorically put, following the bread crumbs. In each node the daughter radius is calculated using the value that is stored on the top of a stack. The radius calculated is then put on the top of stack and before leaving the node the path variable is set to false again.

11.3 Alzaidi model

The Alzaidi model [44] was developed to calculate the physiological values of the zero-dimensional tree produced using Mette Olufsen's binary tree generating algorithm, see section 10.3.1 [40, 47]. In order to evaluate and calculate the physiological properties of the SM binary trees , data from the T2000 tree was run through the Alzaidi model [44]. The length and radius of the T2000 needed to be reorganized to match the data structure of the Alzaidi model. Finally the radii and length from tree was downloaded into the Alzaidi model which calculated the pressure and flow rate of the tree.

The resistance was first calculated for each individual segment using Poiseuille's formula (equation 11.1). The total resistance was calculated from the bottom of the tree moving up to the root adding the resistance of a capillary

bed, to the arterioles. Due to the irregular structure and size of the SM tree radii, the capillaries depended on the radius size of the terminal vessel segment. If a terminal segments radii was too big to be considered an arteriole it did not receive an added capillary resistance.

In the Alzaidi model the viscosity of the blood is not a fixed value but calculated for each segment using the following equation derived by Pries et al [48]:

$$\mu = \left[1 + (\mu_{45} - 1)\left(\frac{d_i}{d_i - 1.1}\right)^2\right]\left(\frac{d_i}{d_i - 1.1}\right)^2, \quad (11.32)$$

$$\mu_{45} = 6\,exp(-0.085 d_i) + 3.2 - exp\left(-0.06 d_i^{0.645}\right), \quad (11.33)$$

where d_i is the diameter of an individual vessel segment. This is an improvement from the SM model which does not consider variability of the blood regarding it to be a constant value.

The total resistance of the tree was calculated using both the resistance in-series and in-parallel rules, see equation (11.3) and (11.4). Using the resistance of the whole tree, the pressure values and the flow rate was calculated starting at the root and moving down towards the terminal vessel segments.

Based on the inlet pressure P_a and outlet pressure P_v the pressure difference was calculated:

$$\Delta P = P_a - P_v \quad (11.34)$$

and the flow rate through the whole tree Q was calculated using the following equation rewritten from equation (11.1):

$$Q = \frac{\Delta P}{R} \quad (11.35)$$

In order to calculate the flow rate the tree is regarded as one big branch, see Figure 45(A).

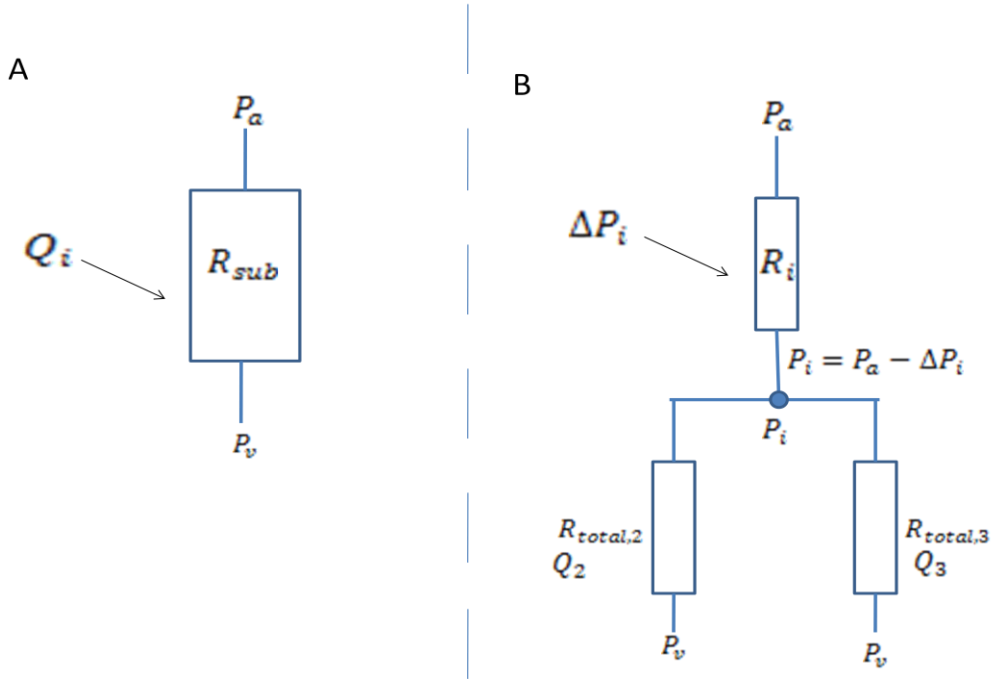

Figure 45: Schematic figure explaining the resistance and flow rate calculations in the binary tree.

Now the flow rate in the branch between P_a and P_v can be calculated using equation (11.35). We now move down the tree one level at a time. To calculate the pressure at node P_i we substitute ΔP in equation (11.34) with the right hand side of equation (11.35) which gives :

$$P_i = P_a - (Q_{Ttree}\, R_{Ttree}) \quad (11.36)$$

The pressure in P_i has now been calculated. Next we move down the tree to branches two and three where the flow rate is going to be calculated, Figure 45(B). First the resistance of the subtree of branches two and tree is required.

By adding the subtree of a chosen i-branch to the individual resistance of that same branch the total resistance R_{Ti} is found, as:

$$R_{Ti} = R_{sub,i} + R_{Individual\ ,i} \quad (11.37)$$

Here i represents a branch in the tree. Now the flow rate Q_2 and Q_3 can be calculated using equation 33 substituting the resistance of the whole tree with the resistance from (36) in the following way:

$$Q_i = \frac{\Delta P_i}{R_{Ti}} \quad (11.38)$$

Once the flow rate has been calculated for the branches the pressure for the individual branches can be calculated. This is procedure is repeated through the tree down to its terminal ends each time calculating the pressure and flow rate. The results are presented in the result and discussion chapter.

11.4 Geometrical properties

The geometrical properties of the T2000 tree were evaluated by calculating the angle between daughter segments as well as the bifurcation symmetry index which is defined as

$$bifurcation\ symmetric\ index = \frac{r_{smaller}}{r_{larger}} \quad (11.39)$$

where $r_{smaller}$ denotes the smaller daughter segment and r_{larger} the larger segment. The area expansion ratio was also evaluated in the following way:

$$Area\ expansion\ ratio = \frac{\pi r_1^2 + \pi r_{2..}^2}{\pi r_0^2} \quad (11.40)$$

where $r_1 and\ r_2$ denote the daughter segments and r_0 the parent segment. The distribution of the angle, bifurcation index and area expansion ratio were plotted and presented in the results and discussion chapter.

11.5 Statistics and Perfusion Area diagram

The perfusion area diagram is calculated and drawn in Matlab by dividing the area perfused by the T2000 tree into polygons of equal size using a method developed by Gringorten and Yepez [49]. The method begins by dividing the circle of overall radius *R* into a central unit circle of radius δr and *M* rings, each ring of the thickness $2\delta r$ where

$$(2M + 1)\delta r = R \quad (11.41)$$

The unit area δA is that of the central cell

$$\delta A = \pi(\delta r)^2 \quad (11.42)$$

The circle that includes the first ring has the radius $3\delta r$, and the area $A_1$is given by

$$A_1 = 9\pi(\delta r)^2 \quad (11.43)$$

While the area of the first ring or annulus δA_1 is:

$$\delta A_1 = 8\pi(\delta r)^2 \quad (11.44)$$

Then the first ring is divided into 8 equal cells, each cell equal to the area of the central unit cell δA. In the same way the second ring will have an outer radius of $5\delta r$ and is divided into 2x8 cells each having the area δA. The m^{th} ring can be divided into 8 cells each having the area δA. The total number of cells I_m up to and including the m^{th} ring is:

$$I_m = (2m + 1)^2 \quad (11.45)$$

The total area A_m is then defined in the following way:

$$A_m = (2\mathrm{m} + 1)^2 \pi(\delta \mathrm{r})^2 \quad (11.46)$$

All the terminal segments have the same flow rate as explained previously, therefore by counting the number of terminal segments entering each polygon a relative perfusion per unit area is acquired. Morphometric statistics for the SM trees T2000 and T250 are also calculated and plotted using Matlab.

12 Results and discussion

The simulation model (SM) program developed for this thesis produces a binary tree structure that resembles an arterial vessel structure. The SM program is based on the constrained constructive optimization (CCO) method developed by Schreiner and Buxbaum[25], as described in the Methods chapter. Two SM binary trees were grown, a tree of 2000 terminal nodes (T2000) and a tree of 250 terminal nodes (T250). The growth of the T2000 tree was observed at 15, 75, 150, 500, 1000 and 2000 terminal node intervals. The statistics and geometry of the T2000 tree were investigated as well as its physiological properties by taking the radii and lengths of the T2000 tree and running it through a model built by Alzaidi [44]. The Alzaidi model calculates pressure and flow rates. The radii of the T250 tree are compared with a CCO binary tree of the same size. The SM T250 tree is also compared with experimental results acquired from corrosion casts from two human hearts.

Initially the results from the T2000 tree are investigated, followed by the comparison of the SM T250 tree with a CCO tree model and other experimental results[28]. Finally the efficiency of the SM program is discussed.

12.1 Graphical results

The six different intervals from the T2000 run weres plotted and are presented in Figure 46.

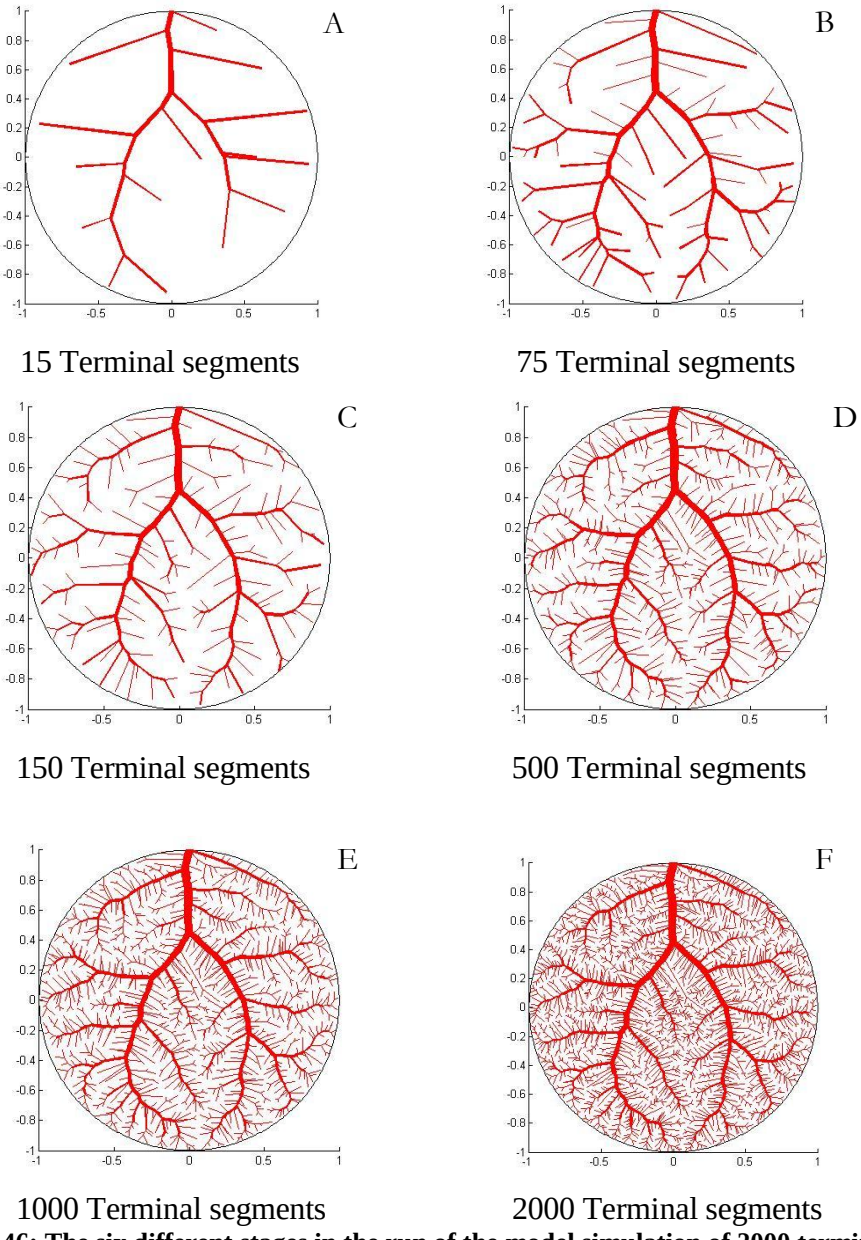

Figure 46: The six different stages in the run of the model simulation of 2000 terminals. (A) The basic structure of the tree is evident at 15 terminals and becomes increasingly clear as the number of terminals grows (B, C, D and F).

When looking at the trees from A to F it can be observed that the basic geometry of the tree is determined quite early in the growth process.

Once 15 terminal segments have been planted the basic structure of the tree can be seen. Subsequent segments increase the density of the tree structure rather than changing its basic geometrical structure.

The boundary conditions guiding the growth of the SM binary trees are the terminal flow rate and terminal pressure. Each time a new terminal segment is added to the existing tree structure, the tree radii need to be adjusted so that the boundary conditions of terminal flow rate are satisfied. This change in root radius at different stages of the SM T2000 growth can be observed in Table 6.

Table 6: Root radius of T2000 binary tree at six different intervals.

Root radius (cm)	N_{term}
0.1425	15
0.1506	75
0.2132	150
0.2155	500
0.2178	1000
0.2182	2000

$N_{term} = number\ of\ terminal\ segments$

Table 6 shows the increase in the root radius as the number of terminal segments grows. When a new segment is added to the SM tree the root radius is increased to meet the previously mentioned boundary conditions. This increase in root radius between different stages therefore demonstrates a correct behaviour of the SM algorithm in relation to the compensation of root radius when a new segment is added to the tree structure.

In Figure 47, the SM tree can be seen in comparison with the CCO tree produced by Schreiner and Buxbaum [25]. The first immediate difference is the density of tree structures. The CCO tree has 4000 terminals segments whereas the SM tree has 2000.

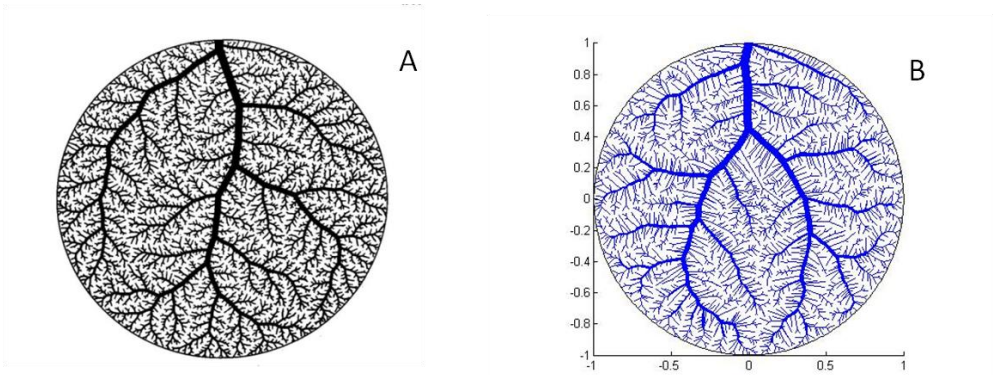

Figure 47:Schreiner and Buxbaum tree of 4000 terminal segments (A) [25]. The SM tree T2000 (B).

Figure 47 also shows that the majority of the CCO tree segments have been successfully bifurcated into short segments. However in the T2000 tree there are still terminal segments that are not fully bifurcated resulting in longer terminal segments. This difference is likely to be related to having fewer terminal segments in the SM tree. The decision to use a T2000 tree rather than a tree of 4000 terminal segments, was based on long run times of the SM program, see section 12.8. The difference between the SM and the CCO trees in relation to the geometry of the bigger arteries is the result of different random number generators used. The random numbers drawn from the random array determine the position of the first segments of the SM tree. From Figure 46 it is apparent that the first segments planted will become the biggest arteries of the fully developed tree.

12.2 Morphological Results

As discussed in the Literature Review chapter the definition of branch or vessel of an arterial tree differs between researchers. In this thesis a vessel has been defined as the segment between any two bifurcations. The vessel is assumed to change its identity when a bifurcation occurs regardless of the both

size of the bifurcation vessels [32] or its degree in relation to the Strahler order[50]. Here, the term vessel segment or segment is used when referring to an arterial segment in the SM binary tree. The total number of bifurcation levels is counted from the root to the most distal terminal bifurcation and was found to be 192 in the SM T2000 tree. The average bifurcation level reported by Karch et al was 103 bifurcation levels with a first and third quartile of 73-129 respectively [42] .

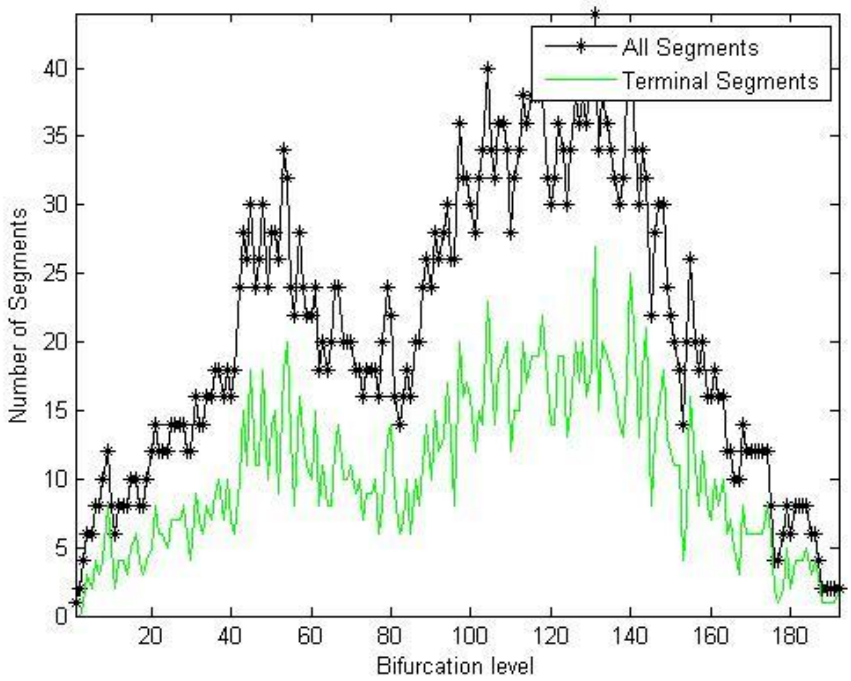

Figure 48: The total number of segments (black) and the number of terminal segments (green) per bifurcation level of the SM T2000 tree.

Figure 48 shows how both the total number of segments as well as the terminal segments in the T2000 tree are distributed throughout the bifurcation levels. The terminal segments are not restricted to the lower bifurcation levels of the tree and are therefore found at every level of the tree. The numbers of segments steadily increase from the root to the 60th bifurcation level of the

tree. At levels 60 to 80 the number of branches decrease slightly, but then increases sharply again from levels 80 to110 where the number of segments reach a maximum. From bifurcation level 150 onwards the number of segments quickly decreases again.

Figure 49 shows the mean radius of the SM T2000 tree. The root radius is 0.22 cm and moving down from the root towards the terminal segments the mean radii at each level decreases quickly.

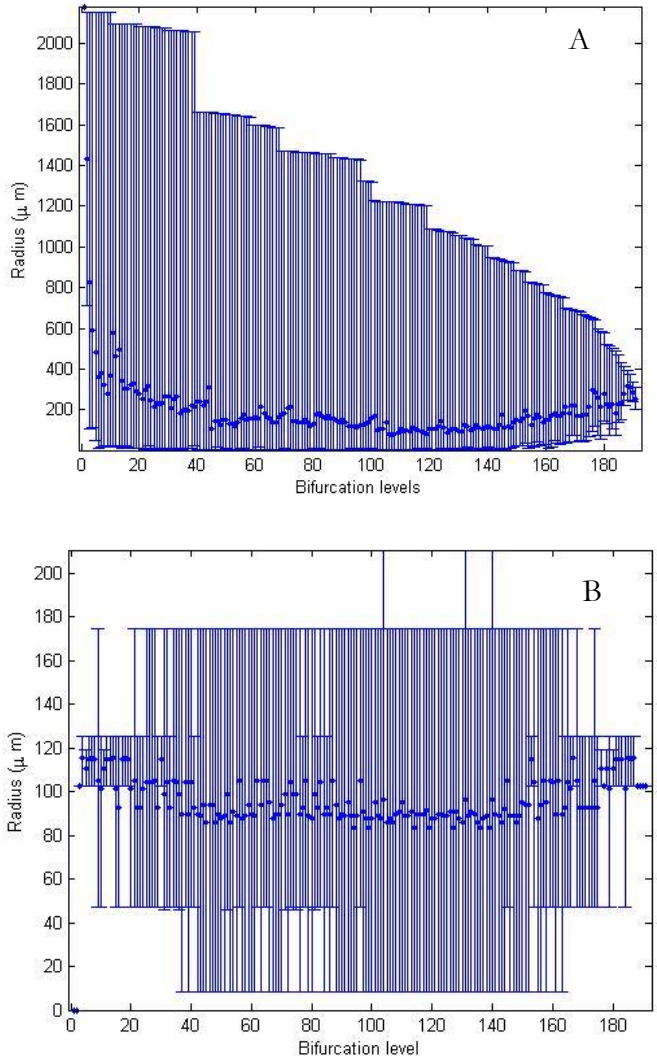

Figure 49: (A) The mean radii of the SM T2000 as well as the maximum and minimum values. (B) The mean radii of the terminal segments of SM T2000 tree as well as the maximum and minimum values.

At level twenty the average radii seems to reach a mean value around 200 μm ranging from 75-300 μm. Moving downstream from the root it can be observed that the maximum radii values decrease, also that the range of the radii values becomes smaller. The reason for that is that the segment radii steadily decrease with increasing bifurcation levels. Figure 49(B) shows the

average radii of terminal segments at each bifurcation level. The average terminal radius for the whole tree is 66.8 μm and would therefore be classified as a tree of small terminal arteries. However, looking at Figure 49(B) we can see that the smallest arteries found at bifurcation levels 38-170 are too small to be classified as arteries and indeed the smallest segment in the T2000 is only 8 μm which can be classified as either arteriole or a precapillary segment [6]. The segments in the SM T2000 tree therefore range from arterial size to arteriolar size.

In Figure 50 the diameter from the SM tree is compared with the experimental results of Lauwers et al

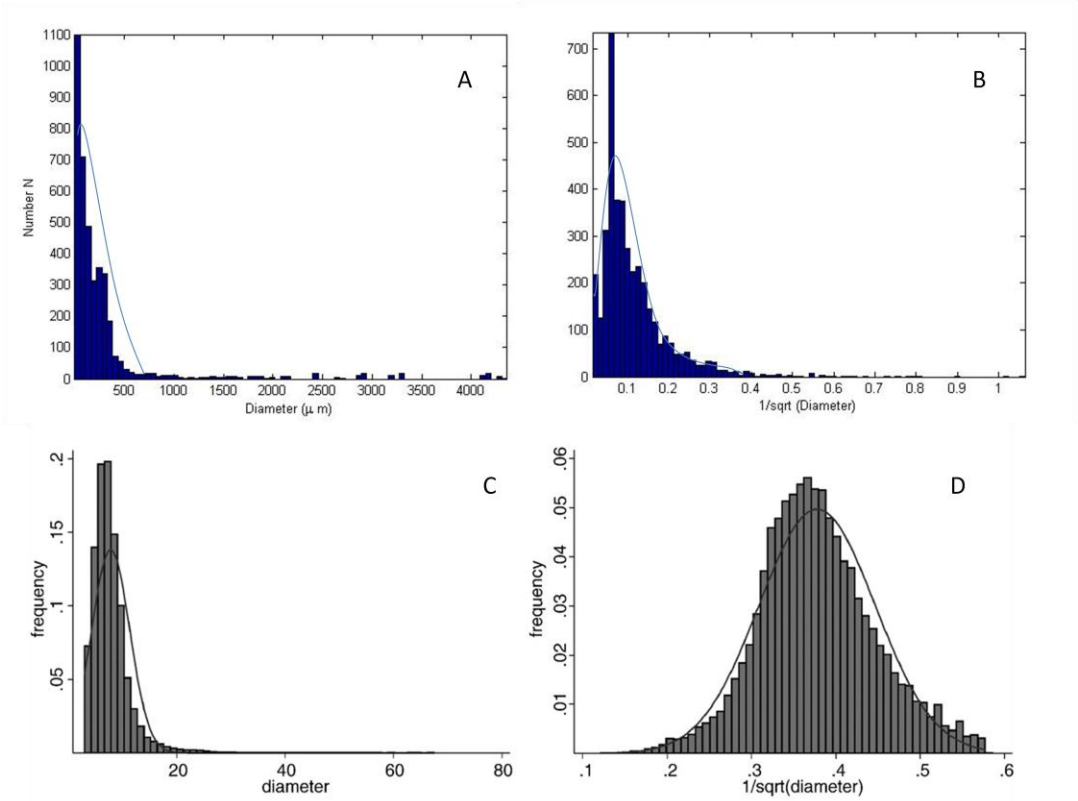

Figure 50: (A) The distribution of segment diameters from the SM tree of 2000 terminals. (B) Shows the distribution of diameter mapped with inverse square root mapping. (C) The distribution of Lauwers et als results diameter. (D) The distribution of Lauwers et als result diameter with inverse square root mapping.

When comparing the SM diameter with the Lauwers et al findings the difference in diameter size between the two trees is noted, Table 7. The reason for this difference can be explained by the basic difference in tree samples being compared. The arterial tree sample investigated by Lauwers et al mostly includes arterioles while the SM T2000 tree includes segments ranging from arterial level to arteriolar level. Lauwers et al mapped their diameter findings in order to establish normal distribution by using the inverse square root of the diameter. This mapping of the radii was also done on the SM T2000, Figure 50 (B). The mapping of the SM radii did not result in a normal distribution. However there is some indication of a skewed normal distribution which could possibly become clear in a SM tree with a higher number of segments.

The relation between daughter and parent diameter of the SM T2000 tree was considered. At each bifurcation the two bifurcating segments were classified as smaller or larger than the parent segment. The results can be seen in Figure 51 (A, B) as logarithmic plots, where the daughter segment diameter is plotted as a function of the parent segment diameter. For comparison, Figure 51 also shows results from experimental [50] and CCO model tree [31], Figure 51 (C,D,E,F).

We can see from Figure 51 that the daughter–parent relationship in the SM tree compares well with both the experimental data [50] and the results reported from the CCO model tree[31]. Figure 51 (A) shows that in the SM tree the larger daughter segment is always of the same magnitude as the parent segment or slightly smaller. On the other hand, Figure 51 (B) shows that the smaller daughter segment varies much more in size. In some instances there is not much difference in the size of the parent segment and the smaller daughter segment. This is also found in the porcine coronary tree as can be seen in

Figure 51 (D), demonstrating a natural occurrence in an arterial tree. The SM tree also shows good agreeance with the CCO tree, Figure 51 (E, F).

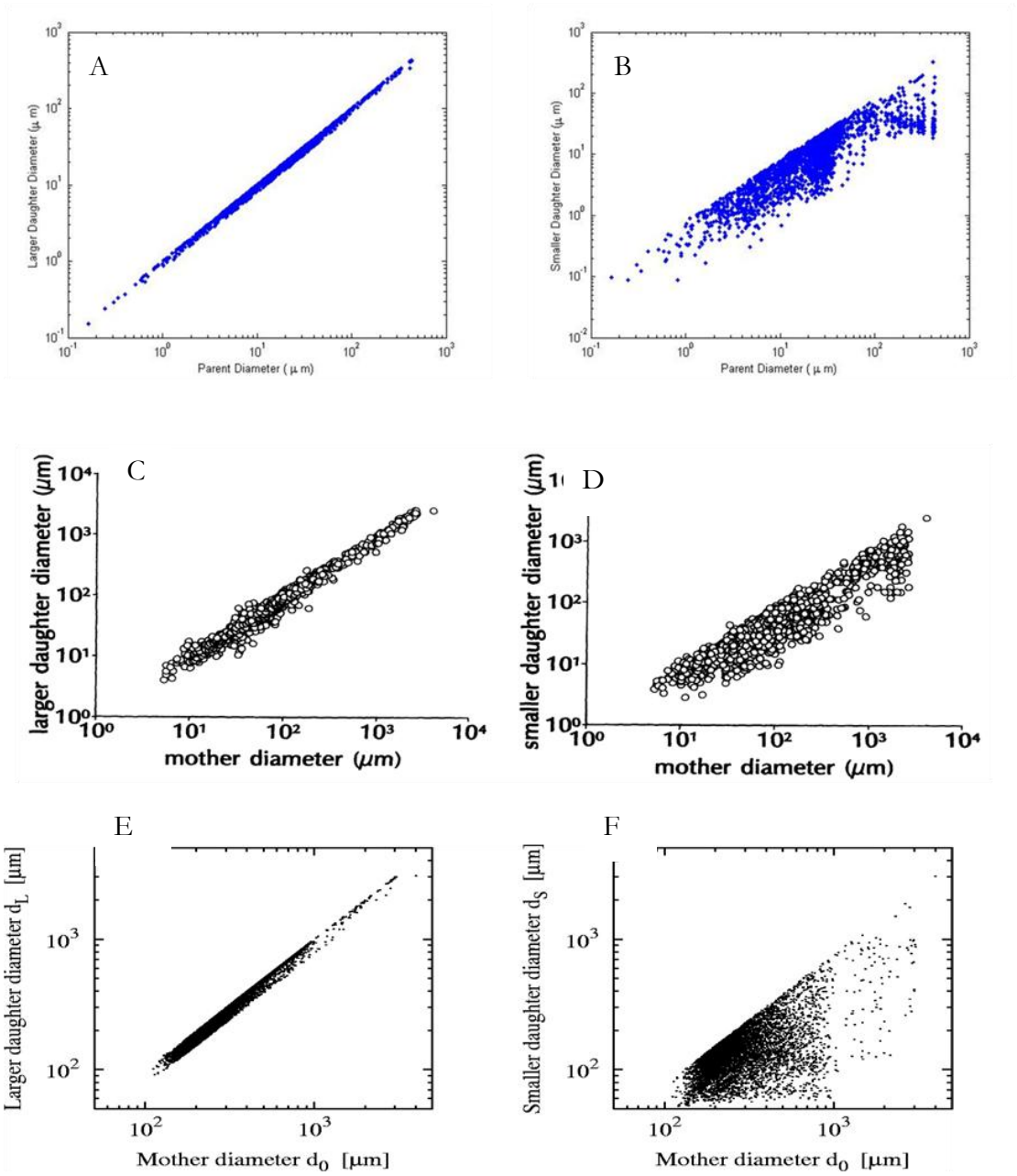

Figure 51: Logarithmic plots of smaller and larger daughter segments from three different arterial trees: the SM tree (A,B) the porcine coronary tree (C,D) [50] and the CCO tree (E,F) [31].

The length of each segment in the SM tree was also examined. The mean length of the segments in the T2000 tree was calculated to be 15.3μm, Table 7. In comparison with both Lauwers et al [29] and Karch et al [42] the mean segment length turned out to be shorter, although the distribution in Figure 52 shows good correlation with the distribution reported by Lauwers et al.

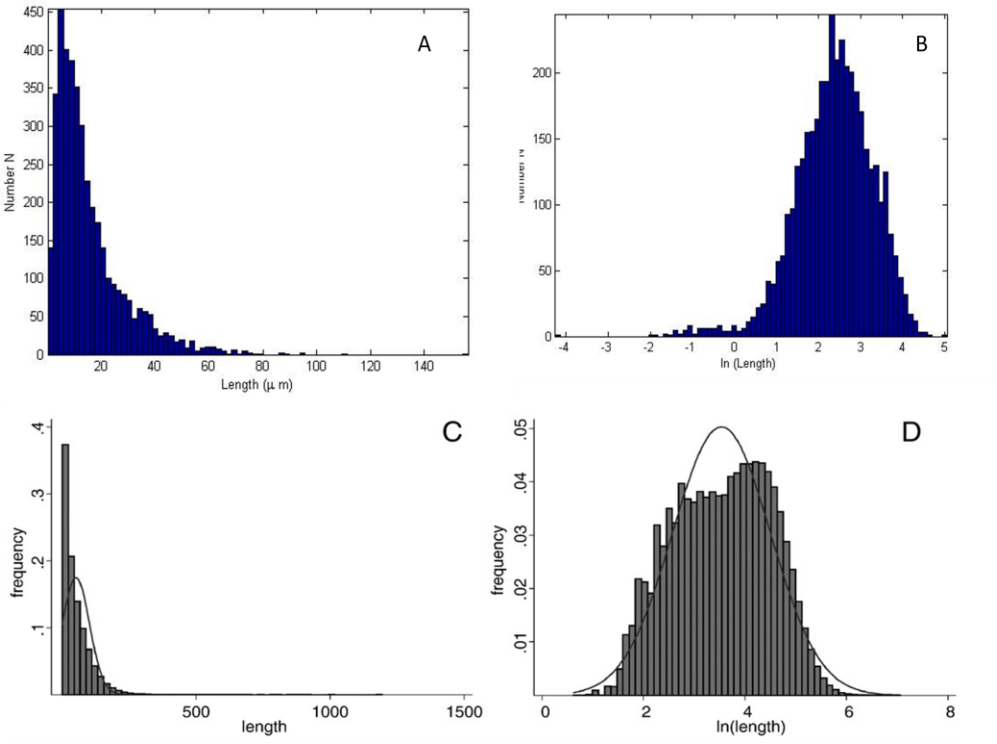

Figure 52: Comparing segment lengths of SM tree of 2000 terminals and experimental results published by Lauwers et al [11]. Figure A shows the distribution of SM tree without mapping while figure B show the results with logarithmic mapping of the length. The results from Lauwers et al's research are presented in figures C and D for comparison.

The length of the SM tree segments has a log normal distribution and also shows good comparison with the mapped results from Lauwers et al's experiments, Figure 52 (B, D). However, the segments from the SM tree are shorter, due to the constraint area size in which it is grown. The SM tree is

grown in a circle with a radius of 5 cm whereas the Karch et al [42] tree was grown in a square with sides of 44.7 cm. The length of the segments in the tree are directly related to the area radius in which it grows, so by increasing the area radius the length of segments of the SM tree will increase. This is an important difference because, although the segments are shorter, it indicates that the SM segments lengths in the tree are correctly distributed.

In Table 7 the comparison of the SM tree properties with experimental results from Lauwers et al [29] and Karch et al CCO model [42] are summarised.

Table 7: SM T2000 compared with Lauwers et al and Karch et al results.

	Lauwers et al [29]	SM T2000	Karch et al[42]
Mean segment diameter	7.82	304.9	-
Median tree diameter	7.19	127.1	260
Bifurcation levels	-	192	108
Mean segment length	52.7	15.3	-
Median segment length	36.1	11.3	189

12.3 Geometric properties of T2000

The geometrical properties are investigated for the T2000 tree were: the branching angle between two daughter segments derived from the same parent; the bifurcation symmetry index (the ratio of daughter branches derived from the same parent); and finally the area expansion ratio (the ratio of the cross section area of the two daughter segment and the cross section of the parent).

12.4 Branching angles

The angle between the two daughter segments derived from the same parent segment was calculated. The distribution of the angles in the SM T2000 tree is shown in Figure 53.

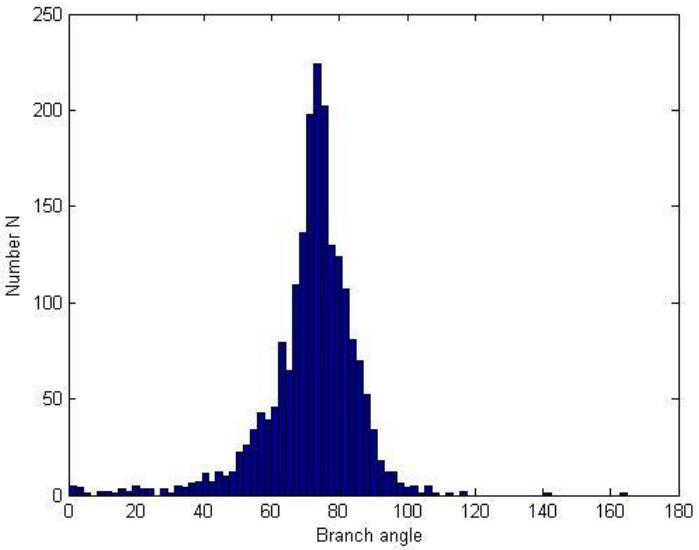

Figure 53: The distribution of the bifurcation angle in SM T2000

The mean bifurcation angle was calculated as 71.6 degrees and the median 73.3 degrees which corresponds well with the optimal theoretical angle calculated by Murray, namely 75 degrees for simple bifurcations. From Figure 53 we can see that the most frequently occurring angles lie in the range from 70-85 degrees. Frame and Sarelius conducted an experiment where the bifurcation angle was measured in the Cremaster muscle and the average angle calculated was 85 degrees [51]. The bifurcation angles in the SM T2000 tree therefore correlate well with both theoretical and experimental results.

12.4.1 Bifurcation symmetry index

The bifurcation symmetry index expresses the relationship between two daughter segments of the same parent. The distribution of the bifurcation symmetry index can be seen Figure 54.

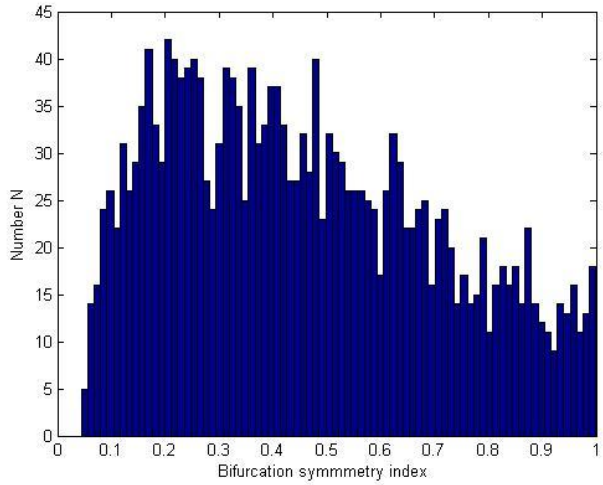

Figure 54: The distribution of the bifurcation symmetry index in the SM T2000 tree.

From Figure 54 we can see that the bifurcation symmetry index is relatively evenly distributed between 0.05-0.7. There's an increase from 0.05-0.2, with a decrease thereafter. It is difficult to draw strong conclusions from this single sample, however similar findings were reported by VanBavel and Spaan [50],Figure 55.

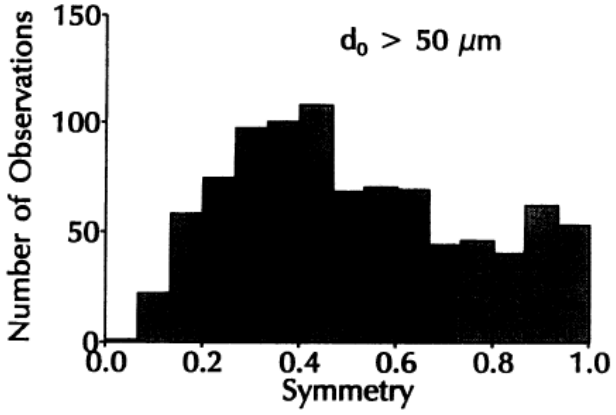

Figure 55: The distribution of the bifurcation symmetry index reproduced from VanBavel and Spaan research. The bifurcation symmetry was calculated for segments larger than 50 μm [50] .

Their measurements were performed on the porcine coronary arteries and the calculated bifurcation symmetry index can be seen in Figure 55. Zamir's experimental findings [38] however found the bifurcation index for the coronary arteries to be nearly uniformly distributed between 0 and 1.0.

The median of the bifurcation symmetry index in the SM T2000 tree was calculated as 0.43 and can be seen in comparison with other models and experimental results, Table 8.

Table 8: Comparing SM tree bifurcation symmetry index with other models and experimental results.

Arterial trees/models	Bifurcation symmetry index
Median SM T2000	0.43
Median VanBavel[50]	0.40
Median Karch[42]	0.56
Bifurcation symmetry constant from Mette Olufsen binary tree [47]	0.42

The bifurcation symmetry index calculated from the SM T2000 tree therefore shows good agreement with both experimental [50] and other binary tree models [42, 47].

12.4.2 Area expansion ratio

The area expansion ratio measures the cross sectional area expansion at bifurcations due to the radii of the parent and its daughter segments.

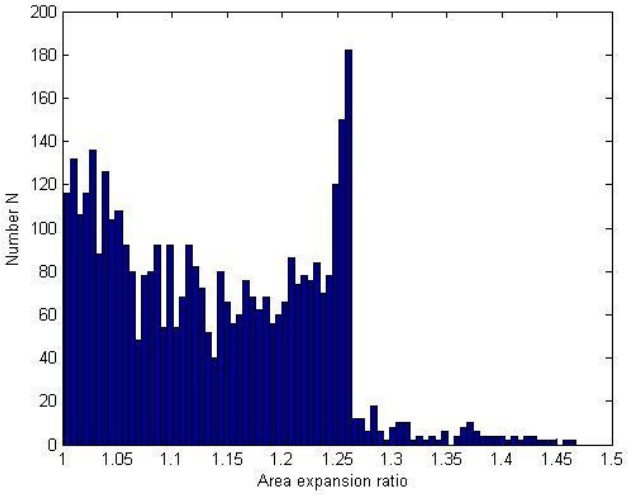

Figure 56: The distribution of the area expansion ratio.

Figure 56 shows the distribution of the area expansion ratio found in the SM T2000 tree with the median calculated as 1.2. Karch et al [42] found the median value for their tree area expansion ratio to be 1.8, whereas Zamir reported the most frequent value to be around 0.9-1.1 [38]. The area expansion ratio from the SM T2000 tree therefore shows better agreement with the experimental results [38] than the reported area expansion ratio found by Karch et al [42].

12.5 Flow rate per area

The SM tree algorithm assumes a constant terminal flow through all the terminal segments. By dividing the infiltration area of the SM tree into polygons of equal size, of total number of 441. By counting the number of terminal segment entering each polygon, a relative blood flow to each area was calculated,

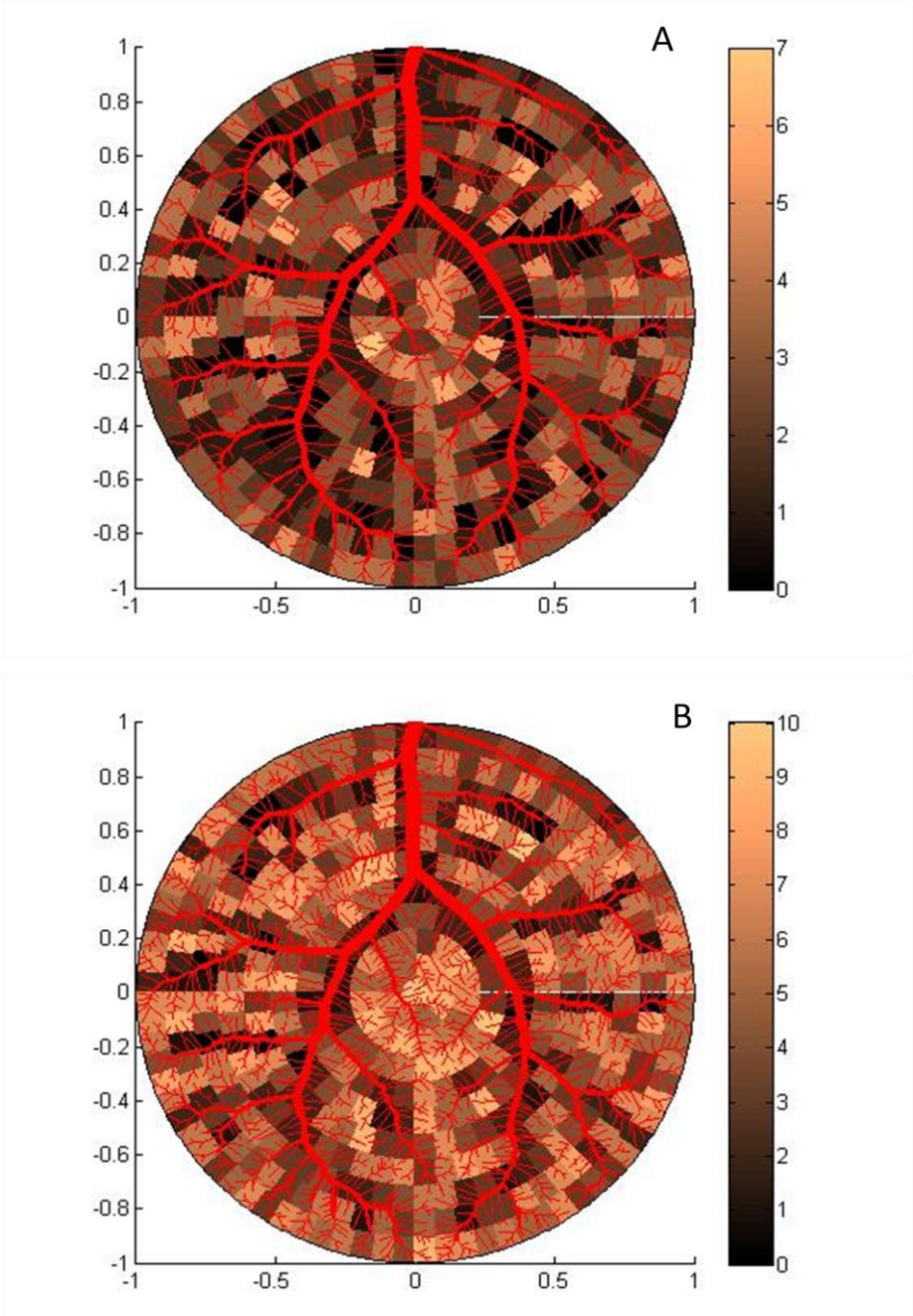

Figure 57: Perfusion diagram of different sized SM trees. Figure A shows the perfusion of a SM T1000 tree and figure B the perfusion of a SM T2000 tree. Darker areas indicate fewer terminal segments per area resulting in lower total blood flow to the specific area, while lighter colour area indicate more terminal segments to the specific area, resulting in higher total blood flow to the area. Scales indicate number of terminal segments

The SM algorithm aims to produce a binary tree that provides even flow to the infiltrated area. Figure 57, shows graphically the difference in perfusion of the T1000 and T2000 SM trees. In Figure 57 (A) the T1000 tree demonstrates multiple areas of poor perfusion compared to the T2000 tree, Figure 57 (B), which can be explained by a smaller number of terminal segments.

A similar pattern is seen in both trees, where the areas with better perfusion lie in the center as well as midway between the bigger segments. This can be explained by looking at the structure of the tree. The main arteries form a semicircle around the centre, causing the majority of the tree segments of to arise from the centre. This means that there is a high chance of multiple terminal segments in the centre, resulting in greater density per area. Furthermore it can be appreciated that the areas of less perfusion lie parallel to the larger segments. That pattern might possibly dissapear with an increased number of terminal segments, resulting in better global perfusion.

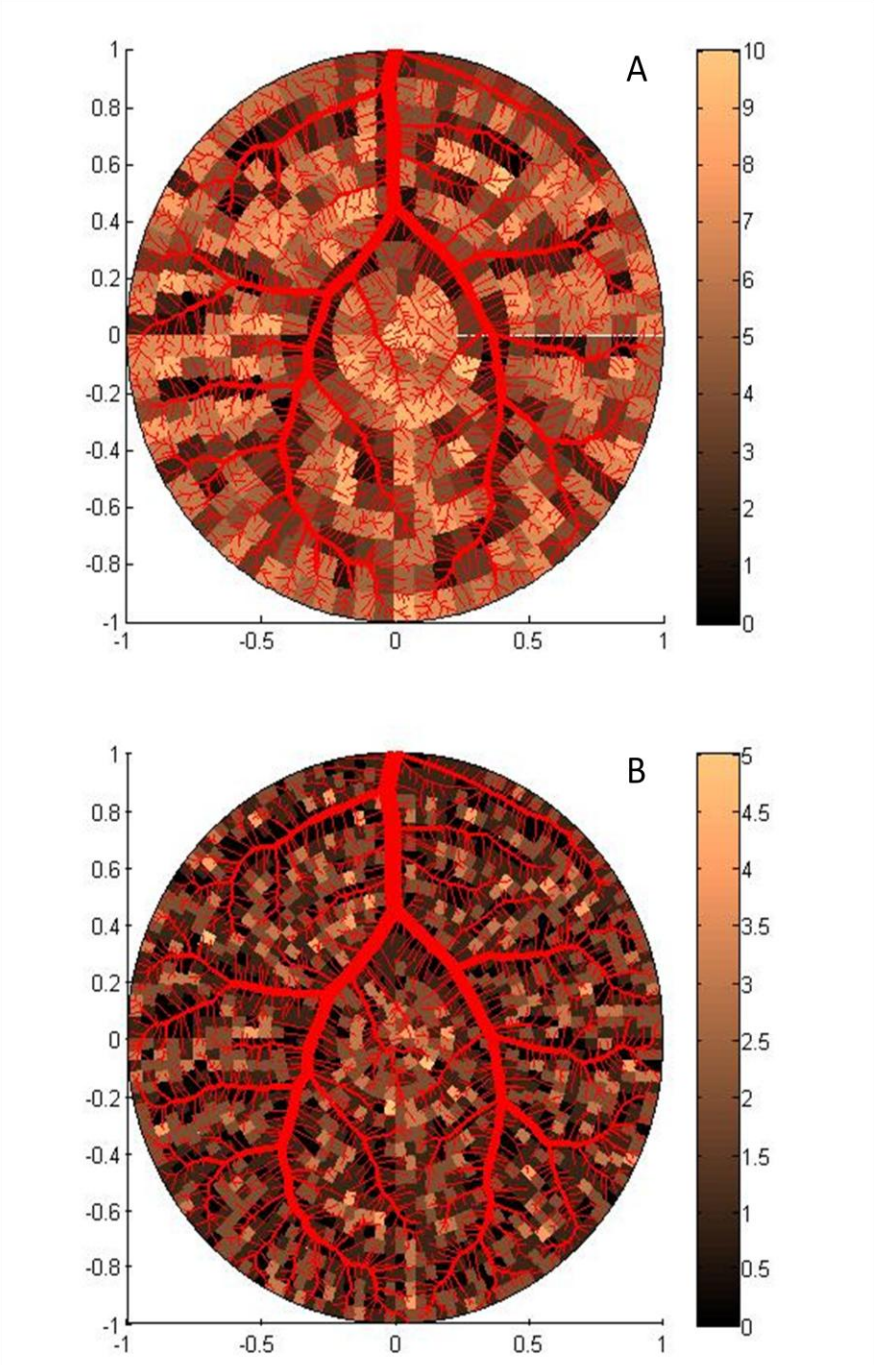

Figure 58: Perfusion diagram of the T2000 SM tree with, (A) 441 equal sized areas and (B) 1681 equal sized areas.

To further explore the perfused areas of the T2000 SM tree. The total perfused area was subdivided into even smaller equal sized areas, totalling a numbe of 1681 polygons. From Figure 58 we can see much more variation of perfusion to different areas. There is still a similar pattern, but the poorly perfused areas parallel to the bigger segments are much clearer. However it must be noted that the total number of equal sized areas is approaching the total number of terminal segments of the T2000 tree.

This disproportionate pattern of perfusions to different areas is a natural occurrence in the brain, a phenomenon known as watershed areas [1]. Although these diagrams from the T2000 run cannot effectively be compared to experimental results it is evident that its pattern behaviour is well known in vivo and the association between Alzheimers disease and increased number of watershed infarcts has recently been demonstrated. [23].

12.6 Physiological Results

The SM algorithm ultimately produces a binary tree in two dimensions, where each segment has a length and radius. In order to evaluate the SM T2000 trees physiological properties, the radii and lengths of all segments in the tree were extracted and rearranged to match the data structure used in the Alzaidi model [44]. This model, developed and built by Alzaidi, calculates pressure and flow rate at each bifurcation level in the tree.

12.6.1 Pressure

The pressure in the T2000 tree was calculated at each level of the tree as described in the Method chapter. The pressure at each level as well as the distribution of pressure can be seen in Figure 59.

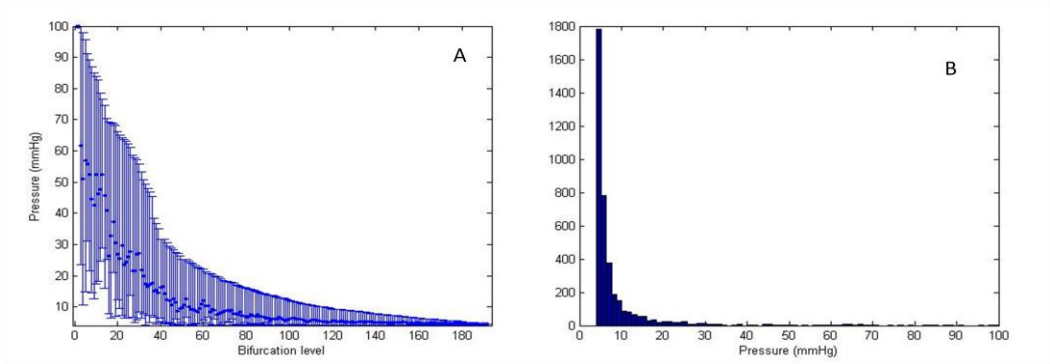

Figure 59: Pressure through the SM tree. (A) The average pressure of all segments per bifurcation level as well as maximum and minimum values. (B) The distribution of pressure in the SM tree.

From Figure 59 we can see that the pressure steadily decreses moving down the bifurcation level from the inlet pressure of 100 mmHg approching 5 mmHg. The drop in overall pressure within the SM tree corresponds well to physiological data on blood pressure variation from small arterioles to capillaries, Figure: 60. The distribution of pressure within the SM tree, Figure 59 (B), demonstrates that the most frequent pressure values lie in the range of 5-15 mmHg, corresponding to the pressures found at the capillary level. This agrees well with the terminal radii data, Figure 49 (B), from the T2000 tree where indeed the smallest segments are classified as precapillary.

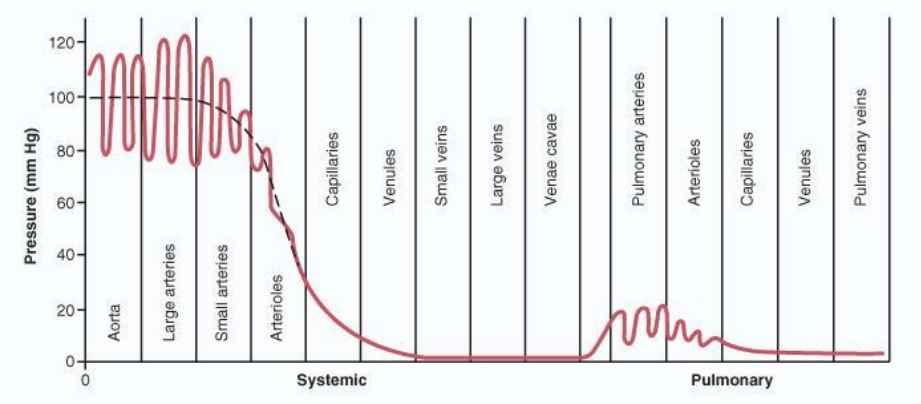

Figure: 60 The systemic and pulmonary circulation pressures in the human body [6].

The pressure from the T2000 tree was also examined in relation to its radii and can be seen in Figure 61.

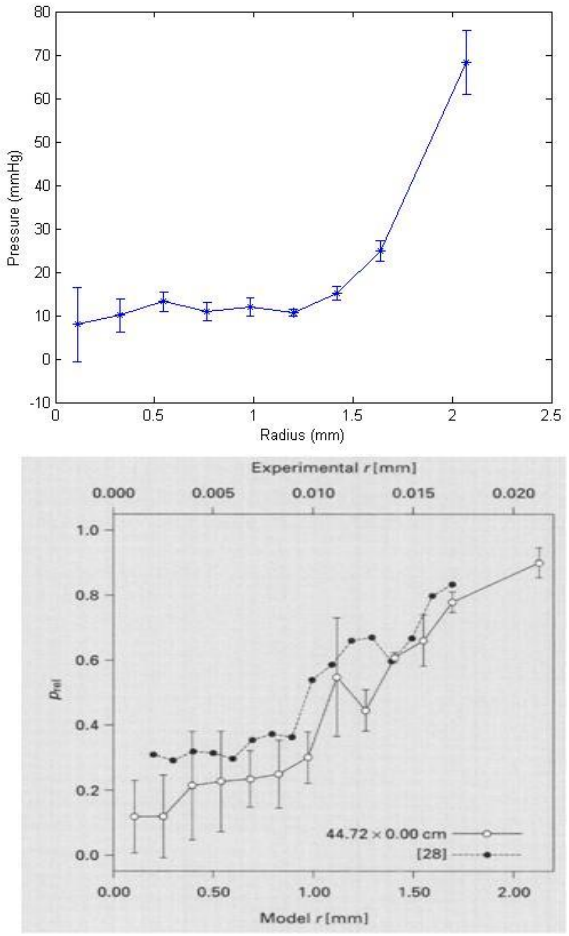

Figure 61: (A) Pressure in the SM T2000 tree in relations to the segment radii. (B) Pressure found in Karch et al [42] tree in relation to the radii of the segments (○), experimental data from rat mesentery (●). The dots represent the mean pressure value and the bars indicate standard deviation.

From Figure 61 the association between radii size and pressure is evident. In the segments with larger radii, the pressure is much higher and the smallest segments have the lowest pressure, as expected. This not only holds true for the SM T2000 tree, but also for the CCO tree of Karch et al and the

experimental results from the rat mesentery [42]. The is however a significant difference in the numbers of segments between the SM tree and the CCO tree presented in Figure 61. It should be noted that the COO tree has a total of 15999 segments while the SM tree has 3999.

12.6.2 Flow Rate

The flow rate through the tree was calculated as detailed in the Methods chapter. The SM tree flow rate can be seen in Figure 62 (A), in comparison with the flow rate calculated by Karch et al and the flow rate from the rat mesentery, Figure 62 (B). This figure shows the superimposed calculated line for flow rate in the SM tree is shifted to the left of the graph. This left shift is due to a larger calculated flow rate in the SM tree compared with the Karch et al model and the rat mesentery [42]. The explanation for this shift is the difference in the total number of segment terminals between the models as well as the difference in the perfusion area(A_{perf}). The SM tree contains a total number of terminal segments of 2000, compared with the 8000 terminal segments in the Karch et al model [42]. The terminal flow rate for both the Karch et al model and the SM tree is determined by an inlet flow rate of 500 ml/min as a constant, divided by the number of terminal segments in the tree. The terminal flow rate is therefore calculated to be 0.0625ml/min for the Karch et al model while in the SM T2000 tree it is 0.25 ml/min. The area in which the SM tree is grown results in relatively shorter arteries and together this is reflected in the relatively large arterial radii of the tree.

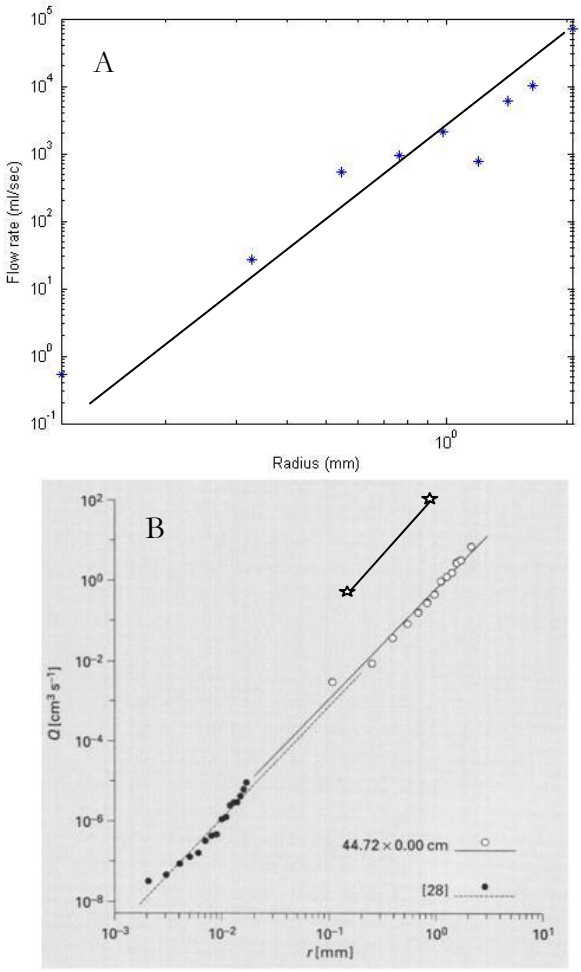

Figure 62 (A) the flow rate through the SM tree plotted on a logarithmic scale in respect to the tree radii. (B) the flow rate through the Karch et al model (○) and the flow rate in the rat mesentery (●) [42] with superimposed data from the SM tree (☆). Straight lines were fitted to the points of the model and experimental data.

The large radii and shorter length of the SM segments therefore result in a larger flow rate which is physiologically inaccurate. This can be rectified by changing the values of the global variables in the SM program by increasing the terminal segment number or the area in which the SM tree grows.

12.7 Comparing experimental result with T250

The second SM tree grown was a tree of total 499 segments of which there were 250 terminal segments (T250). In Figure 63 the radii from the T250 is compared with the results from the CCO model of the same size as well as comparing it to experimental data [25]. Looking at Figure 63 A and B there is clearly a good resemblance between the SM model, the CCO model and experimental results. Also when the bifurcation levels one through ten are observed in regards to the radii we can see an excellent correlation between Figure 63 (A) and (B). At level fifteen in the SM tree there is a rise in the SM tree radii, explained by the different random number generators used. From level ten to twenty the SM model shows a span of diameter from approximately 0.75-1.5 cm, which compares well with Figure 63 (B) where a range of 0.5-1.25cm is demonstrated. From level twenty and onwards the SM model radii are between 0.5-0.75 cm, corresponding well with the CCO model but somewhat larger than the experimental results.

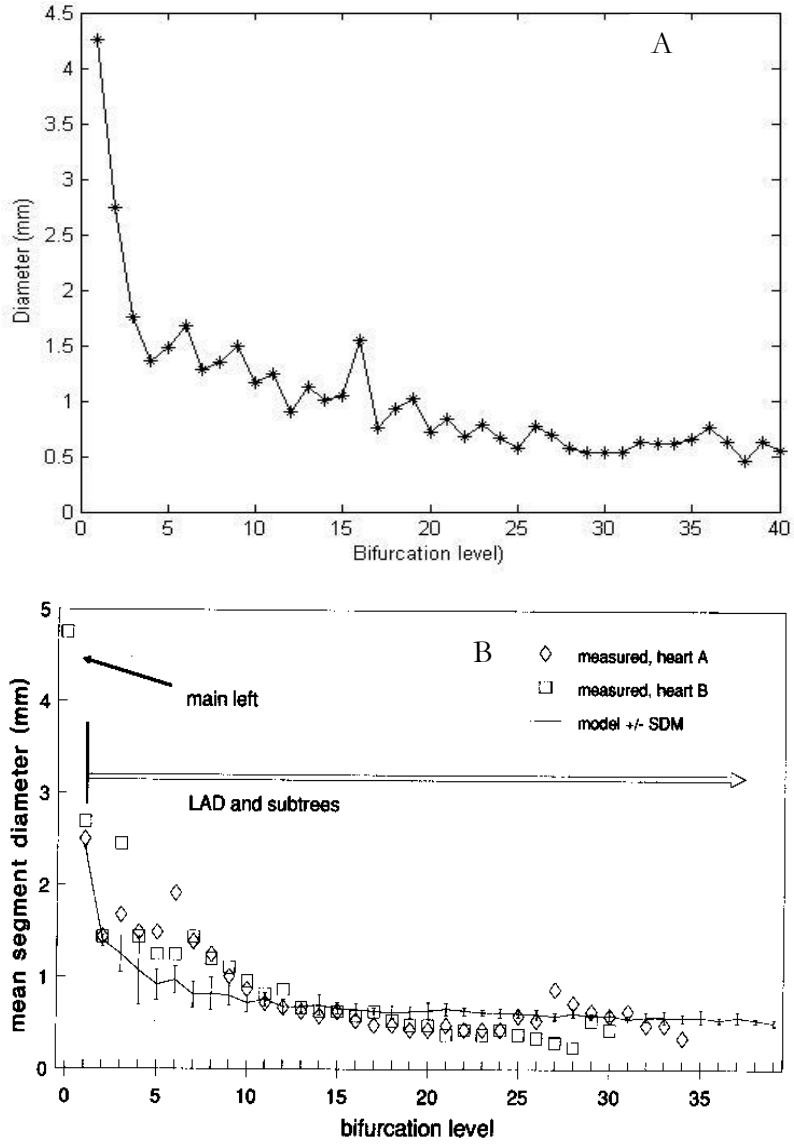

Figure 63: Comparison between SM results and the left coronary arterial trees of two humans. (A) Diameter of the simulation model with 250 terminal branches. (B) Schreiner and Buxbaum binary tree model diameter results and measurements form corrosion casts [25].

12.8 Run time results

The SM tree program was run on a Laptop computer, with an AMD Turion 64 X2 TL-62 processor (2.1 GHz, 2x512 KB L2 Cache), and 2GB DDR2 memory. The run time for the six different stages of the tree increased exponentially, Figure 64. The four smallest trees, T15 to T250, took from a few seconds to 20 minutes, respectively to process. For larger trees the run time increased rapidly.

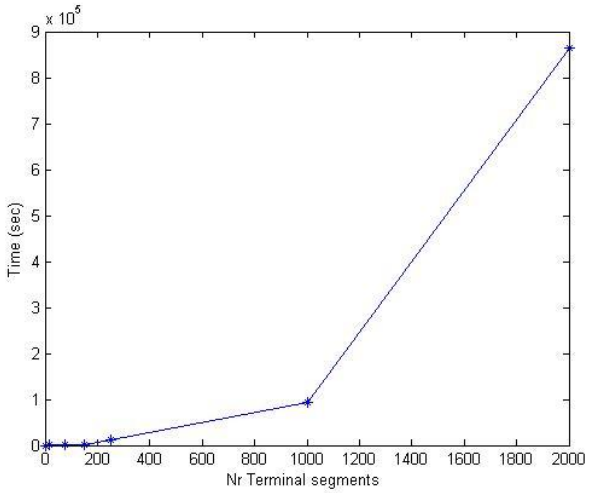

Figure 64: Run time of SM tree with different number of terminal segments.

The extended processing time for the larger trees is due to the repeated recalculation of the tree volume. In order to find the optimized geometrical position of a newly formed bifurcation the connection point is moved along its descending gradient of the total volume, i.e. the target function. This involves recalculating the volume of every segment in the tree in order to evaluate the total tree volume. This becomes increasingly more time consuming as the tree grows. Hopefully the efficiency of the SM tree program can be modified to increase its run speed.

12.8.1 SM Tree Data

The statistics on the SM tree are based on the data from two trees, T250 and T2000. The reason for growing the SM T250 tree is because it could be evaluated by comparing it to previous experimental results and the CCO tree of the same size. The statistics on the SM T2000 tree were based on a single tree, the reason for that is the time required to produce large binary trees, or trees of more than 1000 terminals proved to be very time consuming, Figure 64. Therefore it was not possible to grow a number of binary trees within the given timeframe of this thesis.

13 Conclusion

In this thesis a close resemblance between the SM tree and a true arterial tree has been demonstrated, both visually and geometrically. The morphometric distribution of radii and length showed a good correlation between the SM tree and previous experimental research. The real values of radii and length found in the T2000 SM tree were found to be of larger radii and shorter length compared to previously reported values in the literature. However the results from the T250 SM tree showed excellent correlation with previous experimental results. The physiological parameters of pressure changes in the SM T2000 tree strongly mimic known in vivo physiological parameters from the human circulation. The flow rate in the tree was larger than expected, but can easily be rectified by changing the initial parameters of the SM program.

The perfusion distribution diagram demonstrates a well known in vivo occurrence known as watershed zones which has recently been shown to be strongly associated with pathophysiological changes found on autopsies of brains from Alzheimer's patients.

14 Further Research

The results from this initial development of an SM tree are encouraging. The next step should focus on improving the efficiency of the SM program in order to increase the number of terminal segments which will give more accurate results. A possible solution to this problem is to store the volume of each segment of the tree as a ratio of its parent segment. Each segment should also store the subtree volume as a ratio of the subtree volume of its parent. The real

volume would therefore only be stored in the root node, see Appendix C for derivation of equations.

Another exciting development of the SM tree would be to produce a three-dimensional binary tree with the potential to further explore the concept of watershed areas, adjusted to various organs and their known pathophysiology. A three-dimensional tree would allow for oxygen and nutritional diffusion gradients to be calculated in specific areas. Those results would possibly give valuable information on tissue oxygenation and nutrition, identifying areas of marginal or frank deprivation.

Other future prospects would be to further explore the interaction between the boundary conditions and the geometrical shapes by changing one while observing the effect it has on the other.

References

1. Kumar, V., et al., *Robbins and Cotran pathologic basis of disease*. 7th ed. 2005, Philadelphia: Elsevier Saunders. xv, 1525 p.
2. *2009 Alzheimer's disease facts and figures.* Alzheimers Dement, 2009. **5**(3): p. 234-70.
3. Seeley, R.R., T.D. Stephens, and P. Tate, *Anatomy & physiology*. 6th ed. 2003, Boston: McGraw-Hill. 1 v. (in various pagings).
4. Moore, S., *Computational 3D modelling of hemodynamics in the circle of Willis*, in *Bio-Medical Engineering*. 2007, University of Canterbury: Christchurch.
5. Alberts, B., ed. *Molecular biology of the cell*. 1994, Garland Pub: New York.
6. Guyton, A.C. and J.E. Hall, *Textbook of medical physiology*. 11th ed. 2006, Philadelphia: Elsevier Saunders. xxxv, 1116 p.
7. Vinay Kumar, A.K., Nelson Fausto. , *Pathologic Basis of Disease*. 1999, Elsevier Saunders.
8. Alberts, B., *Molecular biology of the cell*. 3rd ed. 1994, New York: Garland Pub. xliii, 1294, [67] p.
9. Goldsmith, H., *Treatment of Alzheimer's disease by transposition of the Omentum.* New York Academy of Sciences, 2002: p. 454-467.
10. Beckmann, N., et al., *Age-dependent cerebrovascular abnormalities and blood flow disturbances in APP23 mice modeling Alzheimer's disease.* J Neurosci, 2003. **23**(24): p. 8453-9.
11. Zhao, J., et al., *Beta-site amyloid precursor protein cleaving enzyme 1 levels become elevated in neurons around amyloid plaques: implications for Alzheimer's disease pathogenesis.* J Neurosci, 2007. **27**(14): p. 3639-49.
12. Miyakawa, T., et al., *The relationship between senile plaques and cerebral blood vessels in Alzheimer's disease and senile dementia. Morphological mechanism of senile plaque production.* Virchows Arch B Cell Pathol Incl Mol Pathol, 1982. **40**(2): p. 121-9.
13. Sarah L.Cole, R.V., *Linking vascular disorder and Alzheimer's disease: Potential involvemt of BACE1*. Neurobiology of Aging, 2008.
14. Girouard, H. and C. Iadecola, *Neurovascular coupling in the normal brain and in hypertension, stroke, and Alzheimer disease.* J Appl Physiol, 2006. **100**(1): p. 328-35.

15. Niwa, K., et al., *Abeta 1-40-related reduction in functional hyperemia in mouse neocortex during somatosensory activation.* Proc Natl Acad Sci U S A, 2000. **97**(17): p. 9735-40.
16. Velliquette, R.A., T. O'Connor, and R. Vassar, *Energy inhibition elevates beta-secretase levels and activity and is potentially amyloidogenic in APP transgenic mice: possible early events in Alzheimer's disease pathogenesis.* J Neurosci, 2005. **25**(47): p. 10874-83.
17. Vassar, R., et al., *Beta-secretase cleavage of Alzheimer's amyloid precursor protein by the transmembrane aspartic protease BACE.* Science, 1999. **286**(5440): p. 735-41.
18. Small, G.W., et al., *Cerebral metabolic and cognitive decline in persons at genetic risk for Alzheimer's disease.* Proc Natl Acad Sci U S A, 2000. **97**(11): p. 6037-42.
19. Sun, X., et al., *Hypoxia facilitates Alzheimer's disease pathogenesis by up-regulating BACE1 gene expression.* Proc Natl Acad Sci U S A, 2006. **103**(49): p. 18727-32.
20. Peers, C. and P. Kemp, *Ion channel regulation by chronic hypoxia in models of acute oxyfen sensing.* Cell calcium, 2004. **36**: p. 341-348.
21. Torvik, A., *The pathogenesis of watershed infarcts in the brain.* Stroke, 1984. **15**(2): p. 221-3.
22. Minkner, K., et al., *White matter lesions in watershed territories studied with MRI and parenchymography: a comparative study.* Neuroradiology, 2005. **47**(6): p. 425-30.
23. Suter, O.C., et al., *Cerebral hypoperfusion generates cortical watershed microinfarcts in Alzheimer disease.* Stroke, 2002. **33**(8): p. 1986-92.
24. Cole, S. and R. Vassar, *Linking vascular disorder and Alzheimers disease: Potential involvement of BACE1*. Neurobiology of aging, 2009: p. 1-10.
25. Schreiner, W. and P.F. Buxbaum, *Computer-optimization of vascular trees.* IEEE Trans Biomed Eng, 1993. **40**(5): p. 482-91.
26. Carrano, F.M. and J.J. Prichard, *Data abstraction and problem solving with Java : walls and mirrors*. Updated ed. 2004, Boston [Mass.]: Pearson/Addison Wesley. xxii, 808 p.
27. Avolio, A.P., *Multi-branched model of the human arterial system.* Med Biol Eng Comput, 1980. **18**(6): p. 709-18.
28. Schreiner, W., *Computer generation of complex arterial tree models.* J Biomed Eng, 1993. **15**(2): p. 148-50.

29. Lauwers, F., et al., *Morphometry of the human cerebral cortex microcirculation: general characteristics and space-related profiles.* Neuroimage, 2008. **39**(3): p. 936-48.
30. Zamir, M. and S. Phipps, *Network analysis of an arterial tree.* J Biomech, 1988. **21**(1): p. 25-34.
31. Karch, R., et al., *Staged growth of optimized arterial model trees.* Ann Biomed Eng, 2000. **28**(5): p. 495-511.
32. Zamir, M., *Optimality principles in arterial branching.* J Theor Biol, 1976. **62**(1): p. 227-51.
33. Murray, C.D., *The Physiological Principle of Minimum work applied to the angle of branching of arteries.* The Journal of General Physiology, 1926: p. 835-841.
34. Kamiya, A. and T. Togawa, *Optimal branching structure of the vascular tree.* Bull Math Biophys, 1972. **34**(4): p. 431-8.
35. Suwa, N., et al., *Estimation of intravascular blood pressure gradient by mathematical analysis of arterial casts.* Tohoku J Exp Med, 1963. **79**: p. 168-98.
36. Mayrovitz, H.N. and J. Roy, *Microvascular blood flow: evidence indicating a cubic dependence on arteriolar diameter.* Am J Physiol, 1983. **245**(6): p. H1031-8.
37. Zamir, M., P. Sinclair, and T. Wonnacott, *Relation between diameter and flow in major branches of the arch of the aorta.* J Biomechanics, 1992. **25**: p. 1303-1310.
38. Zamir, M., *On fractal properties of arterial trees.* J Theor Biol, 1999. **197**(4): p. 517-26.
39. Olufsen, M.S., *Structured tree outflow condition for blood flow in larger systemic arteries.* Am J Physiol, 1999. **276**(1 Pt 2): p. H257-68.
40. Steele, B.N., M.S. Olufsen, and C.A. Taylor, *Fractal network model for simulating abdominal and lower extremity blood flow during resting and exercise conditions.* Comput Methods Biomech Biomed Engin, 2007. **10**(1): p. 39-51.
41. Dokoumetzidis, A. and P. Macheras, *A model for transport and dispersion in the circulatory system based on the vascular fractal tree.* Ann Biomed Eng, 2003. **31**(3): p. 284-93.
42. Karch, R., et al., *Functional characteristics of optimized arterial tree models perfusing volumes of different thickness and shape.* J Vasc Res, 2000. **37**(4): p. 250-64.
43. Karch, R., et al., *Fractal properties of perfusion heterogeneity in optimized arterial trees: a model study.* J Gen Physiol, 2003. **122**(3): p. 307-21.

44. Alzaidi, S., *1D Computational Models of Cerebral Hemodynamics*, in *BioMedical Engineering*. 2009, University of Canterbury: Christchurch.
45. Matsumoto, T.N.a.M. *Mersenne Twister Home Page. A very fast random number generator of period 219937-1* 1997 January 2002 [cited 2009 30 April]; Available from: http://www.math.sci.hiroshima-u.ac.jp/~m-mat/MT/emt.html.
46. Grimm, J., et al., *Grimm's fairy tales*. 2009, New York: Sterling Pub. Co.
47. Olufsen, M.S., et al., *Numerical simulation and experimental validation of blood flow in arteries with structured-tree outflow conditions.* Ann Biomed Eng, 2000. **28**(11): p. 1281-99.
48. Pries, A.R. and T.W. Secomb, *Microvascular blood viscosity in vivo and the endothelial surface layer.* Am J Physiol Heart Circ Physiol, 2005. **289**(6): p. H2657-64.
49. Gringorten, I.I. and P.J. Yepez, *The Division of a Circle or Spherical Surface Into Equal-Area Cells or Pixels.* Journal of Climate and Applied Metworology, 1992. **23**: p. 1253-1257.
50. VanBavel, E. and J.A. Spaan, *Branching patterns in the porcine coronary arterial tree. Estimation of flow heterogeneity.* Circ Res, 1992. **71**(5): p. 1200-12.
51. Frame , M.D.S. and I.H. Sarelius, *Energy Optimiztion and Bifurcation angles in the microcirculation.* Microvascular Research, 1995. **50**: p. 301-310.

15 Appendix A

15.1 An Example of ASCII file AllNodes.

0 3.13916e-007 1 0 0 | 286 3.18226e-005 0.999602 0.00218185 0.000399317 #
286 3.18226e-005 0.999602 0.00218185 0.000399317 | 20214 0.103363 0.964926 0.326617 0.108994 #
20214 0.103363 0.964926 0.326617 0.108994 | 20215 0.109887 0.941402 0.14406 0.024412 #
20214 0.103363 0.964926 0.326617 0.108994 | 30592 0.121088 0.95973 0.999012 0.0184709 #
30592 0.121088 0.95973 0.999012 0.0184709 | 50914 0.129806 0.956562 0.999034 0.0092756 #
50914 0.129806 0.956562 0.999034 0.0092756 | 50915 0.122712 0.925282 0.155485 0.0320741 #
50914 0.129806 0.956562 0.999034 0.0092756 | 14430 0.139295 0.953633 0.99875 0.00993046 #
14430 0.139295 0.953633 0.99875 0.00993046 | 14431 0.166319 0.982499 0.174039 0.0395421 #

16 Appendix B

16.1 An Example of ASCII file AllNodesLevels.

0 3.13916e-007 1 0 0 0 2000 0 5.31195e-005 | 286 3.18226e-005 0.999602 0.00218185 0.000399317 0.0133851 2000 5.97199e-009 5.31135e-005 1 B #
286 3.18226e-005 0.999602 0.00218185 0.000399317 0.0133851 2000 5.97199e-009 5.31135e-005 | 20214 0.103363 0.964926 0.326617 0.108994 0.00370897 82 1.73894e-007 1.53292e-006 2 B #
20214 0.103363 0.964926 0.326617 0.108994 0.00370897 82 1.73894e-007 1.53292e-006 | 20215 0.109887 0.941402 0.14406 0.024412 0.000111896 1 8.08296e-010 0 3 L #
20214 0.103363 0.964926 0.326617 0.108994 0.00370897 82 1.73894e-007 1.53292e-006 | 30592 0.121088 0.95973 0.999012 0.0184709 0.00323669 81 2.94109e-008 1.5027e-006 3 B #
30592 0.121088 0.95973 0.999012 0.0184709 0.00323669 81 2.94109e-008 1.5027e-006 | 50914 0.129806 0.956562 0.999034 0.0092756 0.00320212 80 1.47409e-008 1.48702e-006 4 B #
50914 0.129806 0.956562 0.999034 0.0092756 0.00320212 80 1.47409e-008 1.48702e-006 | 50915 0.122712 0.925282 0.155485 0.0320741 0.000147017 1 1.23229e-009 0 5 L #
50914 0.129806 0.956562 0.999034 0.0092756 0.00320212 80 1.47409e-008 1.48702e-006 | 14430 0.139295 0.953633 0.99875 0.00993046 0.00318383 79 1.57422e-008 1.47005e-006 5 B #
14430 0.139295 0.953633 0.99875 0.00993046 0.00318383 79 1.57422e-008 1.47005e-006 | 14431 0.166319 0.982499 0.174039 0.0395421 0.000181247 1 1.89866e-009 0 6 L #
14430 0.139295 0.953633 0.99875 0.00993046 0.00318383 79 1.57422e-008 1.47005e-006 | 41956 0.172823 0.941457 0.998519 0.0356703 0.00317013 78 5.63787e-008 1.41177e-006 6 B #

17 Appendix C

If V_1 is the volume of a segment before change in radius and V_2 is the volume of the same segment after a change in radius

$$V_1 = r_i^2 \pi l_i$$
$$V_2 = a r_i^2 \pi l_i$$
$$a = 1.0 + \delta r_i / r_i$$

By substituting V_1 in the following way

$$V_2 = a(V_1)$$

It can be seen that the change in radius a can be used as a scaling factor for the volume.

This is also true for the total volume of the tree

$$Volume_{total} = \sum_{i=1}^{N_{total}} a(r_1^2 \pi l_1 + r_2^2 \pi l_2 + \cdots r_i^2 \pi l_i)$$

The change of root radius in the optimization progress is used to recalculate the total volume of the subtree in the root node. The whole tree would therefore be scaled due to the ratio connections of the subtree nodes. This would save the repeated recalculation of the whole tree volume and increase the efficiency of the program.

18 Appendix D

Compact Disc containing;

1. Complete thesis document
2. Binary tree code
3. MatLab code
4. Data on SM tree structure:
    - 4.1. T15
    - 4.2. T75
    - 4.3. T250
    - 4.4. T500
    - 4.5. T1000
    - 4.6. T2000